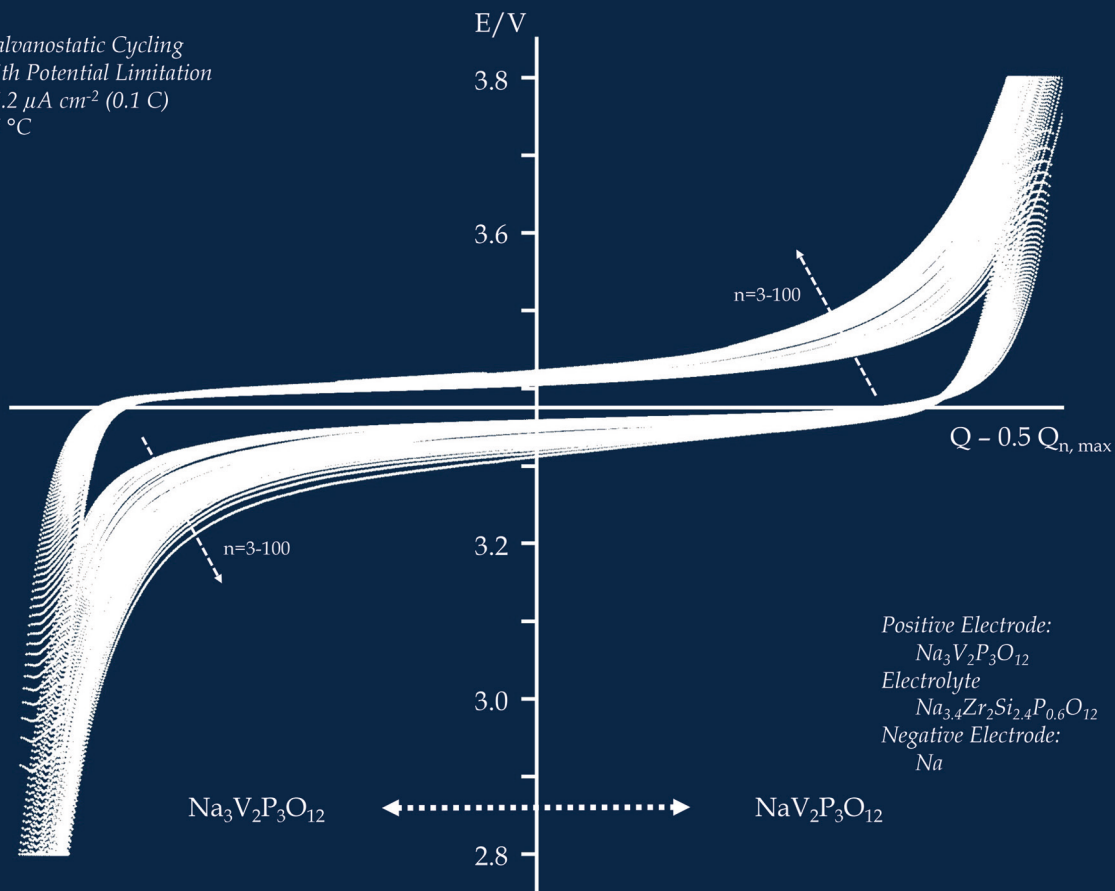


Galvanostatic Cycling
with Potential Limitation
 $35.2 \mu\text{A cm}^{-2}$ (0.1 C)
25 °C



Infiltrated Positive Electrodes for All-Solid-State Sodium Batteries

Tu Lan

Energie & Umwelt / Energy & Environment

Band / Volume 551

ISBN 978-3-95806-576-5

Forschungszentrum Jülich GmbH
Institut für Energie- und Klimaforschung
Werkstoffsynthese und Herstellungsverfahren (IEK-1)

Infiltrated Positive Electrodes for All-Solid-State Sodium Batteries

Tu Lan

Schriften des Forschungszentrums Jülich
Reihe Energie & Umwelt / Energy & Environment

Band / Volume 551

ISSN 1866-1793

ISBN 978-3-95806-576-5

Bibliografische Information der Deutschen Nationalbibliothek.
Die Deutsche Nationalbibliothek verzeichnet diese Publikation in der
Deutschen Nationalbibliografie; detaillierte Bibliografische Daten
sind im Internet über <http://dnb.d-nb.de> abrufbar.

Herausgeber und Vertrieb: Forschungszentrum Jülich GmbH
Zentralbibliothek, Verlag
52425 Jülich
Tel.: +49 2461 61-5368
Fax: +49 2461 61-6103
zb-publikation@fz-juelich.de
www.fz-juelich.de/zb

Umschlaggestaltung: Grafische Medien, Forschungszentrum Jülich GmbH

Druck: Grafische Medien, Forschungszentrum Jülich GmbH

Copyright: Forschungszentrum Jülich 2021

Schriften des Forschungszentrums Jülich
Reihe Energie & Umwelt / Energy & Environment, Band / Volume 551

D 82 (Diss. RWTH Aachen University, 2020)

ISSN 1866-1793
ISBN 978-3-95806-576-5

Vollständig frei verfügbar über das Publikationsportal des Forschungszentrums Jülich (JuSER)
unter www.fz-juelich.de/zb/openaccess.



This is an Open Access publication distributed under the terms of the [Creative Commons Attribution License 4.0](https://creativecommons.org/licenses/by/4.0/), which permits unrestricted use, distribution, and reproduction in any medium, provided the original work is properly cited.

The infant flower opens its bud and cries,

"Dear World, please do not fade."

— — *Stray Birds*: 66

Abstract

All-solid-state batteries (ASSBs) are regarded as promising candidates for next-generation energy storage systems due to several superior properties in comparison to state-of-the-art batteries using liquid electrolytes. ASSBs have advantages with respect to no-leaking electrolytes, wider temperature window, and potentially higher volumetric energy density than those batteries using liquid electrolyte. In addition, ceramic ion-conducting oxides, as electrolyte materials, offer further benefit from their high conductivity, as well as good mechanical, chemical, and thermodynamic stability.

Though great achievements have been made in the development of all-solid-state batteries, there are still a number of problems to be solved, especially with respect to the positive electrodes. The rigid nature of solid-state electrolyte materials restricts the electrolyte-electrode contact and causes problems during the fabrication of components. In the positive electrodes, contacts between randomly-arranged grains of Na-ion conductors and electrode active materials are not efficient for both ion conduction and electrochemical reaction. These rigid contacts are further damaged by volume changes of electrode active materials during electrochemical cycling.

These electrode problems above are reported to be more severe in Na-based ASSBs (Na-ASSBs) due to the larger ionic radius of Na^+ and thus larger volume changes of the electrode materials. In order to solve the problems associated with the positive electrodes of Na-ASSBs, a new electrode design is needed together with a practical preparation method.

In this thesis, Na-ASSBs have been built using NaSICON-type $\text{Na}_{3.4}\text{Zr}_2\text{Si}_{2.4}\text{P}_{0.6}\text{O}_{12}$ as the electrolyte material. A material with similar structure as the electrolyte, $\text{Na}_3\text{V}_2\text{P}_3\text{O}_{12}$, was chosen as the positive electrode material. $\text{Na}_3\text{V}_2\text{P}_3\text{O}_{12}$ has been widely studied as the electrode material for batteries with liquid electrolyte, but only a few unsuccessful attempts have been made to apply the material in ASSBs.

As a starting point, the basic properties of $\text{Na}_3\text{V}_2\text{P}_3\text{O}_{12}$ were studied, from the synthesis to the characterization of the pure material. Then model ASSBs were built based on a back-bone design of the positive electrode. A new method, named chemical infiltration, has been developed combining the ideas of infiltration with *in situ* synthesis of the electrode material. *In situ* synthesis of the electrode material was performed to improve the interface between electrode and electrolyte materials, and was realized by infiltrating a precursor solution and forming the active electrode phase by a chemical reaction on the pore walls of the electrolyte. In ASSBs made by chemical infiltration, the electrode material showed excellent adhesion to the electrolyte, resulting in a low internal resistance of the cell. Additionally, this electrode structure ensures a high tolerance to the volume change of the electrode material. As a result, the Na-ASSBs have highly stable performance with low internal resistance and low fading rate.

Na-ASSBs in this thesis became the first successful examples showing that contact problems in positive electrode can be solved without using any soft phase (liquid, polymers, ionic liquids etc.) as a compensator of volume changes or wetting medium. This method also enables the fabrication of very thick electrode layers for high capacities. Based on the experimental studies in this work, the future developments of ASSBs, including the possibilities and limitations, can be better assessed.

Kurzfassung

Festkörperbatterien (ASSBs) gelten als vielversprechende Kandidaten für Energiespeichersysteme der nächsten Generation aufgrund mehrerer überlegener Eigenschaften im Vergleich zu modernen Batterien mit flüssigen Elektrolyten. ASSBs haben Vorteile in Bezug auf auslaufsichere Elektrolyte, breitere Temperaturbereiche und potenziell höhere volumetrische Energiedichten als Batterien mit flüssigem Elektrolyt. Darüber hinaus bieten keramische ionenleitende Oxide als Elektrolytmaterial einen weiteren Vorteil durch ihre hohe Leitfähigkeit sowie eine gute mechanische, chemische und thermodynamische Stabilität.

Obwohl bei der Entwicklung von Festkörperbatterien große Erfolge erzielt wurden, gibt es noch eine Reihe von Problemen zu lösen, insbesondere im Hinblick auf die positiven Elektroden. Die starre Natur der Festkörperelektrolytmaterialien schränkt den Kontakt zwischen Elektrolyt und Elektrode ein und verursacht Probleme bei der Herstellung von Komponenten. Bei den positiven Elektroden sind die Kontakte zwischen zufällig angeordneten Körnern von Na-Ionenleitern und elektrodenaktiven Materialien sowohl für die Ionenleitung als auch für die elektrochemische Reaktion nicht effizient. Diese starren Kontakte werden durch Volumenänderungen der elektrodenaktiven Materialien während der elektrochemischen Zyklen weiter beschädigt.

Diese oben genannten Elektrodenprobleme sind Berichten zufolge bei Na-basierten ASSBs (Na-ASSBs) aufgrund des größeren Ionenradius von Na^+ und damit größerer Volumenänderungen der Elektrodenmaterialien stärker ausgeprägt. Um die Probleme im Zusammenhang mit den positiven Elektroden von Na-ASSBs zu lösen, ist ein neues Elektrodendesign zusammen mit einer praktischen Herstellungsmethode erforderlich.

In dieser Arbeit wurden Na-ASSBs mit $\text{Na}_{3,4}\text{Zr}_2\text{Si}_{2,4}\text{P}_{0,6}\text{O}_{12}$ als Elektrolytmaterial hergestellt. Ein Material mit ähnlicher Kristallstruktur wie der Elektrolyt, $\text{Na}_3\text{V}_2\text{P}_3\text{O}_{12}$, wurde als positives Elektrodenmaterial gewählt. $\text{Na}_3\text{V}_2\text{P}_3\text{O}_{12}$ wurde als Elektrodenmaterial für Batterien mit flüssigem Elektrolyt umfassend untersucht,

aber es wurden nur wenige erfolglose Versuche unternommen, das Material in ASSBs einzusetzen.

Als Ausgangspunkt wurden die grundlegenden Eigenschaften von $\text{Na}_3\text{V}_2\text{P}_3\text{O}_{12}$ untersucht, von der Synthese bis zur Charakterisierung des reinen Materials. Dann wurden Modell-ASSBs auf der Grundlage eines Grundgerüst-Designs der positiven Elektrode hergestellt. Eine neue Methode, die chemische Infiltration genannt wird, wurde entwickelt, die die Ideen der Infiltration mit der *in situ*-Synthese des Elektrodenmaterials kombiniert. Die *in-situ*-Synthese des Elektrodenmaterials wurde durchgeführt, um die Grenzfläche zwischen Elektroden- und Elektrolytmaterial zu verbessern, und wurde durch Infiltration einer Lösung mit den Edukten und Bildung der aktiven Elektrodenphase durch eine chemische Reaktion an den Porenwänden des Elektrolyten realisiert. Bei ASSBs, die durch chemische Infiltration hergestellt wurden, zeigte das Elektrodenmaterial eine ausgezeichnete Haftung am Elektrolyten, was zu einem niedrigen Innenwiderstand der Zelle führte. Zusätzlich gewährleistet diese Elektrodenstruktur eine hohe Toleranz gegenüber der Volumenänderung des Elektrodenmaterials. Als Ergebnis haben die Na-ASSBs eine sehr stabile Leistung mit niedrigem Innenwiderstand und geringem Kapazitätsverlust.

Die Na-ASSBs in dieser Arbeit sind die ersten erfolgreichen Beispiele, die zeigen, dass Kontaktprobleme in positiven Elektroden gelöst werden können, ohne dass eine weiche Phase (Flüssigkeit, Polymere, ionische Flüssigkeiten usw.) als Kompensator von Volumenänderungen oder Benetzungsmedium verwendet wird. Diese Methode ermöglicht auch die Herstellung von sehr dicken Elektrodenschichten für hohe Kapazitäten. Auf der Grundlage der experimentellen Untersuchungen in dieser Arbeit können die zukünftigen Entwicklungen von ASSBs, einschließlich der Möglichkeiten und Grenzen, besser beurteilt werden.

Table of Contents

List of Abbreviations	vi
I Introduction	1
1.1 Solid-State Batteries	2
1.2 Na-based Batteries	14
1.3 $\text{Na}_3\text{V}_2(\text{PO}_4)_3$	18
1.4 Scope of this Thesis	25
II Methodology.....	26
2.1 Synthesis Methods	26
2.2 Fabrication of Na-ASSBs	29
2.3 Characterization methods.....	32
III Synthesis and Characterization of NVP	42
3.1 Preparation of NVP samples	42
3.2 Conductivity of NVP measured on Na-ASSBs with thin layer NVP	57
IV Na-ASSBs Prepared by Chemical Infiltration.....	61
4.1 Design	61
4.2 Fabrication.....	65
4.3 Performance	71
4.4 Characterization	79
4.5 Discussion: Infiltrated Na-ASSBs compared with other ASSBs.....	86
4.6 Outlook.....	89
V Summary	94
References.....	96
Acknowledgements	101

List of Abbreviations

ASSB	all-solid-state battery
CV	cyclic voltammetry
DTA	differential thermal analysis
GC	gas chromatography
GCPL	galvanostatic cycling with potential limitation
LIB	Li-ion battery
MS	mass spectrometer
NaSICON	Na super ion conductor
NMR	nuclear magnetic resonance
NVP	$\text{Na}_3\text{V}_2\text{P}_3\text{O}_{12}$
NZSP	$\text{Na}_{3.4}\text{Zr}_2\text{Si}_{2.4}\text{P}_{0.6}\text{O}_{12}$
PAN	poly(acrylonitrile)
PEIS	potentiostatic electrochemical impedance spectroscopy
PEO	poly(ethylene oxide)
PVdF	poly(vinylidene fluoride)
RS	rice starch
RT	room temperature
SEM	scanning electron microscopy
STEM	scanning transmission electron microscopy
TG	thermogravimetry
XPS	X-ray photoelectron spectroscopy
XRD	X-ray diffraction

I Introduction

The present thesis, *Infiltrated Positive Electrodes for All-Solid-State Sodium Batteries*, discusses the design and the preparation of positive electrodes for all-solid-state batteries (SSBs). The thesis also aims to solve the particular problems related to positive electrodes of oxide-based Na-ASSBs, as shown schematically in Figure 1.1. These problems act as a main obstacle to the application of Na-ASSBs, and have remained unsolved till the results presented in this thesis.

In the first chapter, I will introduce briefly the related concepts, state-of-the-art in ASSB research, and especially unsolved challenges in this field. Also, previous studies on $\text{Na}_3\text{V}_2(\text{PO}_4)_3$, the main electrode active material used in the thesis, will be introduced in this chapter.

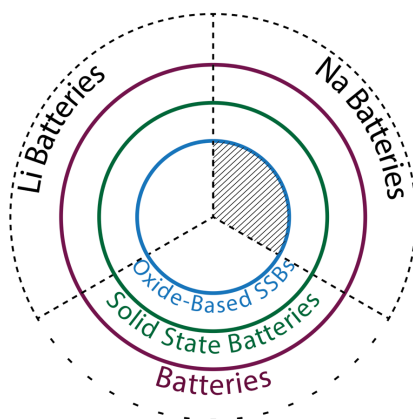


Figure 1.1 Relation of oxide-based Na-ASSBs (with stripe pattern) and related concepts

1.1 Solid-State Batteries

1.1.1 Rechargeable Batteries: Components and Key Properties

Rechargeable batteries are electrochemical devices that convert the chemical energy directly into electric energy during discharge, and backwards during charge. As energy storage devices, rechargeable batteries play a crucial role in modern society, powering electrical devices from cell phones to electric vehicles [1-3].

Components in a rechargeable battery

The basic unit of a battery is named a “cell”, which consists of the positive and negative electrodes, as well as the electrolyte between them, as shown schematically in **Figure 1.2**.

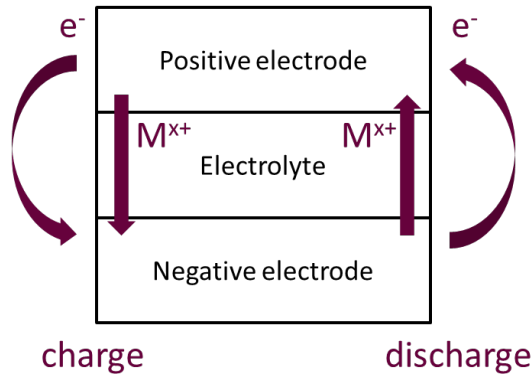


Figure 1.2 Components of a battery cell and the movement of ions (M^{x+}) and electrons (e^-) during charge and discharge of the battery

During the charge of the battery, the positive electrode is oxidized, releasing both ions and electrons, while the negative electrode receives both and gets reduced. The electrons migrate in an outer circuit, driven by an external power source, and the ions move inside the electrolyte. During the discharge of a battery, the process goes in a reversal direction and providing power to the outer circuit via the migration of electrons. In publications of the battery community, positive/negative electrode is

commonly called cathode/anode. However, it is not a scientifically accurate way of naming. By definition: positive/negative electrode is the one with higher/lower potential; cathode is the electrode where the current leaves and anode, where the current goes to. During the discharge of a rechargeable battery, the positive/negative electrode of a cell do act as the cathode/anode; during the charge of the battery, the roles (cathode & anode) of the two electrodes switch, while the relative potential remains the same. This thesis will use positive and negative to determine the two electrodes of a cell.

Key properties of a battery cell

There are several important properties of a battery cell, which help to evaluate the performance of a cell. The **energy** stored in a cell is the product of **capacity** multiplied by **operation voltage**, both are essential properties of a cell.

Capacity is the cumulated charge of the ions stored in electrodes, and the capacity of a cell is determined by the electrode with the lower one. During cell cycling, part of the electrode (usually the positive) will lose function and the capacity will fade. The decrease of capacity is named **degradation**, and is commonly used to quantify the stability of a cell. **Specific weight capacity**, i.e. capacity divided by the mass of active electrode material, is a property of the electrode material, and materials with higher specific capacities are desired. Another normalization, capacity divided by the area of the cell (perpendicular to the current direction), i.e. **specific area capacity**, is the property correlated to the cell structure.

Coulombic efficiency is the percentage of discharge capacity against the charge one during one charge-discharge cycle, and should be close to 100% ideally. A low efficiency indicates some defects in the cell. The defects can be the irreversible change of electrode active materials during operation, and will accumulate into the degradation of the cell during cycling; another possible reason is the leakage of electronic current through the electrolyte.

Operation voltage is determined by the potential difference of electrochemical reactions in the two electrodes. Thus, positive electrode materials with high potential and negative electrode materials with low potential are desired. During the cycling

of a cell, the voltage during the charge is usually higher than that during discharge. The difference is named **polarization** and will cause a loss of energy. Polarization originates from several different sources: charge-transfer overvoltage to activate electrochemical reactions (activation polarization), inhomogeneous distribution of ions (concentration polarization), and most importantly ohmic polarization caused by **internal resistance** of the cell. In order to minimize the internal resistance, efficiency of ion and electron transfer through the whole cell should be maximized by using electrolyte materials with high conductivities, adding proper electronic conducting phase in the electrodes, and guaranteeing good contact between different parts.

Loading of a cell is the amount of active electrode material used. In order to evaluate cell designs, loading per area is commonly used, which have a direct influence on the specific area capacity, together with the specific weight capacity of the electrode material used.

The charge/discharge speed of a cell is evaluated by **C-rate**. "A cell charge/discharge at $n\ C$ ", means the cell is fully charged/discharged in $\frac{1}{n}$ hours. There are some variations of the definition of "fully charged/discharged". In this thesis, the theoretical capacity of all the active electrode materials is used to calculate C-rates, though a real cell will never reach the capacity.

Definitions that are more systematically accurate can be found in the references [2,4].

1.1.2 Solid-State Batteries: Introduction

Solid-state batteries (SSBs), as the name tells, are batteries that only contain components in the solid-state. Most state-of-the-art batteries use some kind of liquid phase as electrolyte (mostly, Li salts organic solvent), which are the usually preferred ion conductors [3]. However, recent research start to pay more attentions to ASSBs using solid ion conductors as electrolyte [1].

Complex liquid solution have been developed as electrolyte materials since the invention and application of batteries, which have good ionic conductivities and

ideal wetting of electrode materials [2]. The ion conduction of these liquid phases are enabled by diffusion of ions, which is quite easy in a solvent. The fluidity of liquid electrolytes guarantees the contact between electrodes and electrolyte, and thus the efficiency of the ion transfer. In the 1990s, Li-ion batteries with organic liquid electrolyte saw a boost in applications and brought the importance of rechargeable batteries to a new level. Commonly organic liquid electrolytes consist of Li salts (e.g. LiPF_6 , LiBF_6 , and LiClO_4) in carbonate solvents (e.g. ethylene carbonate, dimethyl carbonate, and diethyl carbonate) [5].

Solid phases as ion conductors date back to a very early time, when the conduction properties of Ag_2S and PbF_2 were discovered [6]. In the 1960s, the applicable solid-state conductors, including β -alumina [7], $\text{Na}_{1+x}\text{Zr}_2\text{Si}_x\text{P}_{3-x}\text{O}_{12}$ [8], Ag_3SI [9], and RbAg_4I_5 [10], as well as the organic poly(ethylene oxide) (PEO) based materials [11]. However, batteries using these solid electrolytes stay mainly in laboratories, with limited commercial applications such as high-temperature Na-S batteries [12,13] and ZEBRA batteries [14-16].

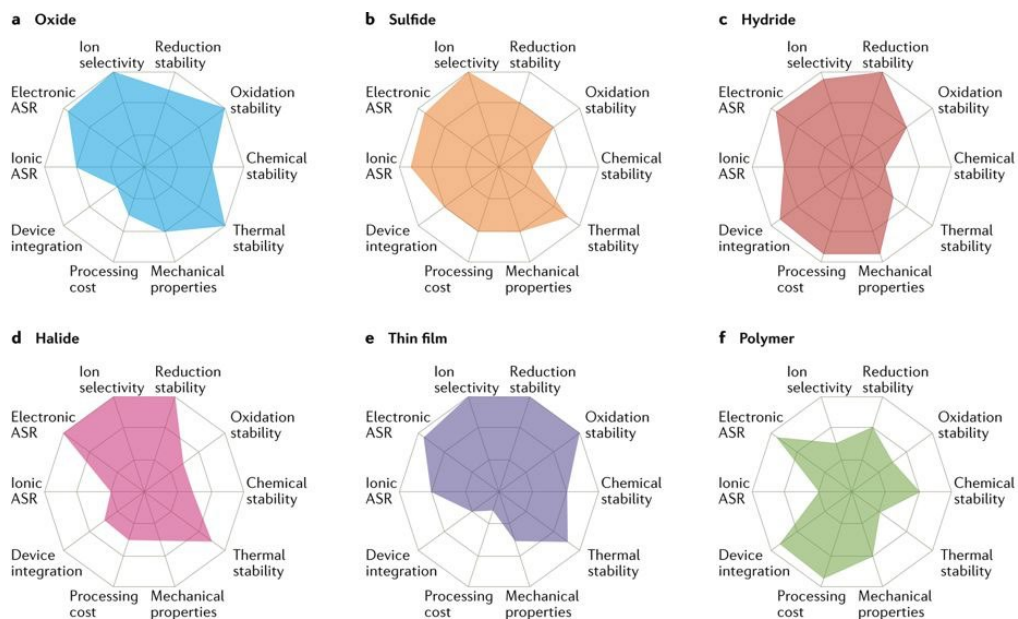
With increasing concerns about battery safety, today more attention has been paid on ASSBs. The liquid electrolytes are usually organic liquids, which are flammable, sensitive to temperature change, and have leakage problems [17]. The solid electrolytes generally can solve these problems above. The next part will introduce the properties of different kinds of solid-state electrolytes in details.

One last thing about the names of related concepts: in publications of the battery community, *all-solid-state* and *solid-state* cover the same range of batteries. Although there are papers involving liquid-containing batteries, they are also claimed as *all-solid-state* or *solid-state*. *Quasi-solid-state* [18] is used, though rarely, by some honest authors to describe liquid containing batteries.

1.1.3 Classification of ASSBs

SSBs are usually classified by the electrolyte used, which strongly influence the battery properties and the design strategy. Some solid-state electrolytes are inorganic, including oxides, sulphides, halides, and hydrides. In addition, there are different kinds of organic electrolyte, and their composites with inorganic phases.

Figure 1.3 summarizes the properties of different kinds of electrolytes [1]. Different types of electrolytes have their own pros and cons, and thus different applications as well as different problems during development.



Nature Reviews | Materials

Figure 1.3 Radar plots of the performance properties of oxide solid electrolytes (panel a), sulphide solid electrolytes (panel b), hydride solid electrolytes (panel c), halide solid electrolytes (panel d), thin-film electrolytes (panel e) and polymer solid electrolytes (panel f). ASR = area-specific resistance. [1] (Reprinted with permission, license number: 4646400446522)

Typical oxide conductors include NaSICON-type materials and garnet materials. NaSICON (Na Super Ion CONductor) materials include $\text{Na}_{1+x}\text{Zr}_2\text{Si}_x\text{P}_{3-x}\text{O}_{12}$ [8] for Na-ion conductors, as well as $\text{Li}_{1+x}\text{Al}_x\text{Ti}_{1-x}\text{P}_3\text{O}_{12}$ [19] for Li-ion conductors. Garnet materials are represented by $\text{Li}_7\text{La}_3\text{Zr}_2\text{O}_{12}$ [20]. Oxide electrolyte materials have the advantage of relatively high conductivity, as well as high chemical, electrochemical, and mechanical stability. However, the stiffness of the oxides also brings severe problems related to the electrolyte-electrode contacting and device integration. Also,

it is worth noting that the fabrication of oxides usually include high-temperature sintering, which is costly in the case of mass production [1,21].

Some inorganic ion conductors are soft materials, including sulphides (represented by Na_3PS_4 [22] and $\text{Li}_{10}\text{GeP}_2\text{S}_{12}$ [23]) and hydrides ($\text{Na}_2(\text{B}_{12}\text{H}_{12})_{0.5}(\text{B}_{10}\text{H}_{10})_{0.5}$) [24]. These conductors have higher conductivities. Different from oxides, these soft phases are more ductile, but suffer from lacking chemical stability. In addition, the conductors above are usually not stable with high potential and limit the operating voltage of the battery.

Polymer electrolytes are represented by the PEO[11]-, poly(acrylonitrile) (PAN)[25]-, and poly(vinylidene fluoride) (PVdF) [26]-based materials. Also, composite electrolytes have been made by mixing polymer with ceramic fillers (e.g. LiAlO_2 [27], Al_2O_3 [25], and SiO_2 [28]). Polymer electrolytes have good mechanical flexibility[1,29]. However, polymer electrolytes usually have lower stability, and also have limited conductivities [29].

In summary, oxides as ion conductors are the most “solid” among the solid-state electrolytes with high stability as well as the high conductivities. However, there are also plenty of challenges to be solved before practical application of ASSBs made from oxide conductors, especially in the positive electrodes.

1.1.4 Oxide-Based ASSBs and Current Challenges

As discussed in the last part, oxide-based ion-conductors have the potential as the ultimate replacement of liquid electrolytes, with the benefits of high conductivity and good stability [1,30]. However, the rigid nature of the oxide conductors also become an obstacle, considering the necessity of a well-established ion pathway through the whole cell and high-efficient electrolyte-electrode contacts.

Negative electrodes and the dendrite problem

Dendrite growth occurs in battery cells with metallic negative electrodes and is referring to the abnormal growth of negative electrode material into the electrolyte, which leads to the short-circuit of the cell. Solid electrolytes are supposed able to suppress the dendrite growth, and thus enable the use of metallic negative

electrodes. This ability is regarded as a main advantage of ASSBs, since metallic negative materials have both high specific capacities and low potentials, enabling high energy densities.

Metallic Na/Li is soft and can guarantee an effective contact. However, dendrites still occur in ASSBs depending on the cycling conditions [31,32]. Till now no reported materials combination can meet the requirements for a typical commercial cell, with respect to both capacity and C-rate [33,34]. A commonly accepted mechanism is yet to be revealed, dendrite forms either during the stripping of metal electrode, i.e. the charge of a battery cell (**Figure 1.4**), or during the plating of metal electrode, as assumed by some other reports. Nevertheless, an increasing number of researchers agree that it is the loss of contact, coming from the solid state of electrolyte material, that causes the high current density at some specific points and then the formation of dendrites [31,35]. Comparing the Na and Li systems, Na-ASSBs have a higher tolerance to the dendrite formation, from the higher self-diffusion coefficient of Na making it more difficult for point contacts to appear, as shown in **Figure 1.4** [36].

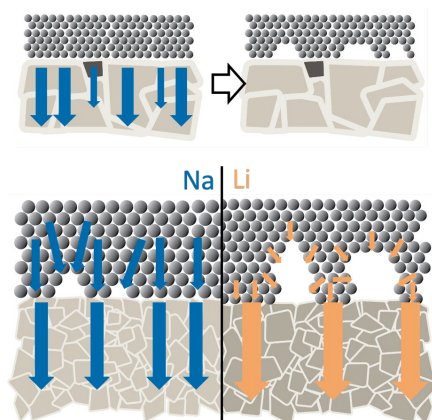


Figure 1.4 The stripping mechanism of dendrite formation and the difference between Na- and Li- ASSBs: dendrite can occur when point contact forms in lower conducting regions (impurities and grain boundaries), caused by current density exceeding the limitation of self-diffusion of metal in the electrode. [36]

Positive electrodes: the contact problem & the problem of mixing electrode composites

In the positive electrode, contact problems are more severe, since the positive electrode materials are also rigid, unlike the negative ones. The contact is further damaged during the cell cycling, when the volume of the electrode materials will change with the intercalation and deintercalation of ions. Inefficient contact will cause a high internal resistance of the cell, and energy will be wasted by ohmic polarization. In addition, the damaged interface during cycling will detach some of electrode active material particles from the electrolyte material particles, leading to the degradation of capacity of the battery. Several methods have been used to improve the inter-ceramic contact in the positive electrode. Most of them use a soft phase, solid or liquid, to improve the contact between two rigid phases. The most simple and direct "solution" is using liquid to wet the interface [37-43]. Ionic liquids, similar to those used as electrolyte, are added to the composite electrode. However, using liquid in the electrode part is contradictory to the use of oxide electrolyte, sacrificing safety and stability. Using polymer as a soft media brings similar problems, and dry polymers usually have limited conductivity and the batteries made have to operate at a higher temperature [44,45]. In cells using soft active electrode materials and electrolyte materials (e.g. sulphides and hydrides), contact can be improved by using mechanical pressure on the cell [21]. However, mechanical pressure is not very effective in oxide-based ASSBs, which still have severe degradation [46].

Moreover, since most active materials for positive electrodes have limited ionic and electronic conductivities, it is necessary to mix the active materials with electrolyte materials and possibly electronic conducting materials (e.g. carbon). The densification of this mixture, in order to connect the ion and electron pathway efficiently, is also a problem, considering the different sintering behaviours of different components. Till now the co-sintering of electrode composite has not been solved properly, leaving random porosity in the structure. Also, the connection between particles of active materials and electrolyte materials is ineffective via sintering [34].

The following part will introduce the different types of positive electrode design with typical examples, and whether these designs can solve the problems mentioned above.

Typical designs of positive electrodes in ASSBs

The conventional design of positive electrodes is based on mixing powders of electrode and electrolyte materials, and co-sintering the mixture. Many previous works used this design and many efforts have been made on the selection of materials with tolerance to co-firing, and also on the optimization of technical details of the process [34,47]. However, till now this method has hardly solved the contact problem or the ineffective compactness of the composite: still an optimized sintering process is not achieved. As shown in **Figure 1.5**, the random oriented particles in the electrode have limited contact between each other with various pore size between them.

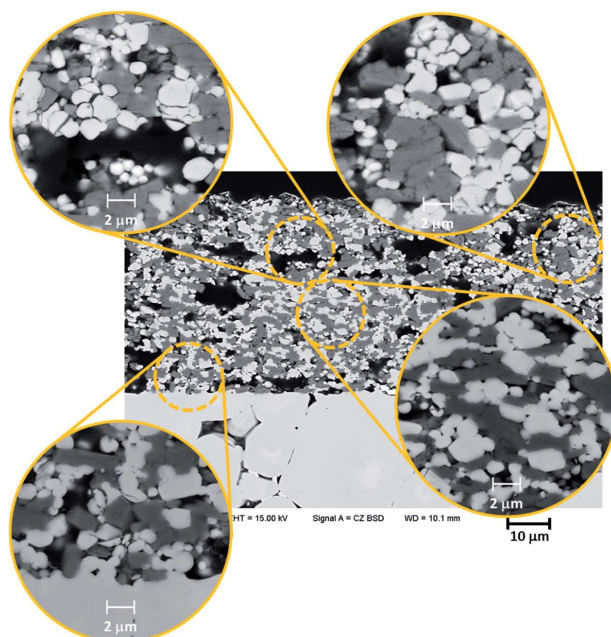


Figure 1.5 A typical positive electrode composite made by mixing and co-firing process [34] (Reprinted with permission, license number: 1004740-1)

By using techniques such as FAST/SPS (Field Assisted Sintering Technique/ Spark Plasma Sintering), the porosity of the composite can be reduced and a densified structure, and better contact between components can be achieved, as shown in **Figure 1.6**. In addition, FAST/SPS enables more options for material selection, since the sintering temperature and time are reduced due to mechanical pressure. However, such a structure showed limited tolerance to the volume change of the active material, leading to fast fading of capacity, even at a higher temperature of 200 °C [48].

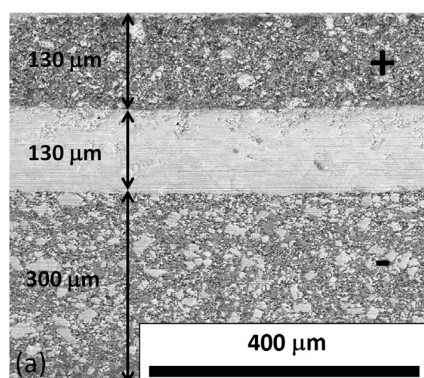


Figure 1.6 A typical microstructure of ASSBs made by FAST/SPS [48]
(Reprinted with permission, license number: 4713081479799)

Another method uses materials with low melting points to build an interlayer between electrode and electrolyte materials, which similarly solves the contact problem and the different sintering temperature between materials. As an example, $\text{Li}_{2.3-x}\text{C}_{0.7+x}\text{B}_{0.3-x}\text{O}_3$ is proposed by Han et al. [49] for Li-ASSBs, and similar methods (with $\text{Na}_2\text{FeP}_2\text{O}_7$ glass) are also applied on Na-ASSBs [50]. However, the tolerance of such interlayer to volume change of the electrode material is doubtful, since some cells reported show a fluctuating capacity during cycling. Also, the scalability of the structure is not satisfactory, for an increased loading would reduce the discharge capacities greatly [50], which is probably due to the limited conductivity of the interlayer material.

By depositing a thin layer of active electrode material on the surface of the electrolyte material, the problems of mixing seems to be solved [51,52]. By choosing proper depositing method, the contact can be guaranteed, as shown in **Figure 1.7**. However, without mixing with electrolyte material, the total thickness of the electrode layer is limited in order to avoid high resistance resulting from the poor conductivity of the active material. Thus, the scalability of this design, as well as the full cell energy density, is questionable.

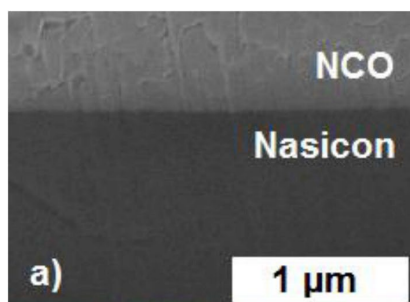


Figure 1.7 A typical microstructure of ASSBs made by thin film technologies [51]
(Reprinted with permission, license number: 4713090188135)

In summary, for positive electrodes of ceramic-based ASSBs, a composite of active electrode materials and electrolyte material is necessary, because of the limited ionic conductivities of the active electrode materials. Battery cells with thin film electrode materials are possible, but the thickness of electrode material layer limits the loading and thus the energy density. For bulk-type cells, no current methods can perfectly solve both the contact problem and the packing of the mixed electrode and electrolyte particles.

The composite in the positive electrode also raises another problem: the energy density. A lower amount of electrolyte material is desired for a higher energy density, since only the electrode materials store ions. However, a certain amount of electrolyte materials is needed for a well-established ionic pathway in the composite [53]. As calculated in the sulphide system, it is rather difficult to have a 50 wt. % ratio of active electrode material in the composite, while in liquid cells it is normally

90% [53]. The difference is due to the fact that the solid electrolyte establishes a network in form of particles with a specific size, but the liquid electrolyte can easily penetrate the remaining porosity. The energy density problem is very important to the possible application of ASSBs, and is discussed in details in **Section 4.6**.

Application of porous structure in ASSBs

In order to overcome the contact problems in ASSBs, a direct solution is to enlarge contact area, so that the overall ion transport at the interface improves. With maximum contact area vs. total mass, thin films are ideal electrode structure in theory. However, thin film electrodes and oxide electrolytes, unable to fold or roll up, lack scalability and may face great limitations to practical applications. In addition, thin film techniques usually involve expensive methods [51,52,54].

An alternative method is very similar to “folding”, by building a porous electrolyte and fill the electrode material into the porosity. Similar methods have been applied in the field of solid oxide cells, whose electrochemical performance also depends strongly on the contact between two ceramic materials [49,55-57].

Reports on applications of such porous structure in battery cells are limited. Several methods have been developed to build up the scaffold, mainly by mixing various types of organic chemicals into electrolyte powder, which will be removed during sintering of the electrolyte. Kotobuki used monodispersed polystyrene beads as pore former [58], and also tried to build structures with different scales [59]. Similarly, poly(methyl methacrylate) [60-62] and graphite [63] were also used as pore former. Alternatively, 3D-printing was used to build up the scaffold [64]. Till now the porous structure is mainly used in the negative electrodes, with metallic Li/Na infiltrated into the porous electrolyte material, in order to increase contact area and thus decrease real current density. Due to the limited wettability of molten Li/Na metal on electrolyte materials, it is usually necessary to pre-coat the pore walls, e.g. Al_2O_3 for Li [43] and SnO_2 for Na [38]. For sure, it is possible to apply this porous structure to positive electrode development. However, an effective method to infiltrate the active electrode materials, is still missing considering the few unsuccessful reports [43,65].

1.2 Na-based Batteries

Na-based batteries, another concept emphasized in this thesis, are promising candidates for stationary energy storage systems [66]. These stationary energy storage systems guarantee permanent power supply from fluctuating energy sources (e.g. solar and wind power) [66-68]. Systems for stationary applications need to meet lower requirements in terms of weight and volume, unlike those for mobile applications (e.g., cell phones and electric vehicles), while they are more sensitive to cost and scalability (up to MW units).

Present options for stationary systems include mechanical storage (pumped-storage hydro, compressed air, and flywheels) and batteries (mainly Li-ion and redox flow batteries) [67], which are still not satisfactory considering economic and environmental issues [69]. The characteristics of stationary storage systems offer ample scope for Na-based batteries, which are less mature than their lithium-based counterparts, but have advantages in terms of higher elemental abundance and lower cost of raw materials [66,68,70,71].

This part will describe the motivation of developing Na-based batteries, their pros and cons compared to Li-based batteries, as well as the combination of the concepts of ASSBs and Na-based batteries.

1.2.1 Na vs. Li

Na-based batteries are highly similar to their Li congeners. Li-ion batteries (LIBs) have become one of the most influential energy storage devices with the growing portable electronic market, and their importance is forecasted to grow further with the raising of electrical vehicles[3,72]. However, concerns about the price of raw materials for LIBs and even the reserve of Li materials also have grown in recent years[72]. Thus, researchers started to find possible alternatives to LIBs. Na-based batteries are viewed as a promising alternative, due to the similarity between the elements Na and Li.

Compared to Li, Na has a higher atomic weight (23.0 g mol⁻¹ vs. 6.94 g mol⁻¹), leading to a lower energy density of Na battery materials. However, considering that

mobile Na/Li ions only make a small fraction of the weight of the battery materials (e.g. 46.0 of 455.8 g mol⁻¹ in Na₃V₂P₃O₁₂ with a moderate specific mass capacity of 120 mAh g⁻¹), it is debatable that Na-based batteries will have a significant lower energy density. In addition, Na has a larger ionic radius (1.06 Å vs. 0.76 Å), which is especially critical to electrode materials, resulting in a higher volume change during electrochemical reactions. Another shortcoming of Na is a slightly higher potential (0.3 V) of Na metal than Li metal, which reduces the operation voltage of batteries using metallic anode. However, Na does enjoy some important advantages compared to Li, including a much lower price (\$150 per ton vs. \$5000 per ton, carbonate raw materials) and the abundance of Na resources (as 4th most abundant element on the earth) [72]. These properties indicate that Na-based batteries cannot be a total replacement of Li batteries, but can act as an ecologic and economical alternative, especially for stationary applications as discussed before.

It is worth noting that the comparison of Na and Li involves more factors when ASSBs are discussed. Ceramic sodium conductors usually has a higher conductivity than those of Li [73], which is probably enabled by a lower electronegativity of Na (0.93 vs. 0.98) [74]. On the negative electrode side, Na metal has a higher self-diffusion coefficient, a limitation to high rate cycling of ASSBs [33], which will enable Na-ASSBs with theoretically higher operation current density. Also, Na metal is softer than Li (0.69 MPa vs 5 MPa, Brinell hardness) [75], and thus easier to maintain contact with the ceramic electrolyte applying similar mechanical pressure. The larger radius of Na, together with higher volume change of electrode materials during cycling, will create more severe contact problem between electrode and electrolyte materials, as discussed in **Section 1.1.3**.

1.2.2 State-of-the-art Na-ASSBs in the Research Field

Similar to other kinds of ASSBs, Na-ASSBs are still on their early stage of development. What is worse, higher volume change happens in positive electrode materials for Na batteries. Thus, Na-ASSBs, built in a similar way, usually show a much higher degradation during cycling. **Table 1.1** summarizes the cycling performances of the state-of-the-art Na-ASSBs, compared to those of a Li-ASSB and

two Na-ion batteries with liquid electrolyte. Though Na-ASSBs with soft materials are able to operate at room temperature, no oxide-based Na-ASSB has been reported able to cycle at room temperature. Na-ASSBs operating at higher temperature still showed very fast degradation, also did thin-film Na-ASSBs. Their performances were much worse than those of Li-ASSBs and conventional Na-ion batteries, and were far from practical applications.

Table 1.1 Cycling performances of Na-ASSBs compared with an Li-ASSBs and Na-ion batteries with a liquid electrolyte

Ref.	Type	Compositions of materials (positive electrode electrolyte negative electrode)	Operating temperature (°C)	Current density ($\mu\text{A cm}^{-2}$) and C-rate, if available	Number of cycles	Degradation \checkmark after cycles	Specific capacity of active material (mAh g^{-1}) \checkmark
[76]	Na-ASSB with mixed positive electrode	NVP NZSP NVP	80	10	20	24%#	84#
[48]	Na-ASSB with mixed positive electrode	NVP NZSP NVP	200	486, 0.5C*	20*	55%#+	58#+
[41]	Na-ASSB with mixed positive electrode	NVP La-substituted NZSP Na	80	0.1C	40	35%#	107
[24]	Na-ASSB with soft electrolyte	NaCrO_2 $\text{Na}_2(\text{B}_{12}\text{H}_{12})_{0.5}(\text{B}_{10}\text{H}_{10})_{0.5}$ Na	65	0.2C	250	15%#	75
[22]	Na-ASSB with soft electrolyte	FeS_2 Na_3PS_4 Na	25	120	100	20%#	355#
[44]	Na-ASSB with polymer in positive electrode	$\text{Na}_2\text{MnFe}(\text{CN})_6$ +PEO+ NaClO_4 NZSP Na	60	180	200	11%	121
[49]	Li-ASSB mixed positive electrode	LiCoO_2 Li ₇ La ₃ Zr ₂ O ₁₂ Li	25	6, 0.05C	100	10%#	94#
[51]	Na-ASSB with thin film positive electrode	NaCoO_2 Sc-substituted NZSP Na	25	8, 0.15C	100	25%#	150
[77]	Na-ion battery with liquid electrolyte	NVP NaFSI+PC Na	RT	36, 0.1C	80	8%#	108#
[78]	Na-ion battery with liquid electrolyte	NVP+reduced graphene oxide-carbon nanotube NaClO_4 +PC+fluoroethylene carbonate Na	RT	10C	2000	4%	117

\checkmark Degradations are calculated from the first stable cycle, excluding first cycles with side reactions.

These numbers are calculated from figures.

+ Data from the middle of a test with various current densities.

1.3 $\text{Na}_3\text{V}_2(\text{PO}_4)_3$

$\text{Na}_3\text{V}_2(\text{PO}_4)_3$ (NVP) is a material with NaSICON structure and recently in the focus of research as a promising electrode material for sodium-ion batteries. NVP is used as the main positive electrode material studied in this thesis, and will be briefly introduced in this part.

NVP was first reported by Delmas et al. in 1978 [79] in a following research to the crucial discovery of NaSICON materials by Hong and Goodenough [80]. Afterwards, several reports were published on its structure [81-83], or on its potential as electrode material for Li-ion batteries [84]. In 2012, NVP started to be studied as the electrode material for Na-ion batteries by Jian et al. [85] and Kang et al. [86]. Since then, an increasing attention has focused on the material in the past 7 years, especially in 2014 and 2015.

In recent years, various materials have been designed as active materials for the positive electrode of Na-ion batteries, as introduced systematically by Guillon et al. [87]. NVP was chosen as the positive electrode material for batteries studied in this thesis, not only for its advantages as the positive electrode that has already been proven in previous reports, but also for its similar structure with the NaSICON electrolyte materials developed in our group.

1.3.1 Crystal structure

NVP is a polyanion material, normally with a rhombohedral (trigonal) structure and the space group of $R\bar{3}c$ with lattice parameters of $a = 8.7288(2) \text{ \AA}$, $c = 21.8042(7) \text{ \AA}$. [83] The crystal structure of NVP has been systematically investigated in previous studies [81,88-91], and a unit cell is shown in **Figure 1.8**.

Chotard et al. studied the alternative structures of NVP (α - and β -NVP) [90] with slightly modified lattice parameters. Also, various substitutions to the structure were studied in previous reports, e.g. the partial replacement of Na with Li and K [92]. K doped NVP showed a longer c-axis in the lattice and thus enlarged Na-ion diffusion pathway [93]. The replacement of V in NVP was also studied, including the

substitution with Fe [94], Cr [95], Al [96], and Mg [97]. Besides, Cushing et al. [84] partially replaced Na ions by Li ions in NVP by ion exchange method, and discovered that the Na ions in A(1) sites tend to remain immobilized in NVP, suggesting a direct A(2)-A(2) ion-transport mechanism in the material, as shown in **Figure 1.9**.

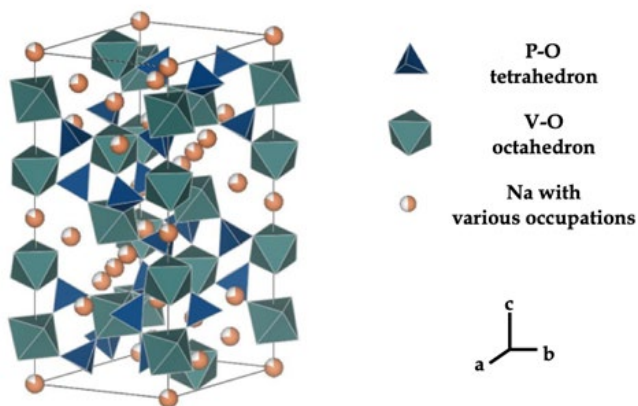


Figure 1.8 Crystal structure of NVP

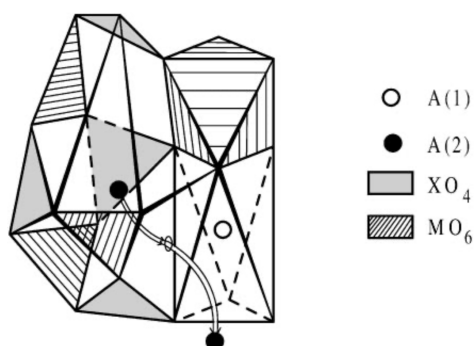


Figure 1.9 Ion transport pathway between adjacent A(2) sites in the rhombohedral NASICON structure [84]. (Reprinted with permission, license number: 4791840660443)

1.3.2 Synthesis methods

Till now, several methods have been used to synthesize NVP. The first and most commonly used method is solid-state reaction [77,96,98]. In order to reduce the particle size of NVP, sol-gel methods were also used [99,100]. Besides, some previous studies also tried pyro-synthesis [86], and electrostatic spray deposition [78].

During the synthesis, the reduction of vanadium is an important step. Most studies used a reduction atmosphere, Ar/H₂, during the sintering to convert V(V) to V(III). Another option is to add reducing agents in the starting materials, including oxalic acid [100,101], acetylene black [102], and sugar [77], with Ar atmosphere during sintering.

NVP crystals with small size were prepared for XRD measurements, using a self-flux in the system Na₄P₂O₇-NaVP₂O₇ [83]. Densification of NVP via sintering of pressed powder is difficult, since stabilizing V(III) requires a reducing atmosphere during sintering, in which P(V) is easily reduced.

1.3.3 Characterization of NVP

In order to optimize NVP as electrode material, different methods have been used to characterize it. This part will summarize the techniques used and some typical results. Details about the principles of most characterization techniques can be found in **Chapter II. Methodology**.

Microscopic methods

Microscopy methods, including SEM (scanning electron microscopy) and TEM (transmission electron microscopy), are commonly used to characterize the morphology of NVP powder. SEM is usually used to determine the size and morphology of particles, and TEM usually gives information about the carbon coating on the surface of NVP particles. It is noteworthy that most microscopic images were of the NVP powder, since it is difficult to prepare densified NVP. For a better visualizing of the carbon coating, Zhang et al. [101] used HCl to remove NVP, leaving only the carbon in their samples.

Diffraction and spectroscopic methods

X-ray diffraction (XRD) is commonly used to determine the lattice parameters and the atom positions in the crystal structure. XRD was mostly used to determine the phase purity, and in some cases the particle sizes of samples [100]. Lim et al. used high temperature XRD to study the thermal stability of NVP, which showed no change in the investigated range of 25 – 450 °C [88]. More importantly, Jian et al. carried out *in situ* XRD during the charge and discharge of NVP (Figure 1.10), and clearly showed the phase transformation during the process [77].

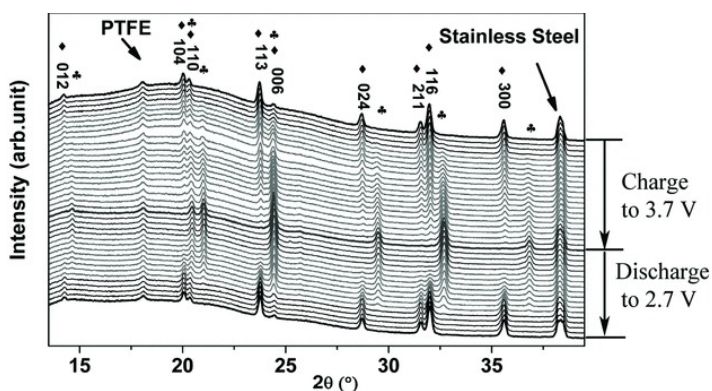


Figure 1.10 *In situ* XRD patterns of the $\text{Na}_3\text{V}_2(\text{PO}_4)_3/\text{Na}$ cell cycled between 3.7 and 2.7 V at a current rate of C/10, ◆ $\text{Na}_3\text{V}_2(\text{PO}_4)_3$, ♣ $\text{NaV}_2(\text{PO}_4)_3$ (Reprinted with permission, license number: 4734410985988)

X-ray photoelectron spectroscopy (XPS) and X-ray absorption spectroscopy (XAS) are both techniques able to determine the chemical state of elements. Thus, both methods were used previously to determine the oxidation state of vanadium. XPS was used in several papers, in order to measure the oxidation states of vanadium in the sample. Though, the oxidation states were hard to determine from the results, for peak positions vary greatly between different references [73,103-110]. Some useful information were given by Saravanan et al. [111], showing the chemical shift and restoration during charge and discharge of NVP. Similar to XPS, XAS is applied in several papers to determine the oxidation states of vanadium. Both XANES (X-ray

absorption near edge structure) and EXAFS (Extended X-Ray absorption fine structure) showed the chemical shift and restoration during charge and discharge of NVP [112,113].

Raman and IR (infrared spectroscopy) are common methods to detect the molecular and bond structure of materials, and are especially widely used on organic chemicals. These methods were also carried out on NVP samples. Raman spectroscopy is commonly used to characterize carbon in NVP samples, which is universally used as additive to improve the electronic conductivity of NVP. Almost all the papers on the carbon coated used Raman to analysis the state of carbon in their samples. Raman spectra with a wider spectral range show other bands, including the two bands between 250 and 500 cm^{-1} and the two around 1000 cm^{-1} (e.g. in **Figure 1.11**), which are common in different reports and probably the bands of NVP, though not analysed in those papers [77,85]. FTIR (Fourier transform infrared spectroscopy) was also used for the characterization of NVP in some papers, and gave information of different bonds in the structure. In a typical FTIR spectra of NVP, 577 and 1050 cm^{-1} peaks correspond to the P-O bonds, 629 and 978 cm^{-1} ones to V(III)-O bonds, while 760 and 950 cm^{-1} ones to V(V)-O bonds [88,102].

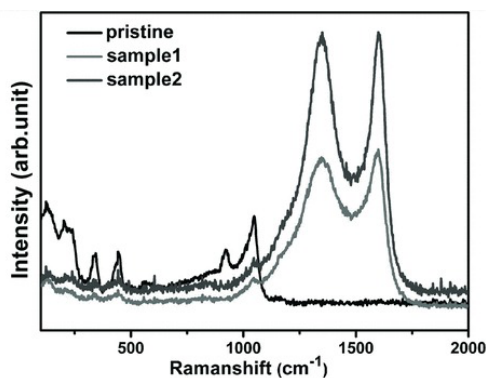


Figure 1.11 Raman spectra of the pristine $\text{Na}_3\text{V}_2(\text{PO}_4)_3$ and carbon coated NVP (sample 1 and sample 2) [77]

(Reprinted with permission, license number: 4860190716213)

Macroscopic methods (Thermal analysis)

Thermal analysis methods were commonly used to measure the carbon content of samples by heating the samples in air [85]. Inert atmosphere were used to analyse the sintering process or to check the thermal stability of samples. In Ar, DTA (differential thermal analysis) peaks between 643 and 720 °C indicate the formation of NVP crystals in a solid-state reaction from the raw materials of Na_2CO_3 , $\text{NH}_4\text{H}_2\text{PO}_4$, V_2O_5 , and acetylene black [102].

Electrical and electrochemical properties

NVP can act as both positive and negative electrode material, with two phase transformations: $\text{NaV}_2\text{P}_3\text{O}_{12}$ - $\text{Na}_3\text{V}_2\text{P}_3\text{O}_{12}$ - $\text{Na}_4\text{V}_2\text{P}_3\text{O}_{12}$ [85], as shown in **Figure 1.12** [88]. In the previous reaction, vanadium (III) is oxidized to vanadium (IV) at the potential of about 3.4 V vs. Na^+/Na , giving a specific capacity of about 120 mAh g^{-1} ; in the latter one, vanadium (III) is reduced to V(II/III) at about 1.7 V with about 60 mAh g^{-1} [85]. It should be noticed that the potentials of $\text{Na}_3\text{V}_2\text{P}_3\text{O}_{12}$ - $\text{Na}_4\text{V}_2\text{P}_3\text{O}_{12}$ reaction observed in experiments ($\sim 1.7 \text{ V}$) were lower than that simulated ($\sim 2.0 \text{ V}$ in **Figure 1.12**).

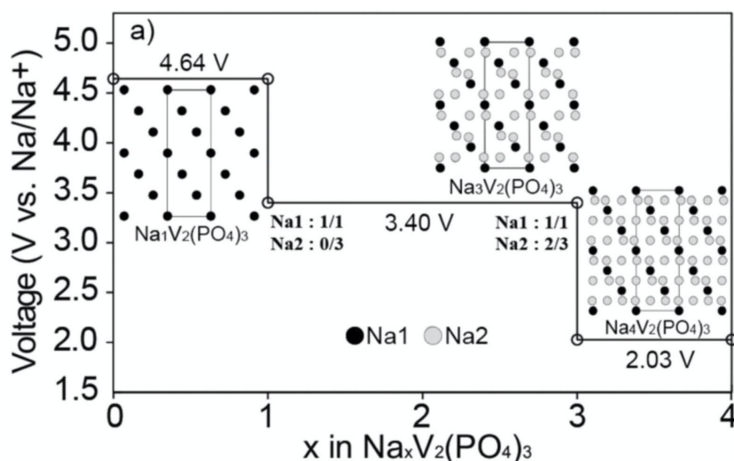


Figure 1.12 Voltage profiles estimated from first principle calculations [88]
(Reprinted with permission, license number: 1010281-1)

Carbon coating is commonly deposited on NVP in order to improve the electronic conductivity in systems using liquid electrolyte. Mostly, amorphous carbon was used as coating [114]. Other kinds of carbon include porous carbon matrix [101,115], carbon nanotubes [116-118], hierarchical carbon framework [119], hierarchical carbon nanofibers [120], reduced graphene oxide [121,122], and nitrogen-doped carbon (nanotubes and reduced graphene oxide) [98].

Although the majority of papers on NVP used carbon-coating and other methods to improve the electronic conductivity of NVP, the conductivity was just mentioned as "low" in most papers. Some paper gave such an inference with no reference or citing another paper without real data [78,80,85,86,91,97-101,114,120,123-139]; some indicated that the V-O-P connection in NVP has a large energy difference between V3d and O2p orbitals [123,126,138], and that biphasic reaction owing to the large lattice volume change during (de)sodiation [138]. However, no calculation based on this theory has been made till now. Chekannikov et al. [100] measured the impedance of carbon coated NVP, and Li et al. [97] carried out a direct current measurement, but only on carbon-coated samples, other than NVP itself. Also, measurements of NVP particles surrounded by liquid electrolyte are not accurate.

1.4 Scope of this Thesis

The main goal of this thesis is to design, fabricate, test, and optimize positive electrodes for Na-ASSBs using $\text{Na}_3\text{V}_2\text{P}_3\text{O}_{12}$ (NVP), $\text{Na}_{3.4}\text{Zr}_2\text{Si}_{2.4}\text{P}_{0.6}\text{O}_{12}$ (NZSP) and metallic Na as battery materials. In order to achieve this aim, theoretical and experimental work was performed to solve the following problems:

A deeper understanding of the physical and electrochemical properties of NVP

For this target, research work has been carried out on the synthesis, purification, densification, and characterization of NVP.

A new structural design of positive electrodes

Based on previously reported designs, a backbone-infiltration route was selected with the aim to enable higher efficiency of electrochemical reactions and higher tolerance to volume change of the electrode material.

A realistic process to fabricate the ASSBs, as well as optimization with respect to systematic tests, characterizations, and analysis

The whole process of cell preparation needs to be studied: the fabrication of electrolyte layer and the backbone of electrolyte material in the electrode composite, the preparation of precursor solution of active electrode material, the infiltration of precursor solution, the conversion of the dried components of the solution into active electrode material by calcination, the attachment of metal electrode, and the final assembly of cells.

A series of electrochemical tests have been performed to evaluate the prepared ASSBs, supported by post-test characterization.

A view on the possible practical application of the design compared to other ASSB designs

Based on all the results, an outlook is given about further application of the design and the fabricating method, regarding the scalability, the energy density, and the practicability of ASSBs.

II Methodology

2.1 Synthesis Methods

2.1.1 Powder Synthesis

NVP powder was synthesized in this thesis for physical characterization and as electrode materials for battery cells with liquid electrolyte. The synthesis process contains the following two steps: mixing raw materials and heat-treating the mixture.

For the first step, two methods, solid-state reaction and Pechini (sol-gel) synthesis, were used to mix the raw materials. Solid-state reaction, as the name tells, is a method of mixing raw materials as powders. In this thesis, the mixing was done by ball milling the raw materials in a PE (Polyethylene) bottle on a roller bench, with ZrO₂ balls and ethanol. This method is simple with no limitation to the solubility of raw materials, and was able to provide pure NVP powder in previous studies [77,98,140]. However, it turned out that the method was not entirely “solid-state” in the studies of this thesis, and will be discussed in detail in **Section 3.2.1**. The Pechini method [141], as one type of sol-gel synthesis, is able to produce fine powder with small particle sizes. The method starts from an aqueous solution of all raw materials, and later all the cations are well dispersed by polymerized citric acid and ethylene glycol. In this thesis, the precursor produced by Pechini was then heat-treated in reducing Ar/H₂, and the organic chemicals were carbonized. The carbon *in situ* synthesized together with NVP powder benefits the electronic conductivity of the powder, and thus Pechini method was used to produce electrode materials for battery cells with liquid electrolyte. For physical characterization of the material, however, carbon influences the properties as impurity.

In addition, different raw materials were studied for their influence on purity of the product. Na₂CO₃, NaNO₃ and NaH₂PO₄ were studied as source of Na in NVP. Na₂CO₃ is a commonly used Na salt for synthesis. However in the case of this thesis, Na₂CO₃ appeared to be an improper raw material, since the mixed precursor was acidic and CO₂ was released during room temperature mixing (usually done in a

close PE bottle). NaNO_3 was also not preferred, for releasing NO_x during heat-treatment. NaH_2PO_4 was used for most synthesis in this thesis, which has the same stoichiometry as NVP of elements Na and P and lowers the possibility of insufficient mixing. As the source of V in NVP, V_2O_5 and NH_4VO_3 were used. V_2O_5 is a proper raw material for solid-state reaction, and is easy handling as rough powder. NH_4VO_3 is fluffy with smaller particle size, but is necessary for Pechini reaction with a higher solubility in acidic solution. NaH_2PO_4 and $\text{NH}_4\text{H}_2\text{PO}_4$ were studied as the source of P in NVP.

The heat-treatment step was similar for all methods, with a reducing Ar/ H_2 (4 vol. %) atmosphere. The maximum temperature (740 - 900 °C) and the holding time (2 h - 4 h) varied.

2.1.2 Purification and densification of NVP

Carbon was found to be the main impurity in NVP. Thus, oxidation of carbon was the main process of the purification, which, however, also oxidized some raw materials. The oxidation irreversibly destroyed the homogeneity of the precursor. Thus, a series of experiments was carried out by adjusting the sequence of different steps during the synthesis: milling (by hand in a mortar or with balls), oxidation to remove carbon, and reduction to form NVP phase. Details about the experiments are introduced and discussed in **Section 3.2.1**.

The densification of NVP, from powder to a monolithic sample, appeared to be difficult and has not been done in previous reports. NVP is usually synthesized in reduced atmosphere to obtain the V(III) in the material. In Ar/ H_2 , 900 °C is not high enough for the densification for NVP, but is nearly the upper limit before the decomposition of NVP with the reduction of P(V). Different methods were tried to densify NVP, introduced in details in **Section 3.2.2**.

2.1.3 NVP precursor solution with high vanadium concentration

NVP precursor solution was made by mixing ethanolamine (Merck), de-ionized H_2O , NaH_2PO_4 (Sigma-Aldrich), citric acid (Sigma-Aldrich), and NH_4VO_3 (Merck) (weight

ratio 1:2:0.71:1:0.46). Citric acid provided extra carbon after heat-treatment and was added in some batches of solution used.

2.2 Fabrication of Na-ASSBs

2.2.1 Fabrication of Na-ASSBs with thin layer NVP as positive electrode

Na-ASSBs with thin layer NVP electrode was made by dropping NVP precursor solution onto sintered NZSP ($\text{Na}_{3.4}\text{Zr}_2\text{Si}_{2.4}\text{P}_{0.6}\text{O}_{12}$) pellets, followed by heat-treatment.

NZSP powder was synthesized by a solution-assisted solid-state reaction [46,142], by solving NaNO_3 (VWR), $\text{ZrO}(\text{NO}_3)_2$ (Aldrich), $\text{Si}(\text{OCH}_2\text{CH}_3)_4$ (Merck), and $\text{NH}_4\text{H}_2\text{PO}_4$ (Merck) in de-ionized H_2O . The mixture was dried at 85°C and then calcined at 800°C for 3 h. The calcined powder was milled in ethanol with zirconia balls on a milling bench for 48 h and then dried at 70°C for 12 h. NZSP powder was put into a cylindrical pressing mould (diameter 13 mm), and then pressed into pellets using a uniaxial press with a pressure of 90 MPa. The pressed pellets were sintered in air at 1280°C for 6 h to obtain the NZSP pellets.

NVP precursor solution (without citric acid) was described in **Section 2.1.3**. Drop of the solution was deposited onto the surface. The pellets were then heat treated at 740°C in Ar-4 % H_2 for 4 h to form the NVP crystalline phase. Au was then sputtered on the positive electrodes to serve as current collector. Sodium (Sigma-Aldrich) was attached manually to the opposite surface of the NZSP pellet in an Ar-filled glove-box. The cells were sealed in Swagelok cells after assembling.

2.2.2 Fabrication of Na-ASSBs using chemical infiltration

In this thesis, a new method of Na-ASSB fabrication is developed, by combining the infiltration of precursor solution into a porous electrolyte scaffold with an *in situ* synthesis of the active material. **Figure 2.1** shows the steps of the fabrication process, which are outlined in detail in the following parts. The development of the method is further discussed in **Section 4.1** and **Section 4.2**.

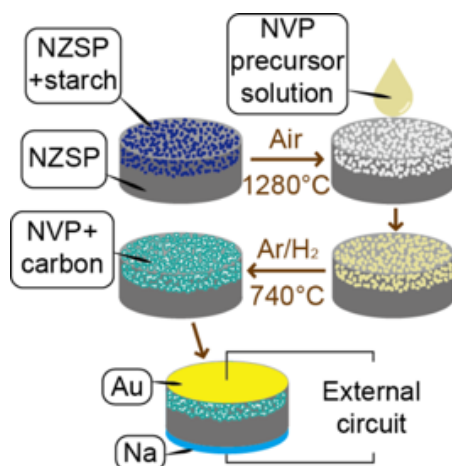


Figure 2.1 Manufacturing steps for an NVP-NZSP-Na battery using the chemical infiltration method

Electrolyte & positive electrode backbone

NZSP powder was synthesized as described in **Section 2.2.1**.

Part of the NZSP powder was mixed with 10 wt. % rice starch (BENEO-Remy) by ball-milling in ethanol for 24 h. 0.3-0.4 g NZSP powder and 20-50 mg of the mixture made above were put into a cylindrical pressing mould (diameter 13 mm) layer by layer, and then pressed into pellets using a uniaxial press with a pressure of 90 MPa. The pressed pellets were sintered in air at 1280 °C for 6 h to produce the dense-porous bi-layered NZSP pellets. After sintering, the porous layer is about 150-250 μm thick, and the dense layer is about 600-800 μm thick. Different amount (20 and 30 wt. %) of rice starch in the mixture were also studied, as discussed in **Section 4.2.1**.

Infiltration

NVP precursor solution (**Section 2.1.3**) was deposited onto the surface of the porous layer for infiltration and propagated by capillary force.

The pellets were then heat treated at 740 °C in Ar-4 %H₂ for 4 h to form the NVP crystalline phase. The infiltration and heating process was repeated 3 times to obtain the desired loading of active material and establish continuous electronic pathways.

Cell Assembly

Au was then sputtered on the positive electrodes to serve as current collector. Sodium metal (Sigma-Aldrich) was attached manually to the surface of the dense layer of NZSP in an Ar-filled glove-box. The cells were sealed in Swagelok cells after assembling.

2.3 Characterization methods

2.3.1 Diffractive and spectroscopic methods

XRD

X-ray diffraction (XRD) is a common method to identify atomic and molecular structure of a crystalline material.

During the measurement, a beam of incident X-rays is targeted on the sample and diffracted by the electrons. The electrons, influenced by X-ray waves of electromagnetic radiation, scatter the waves keeping the same frequency, known as Rayleigh scattering (or elastic scattering). These scattering waves may interfere with each other either constructively or destructively, and only those constructive interferences are strong enough to be detected as diffractions [143]. The interference of waves can be calculated via Fourier integral, and thus the reciprocal space (Fourier transformed real space) is usually used to understand the diffraction conditions. In a crystal, as a lattice of points of equal symmetry, the condition for constructive interference is that: the reciprocal momentum of the scattering wave meet a reciprocal point of the crystal. For a given incident radiation with wavelength λ , the scattering wave has the same wavelength and has reciprocal momentums with same length of $2\pi/\lambda$, which point to the surface of a sphere (Ewald sphere[144]). The constructive interference happens, quite obviously, where the Ewald sphere meets the reciprocal lattice of the crystal. In a polycrystalline sample, there exist many randomly oriented crystals. Thus, their reciprocal lattice also forms a series of concentric spheres (centred at the origin of the reciprocal space), and constructive interference happens when their surface meet that of the Ewald sphere (with the origin on its surface).

By measuring the direction and intensities of the diffracted beams, the density of electrons in the crystal can be calculated. Many information can be analysed from the electron density, including the atom positions and chemical bonds. The diffractions of polycrystalline samples are usually presented as an XRD pattern, in which intensity is drawn against direction diffraction angle. The XRD pattern is the

characteristic information for a polycrystalline sample, but also influenced by preferred orientation and overlapping of different phases.

In this thesis, XRD patterns of different samples were measured using a Bruker D8 DISCOVER diffractometer with Cu K_{α} radiation at room temperature. The crystal structures were analysed by the Rietveld method using FullProf-suite software [145] in cooperation with other institutions. Schematic crystal structures were illustrated by VESTA software [146]. XRD was also used to analysis the phase transition during the electrochemical cycling of Na-ASSBs with an *in situ* XRD technique. Na-ASSB cells were sealed in a special sample holder with a Kapton window, which allows X-ray penetration and enables the *in situ* XRD analysis during their cycling. *In situ* XRD measurements were performed using a Bruker D8 DISCOVER diffractometer with Cu K_{α} radiation at room temperature.

XPS

X-ray photoelectron spectroscopy (XPS) is a surface-sensitive spectroscopic technique that can measure the elemental components of the sample. During an XPS measurement, the sample is irradiated with a beam of X-rays, meanwhile the kinetic energy and number of electrons that are ejected from the surface are recorded. Usually, the XPS result is plotted as a spectrum with the number of electrons versus the energy of the electrons (binding energy). Each element, other than hydrogen and helium, has a series of XPS peaks at characteristic binding energies, which correspond to the electron configuration of the atoms. The position of a peak is also influenced by the chemical state of an atom, which includes the oxidation state, the bonding environment (neighbour atoms) etc. The influence is usually called "chemical shift". Thus, XPS is a useful tool to help understanding the chemistry states of elements on the surface (0~20 nm) of a material.

Usually two modes of scanning are adopted. A survey spectrum shows all the elements detected on the tested surface. A high-resolution spectrum focuses on the narrow area around some specific peaks, and gives detailed information for further analysis of the chemical shift. For example, when vanadium is the target element of an XPS measurement, the peaks corresponding to the 2p electron shell of the

vanadium atom (named V-2p peaks) is used to determine the chemical shift of this element. In a high-resolution spectrum, there are two V-2p peaks, corresponding to the 2p 1/2 and 2p 3/2 electrons. These two peaks have a constant difference of binding energies, thus the position of the 2p 3/2 electron is usually used for the determination of chemical shift. **Table 2.1** below summarizes some reported positions of the V-2p 3/2.

Table 2.1 Positions of 2p 3/2 peak of vanadium

Chemical	Oxidation state of V	Position of V-2p peak	Reference
V ₂ O ₃	III	513.1	[106]
V ₂ O ₃	III	515.8	[104]
V ₂ O ₃	III	516.8	[107]
V ₂ O ₃	III	517.2	[147]
VO ₂	IV	516.3	[73]
V ₂ O ₅	V	516.6	[73]
V ₂ O ₅	V	517.2	[105]
V ₂ O ₅	V	517.7	[103]
VOPO ₄	IV ¹	516.9	[109]
VOPO ₄	V	518.5	[109]

In this thesis, XPS was used to study vanadium in NVP. XPS measurements were operated in ZEA-3, Forschungszentrum Jülich, on NVP samples made by solid-state reaction (Na₂CO₃, NH₄H₂PO₄ and V₂O₅, air@530 °C - Ar/H₂@850 °C), and also on NVP-NZSP mixture. Bar-shaped samples were kept in a Ar-filled atmosphere, and XPS measurements were done on fresh cross sections. The chemical shifts of vanadium are strongly influenced by its chemical environment, and are very sensitive to various conditions. The differences between reference values of the same oxidation state are sometimes larger than the differences between different states, as shown in **Table 2**. XPS results of NVP in this thesis cannot be interpreted accurately in terms of chemical states, which will be discussed in more detail in **Section 3.1.1**.

¹ According to the reference, there are V(IV) signals in the XPS result of the VOPO₄ sample

Raman

Raman spectroscopy is a technique to determine vibrational modes of molecules, influenced by the polarizability of the electrons. During the measurement, laser is targeted on the sample surface and the photons excite the irradiated sample area into a higher vibrational state. The excitation then ends with photons emitted as Raman scattering. The difference of wavenumbers of excitation light and scattering light is named Raman shift, and a Raman spectrum is drawn as intensity against Raman shift.

For battery materials, Raman spectroscopy is commonly used to characterize carbon. In a Raman spectrum, two bands at 1350 cm^{-1} (named D-band) and 1600 cm^{-1} (G-band) are assigned to carbon. The D/G intensity ratio (I_D/I_G) can provide the gauge for the amount of structural defects. The higher I_D/I_G is, the more amorphous the carbon is [135,136].

In this thesis, Renishaw inVia Raman microscope is used to detect the existence of carbon on the surface tested. Combined with optical microscopy (with white light source), the relation between colours in the optical microscopic image and existence of carbon could be identified. Thus, the distribution of carbon in samples could be confirmed. The analysis will be discussed in detail in **Section 3.1.1**.

NMR

Nuclear magnetic resonance (NMR) spectroscopy is a technique analysing the structure of small molecules with high precision. During an NMR measurement, the local magnetic fields around atomic nuclei are observed by detecting the excitation of the sample by radio waves with changing frequencies. In an NMR spectrum the signal intensity is plotted against the chemical shift. Chemical shift is calculated as the quotient of relative resonance frequency of the sample divided by the absolute resonance frequency of a standard reference compound and is usually expressed in parts per million (ppm). There are different kinds of nuclei that are NMR active, and the ^1H and ^{13}C are most commonly used, which give characteristic spectra for various kinds of organic chemicals.

In this thesis, ^{13}C -NMR (Bruker Avance 600-MHz spectrometer) was performed in ZEA-3, Forschungszentrum Jülich, and was used to analyse the composition of NVP precursor made by solid-state reaction, in which unknown organic chemicals were observed.

2.3.2 Macroscopic methods (Thermal analysis)

TG/DTA with MS

Thermogravimetry / differential thermal analysis (TG/DTA) is a simultaneous macroscopic characterization technique, in which the mass of a sample, as well as the calorimetric response of the sample, are measured over time as the temperature changes.

In a TG report, the mass and the temperature are recorded and usually are plotted against each other. In a TG/DTA measurement, a reference also undergoes the same heat-treatment with the sample. Thermal changes in the sample, exothermic or endothermic, can thus be detected. Sometimes a mass spectrometer (MS) can be coupled with TG/DTA, giving the molecular mass of the released gas. During the MS measurement, the molecules are ionized and the mass can be measured by the radius of the ion's path in the magnetic field.

In this thesis, TG/DTA was carried out with a STA449 F1 Jupiter instrument, which is coupled with a QMS 403C Aëolos MS detector.

GC-MS

The gas chromatography (GC) is a system to identify different organic molecules. A GC system contains a capillary column, and different molecules with different chemical properties will separate when traveling through the length of the column. The molecules are retained by the column and then eluted from the column at different retention times. Subsequently the MS will detect the mass-to-charge ratio of the ions. The combination of the two systems allows a better substance identification than either unit used separately.

In this thesis, GC-MS was operated in combination with ^{13}C -NMR, in order to give a better interpretation of the NMR results.

Optical Characterisations

In this thesis, photos, that describes the macroscopic morphology of the samples, are obtained via various devices, including: iPhone 6S plus (Apple Inc.) and iPhone XS max (Apple Inc.) for most photos; TOMMIplus (Fraunhofer ISC) optical dilatometer for photos taken during heat-treatments.

2.3.3 Microscopic methods

Two types of microscopic methods were used in this thesis to characterize samples: scanning electron microscopy (SEM) and scanning transmission electron microscopy (STEM).

SEM produces images of a sample by scanning the sample surface with a focused beam of electrons. The electrons interact with atoms in the sample, and the interaction produces various signals with information about the observed surface. The scanning is made in a raster pattern, and the image is generated by visualizing the intensity of the detected signals at the beam position. Common signals used include secondary electrons, backscattered electrons, and X-rays. Secondary electrons are emitted by atoms excited by the electron beam and give information about the surface morphology. Backscattered electrons are detected after the elastic scattering of the beam electrons from specimen atoms. Since the backscatter strength is proportional to the atomic number, backscattered electrons images are able to differentiate areas with different chemical compositions. X-rays are also released by excited atoms, and are usually analysed in an energy-dispersive X-ray spectroscopy (EDS). A given element has specific energies of the released X-ray. Thus, an EDS spectrum is obtained as intensity vs. energy (in eV): the positions (energies) of peaks in the spectrum represents the detected elements, and the peak intensities scale with the amount of the element.

STEM is very similar to SEM, but scan samples with small thickness that allow the electrons to pass through and is able to produce images with much higher magnification. The most common signal for morphological analysis is named high-angle annular dark-field electron (HAADF). In HAADF technique, the image is made by detecting high angle, incoherently scattered electrons (Rutherford

scattering), and thus, the contrast in the image is sensitive to variations in the atomic number of atoms [148].

Samples usually require a special preparation process before being ready for SEM/STEM measurements. For SEM analysis, samples are observed on their surface, or on an internal plane (cross-section) exposed by breaking or polishing. For STEM analysis, the thickness of the sample is usually reduced by cutting of a focused ion beam (FIB).

In this thesis, the microstructure of the positive electrodes was investigated with a ZEISS Merlin SEM. The cross section of some samples was polished by an Ar cross-section polisher (JEOL, SM-09010), since the electrode active material (NVP) is shaped in thin film and breaks easily during mechanical polishing. In order to estimate the fractions of the electrode layer, the software Analysis pro was used to measure the size of pore area in SEM images. FIB (FEI Helios NanoLab 400S) was used to cut thin lamella from the positive electrode part. The lamellae specimens before and after the electrochemical tests were then investigated by STEM (FEI Titan 80-200 Chemi-STEM), which is equipped with a Super-X EDS system. NZSP is sensitive to electron-beam irradiation, making it difficult to carry out high-resolution STEM studies of the interface structure.

2.3.4 Electrochemical tests

The electrochemical tests of battery cells are usually carried out using an electrochemical testing system. In this thesis, Biologic VMP-300 system used, and samples are kept at the constant temperature of 25 °C in a climate chamber (Vötsch, VT4002) during measurements. This section will introduce the main electrochemical tests performed with typical analysis on the test results.

PEIS

PEIS (Potentiostatic Electrochemical Impedance Spectroscopy) is an impedance spectroscopy method with a constant potential difference between electrodes of the cell.

During the measurement of an impedance spectrum, an alternating current with changing frequency is applied on the sample, the dielectric properties of the sample are recorded as a function of the frequency. The sample is usually interpreted as a passive complex electrical system, comprising both energy dissipater (resistor) and energy storage (capacitor) elements. The reaction of the complex system to the alternating current applied is also represented by a complex number, i.e. impedance. An impedance spectroscopy is usually expressed graphically in a Bode plot (magnitude and phase of impedance against frequency) or a Nyquist plot (parametric plot of magnitude on a complex plane with real part as x-axis and imaginary part as y-axis). The analysis of impedance spectra is complex and an accurate interpretation usually requires control experiment. In this thesis, the analysis is based on previously reported curves and their interpretations.

For battery cells, it is necessary to use PEIS test mode to ensure the steady-state during the impedance measurement, since the potential of the electrode material, directly related to the chemical state, has a significant influence on its dielectric properties.

In this thesis, PEIS was carried out on Na-ASSBs with thin layer NVP positive electrode, at various temperatures and at various potentials. The temperature was controlled by the climate chamber, with a 2-hour rest time after each change. The potential was controlled using MB (Modulo Bat) technique, holding the battery cell at a given potential for at least 12 hours to ensure the steady-state conditions. The Nyquist plots were compared with those of pure NZSP pellets, and among themselves with changing temperature and potential. Then, the contribution of NVP layer was interpreted. Detailed analysis can be found in **Section 3.2**.

For Na-ASSBs made by chemical infiltration, PEIS of the cell only provided limited information about the cell, which is discussed in detail in **Section 4.3.2**.

CV

Cyclic voltammetry (CV) is a potentiodynamic electrochemical measurement. In a CV measurement, the cell potential is ramped linearly versus time, back and forth in many cycles, and the current is recorded. The result is plotted with current against

potential, and peaks in the curves represents electrochemical reactions. For reversible reactions, peaks with different direction (in current) couple with each other. CV peaks, during slow potential ramping, are very sensitive to reactions, thus is commonly used for unknown electrochemical systems. However, CV measurements are unable to give directly quantified information about the capacity of the cell.

GCPL

Galvanostatic Cycling with Potential Limitation (GCPL) is a method that cycles the cell with constant current between specific voltages, as the name tells (galvano = of current). GCPL displays the operation of a battery cell in real application, giving direct information about its performance.

A series of parameters are important during a GCPL measurement, including the current density of each charge/discharge process, the start and end potential of each process, and the constant potential period or open circuit voltage (OCV) period after each process. The current density is chosen based on the estimation of the cell capacity, and the cell's ability to operate at high C-rates. The most commonly C-rates used for long time cycling of a cell is 0.05C and 0.1C. An additional type of GCPL analysis is named C-rate test, in which the same cell is cycled with changing C-rates. In C-rate tests, the current density (C-rate) first increase (usually from 0.1C) every few cycles, and then reverse to the initial C-rate in the final cycles. Such a C-rate test gives information about the stability of the tested cell against fast charging/discharging. The start and end potential of each process is chosen based on the operation voltage of the cell. The investigated NVP-NZSP-Na system has a potential plateau of around 3.4 V, and thus most cells were cycled between 2.8 and 3.8 V. For cell systems with a slope change of potential, a wider range of cycling potential is usually chosen. The process after each charge/discharge step, either the potential is held with changing current density recorded, or the current density is set to 0 with the changing potential recorded, gives information whether the electrode material is charged to an equilibrium state. For cells with large capacity, the

potential holding period helps to avoid instant polarization when the orientation of current density is changed between charge and discharge steps.

There are various ways of presenting a GCPL result. Charge/discharge curves are parametrically plotted with potential against capacity. The shape of a curve gives information about the changing of electrode materials' state in electrochemical reactions. In this thesis, the NVP-NZSP-Na cells show a nearly flat plateau in charge/discharge curves, and the potential difference between two curves of the same cycle is caused by the internal resistance of the cell (multiplied by 2 times of the current density). It is also very common to summarize the discharge capacity and Coulombic efficiency of each cycle. From the change of discharge capacity during cycling, the fading or degradation of a cell can be calculated. In addition, in a C-rate test, the cell stability on current density can be quantified by the discharge capacities. A series of GCPL was carried out, and results are discussed in **Section 4.3**.

III Synthesis and Characterization of NVP

NVP is a promising positive electrode material for Na-ion batteries and has long been a focus of research. Though various characterizations have been made on NVP as electrode material for batteries with liquid electrolyte, limited information is known about the pure material. Therefore the initial attempt was the preparation of NVP and its densification to study the physical properties. In this chapter, the study on the purification of NVP is introduced, followed by the unsuccessful densification of the material, and finally the measurement of its conductivity is reported based on a new structured Na-ASSB that avoids the densification problem.

3.1 Preparation of NVP samples

3.1.1 Purification of NVP

Phase purity depending on raw materials

Various synthesis methods and raw materials for NVP have been reported in recent years (**Section 1.3.2**). In order to fabricate pure NVP sample, solid-state reaction method was mainly studied, since the polymerized citric acid and ethylene glycol is easier to remain in the precursor and get carbonized during the following heat-treatment in reducing Ar/H₂.

Experiments were also made to study the influence of raw materials. **Figure 3.1** shows the XRD patterns of NVP phase prepared from different raw materials. NVP made from NaH₂PO₄ showed the highest purity, with no visible peak from impurities in the XRD pattern. This is probably due to the fixed stoichiometry of elements Na and P. By contrast, in samples using separate sources for Na and P, impurities with different stoichiometry of elements Na and P could be found: NaVP₂O₇, Na₄P₂O₇, and NaPO₃. V₂O₅ as a raw material also remained as impurity after the synthesis, though V₂O₅ is easier to handle than the other V source, the fluffy powder of NH₄VO₃. Based on these results, NVP in the following studies of the thesis was synthesized from NaH₂PO₄ of NH₄VO₃ via solid-state reaction method.

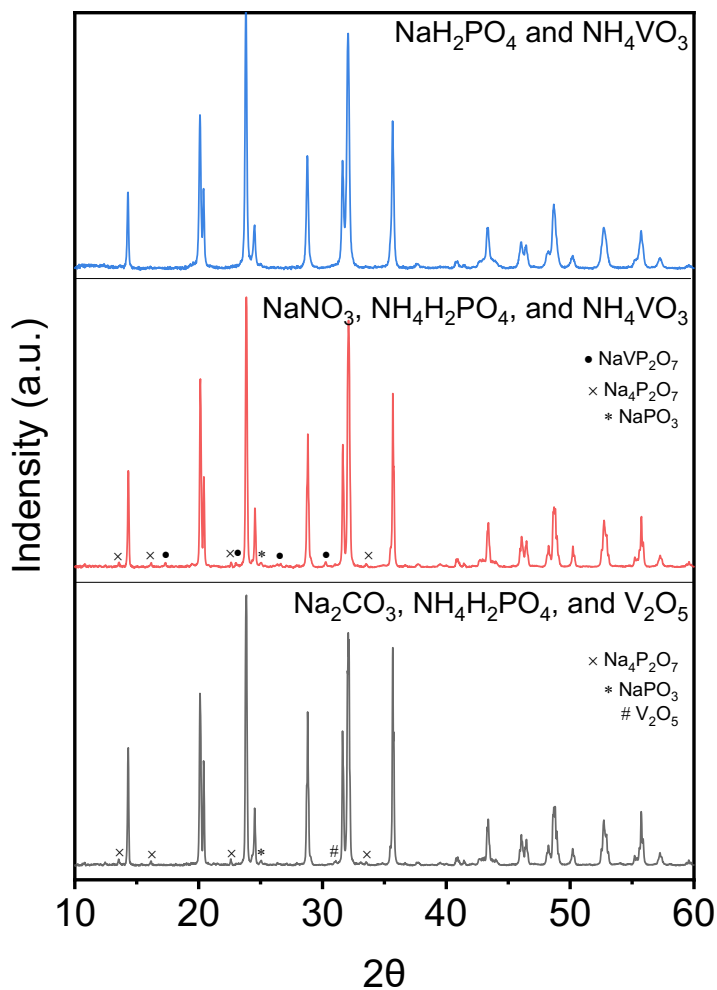


Figure 3.1 XRD patterns of NVP made from different raw materials

Origin of black colour in NVP samples

NVP samples were always obtained in black colour. For those made by Pechini method, the black colour is probably from carbon, which is the product of the reduction of organics. However, samples made by solid-state reaction also showed a

black colour. In this case, ethanol as a possible source will be discussed later in this section. In NVP powder prepared as electrode material for batteries, carbon is not harmful but even beneficial for increasing the electronic conductivity. In NVP samples for fundamental characterization, in contrast, carbon will influence the result. It is worthy studying the origin of carbon and how to remove it. Moreover, since the addition of crystallized carbon (nanotubes, graphite etc.) is common as a composite with NVP, it is also important to control other source of carbon in the samples, to get a clearer understanding of the function of additives.

The black colour is not necessarily resulting from carbon, but also from the mixed oxidation state of vanadium, which was studied with XPS. Typical survey spectra of NVP samples are shown in **Figure 3.2**. It is worth noting that carbon peaks exists in both spectra. The intensity of carbon signals in the mixture is higher. **Figure 3.3** shows the high-resolution spectra of the V-2p signals. The peak fitting results are given as the most possible interpretation according to the database, showing that the vanadium in both samples has a mixed oxidation state of IV and V. The result, however, is contradictory to electrochemical tests, showing a oxidation state of III (2.9 V vs. Na/Na⁺, after a longer exposition in air during cell processing). The error is possibly due to XPS as a surface-sensitive method, while the oxidation state of the surface can easily change without significant change of the sample as a whole. It is possible that NVP was not totally reduced during heat-treatment, and oxidation of vanadium during the experiment was also possible, even though all the measurements were done on freshly exposed cross-sections.

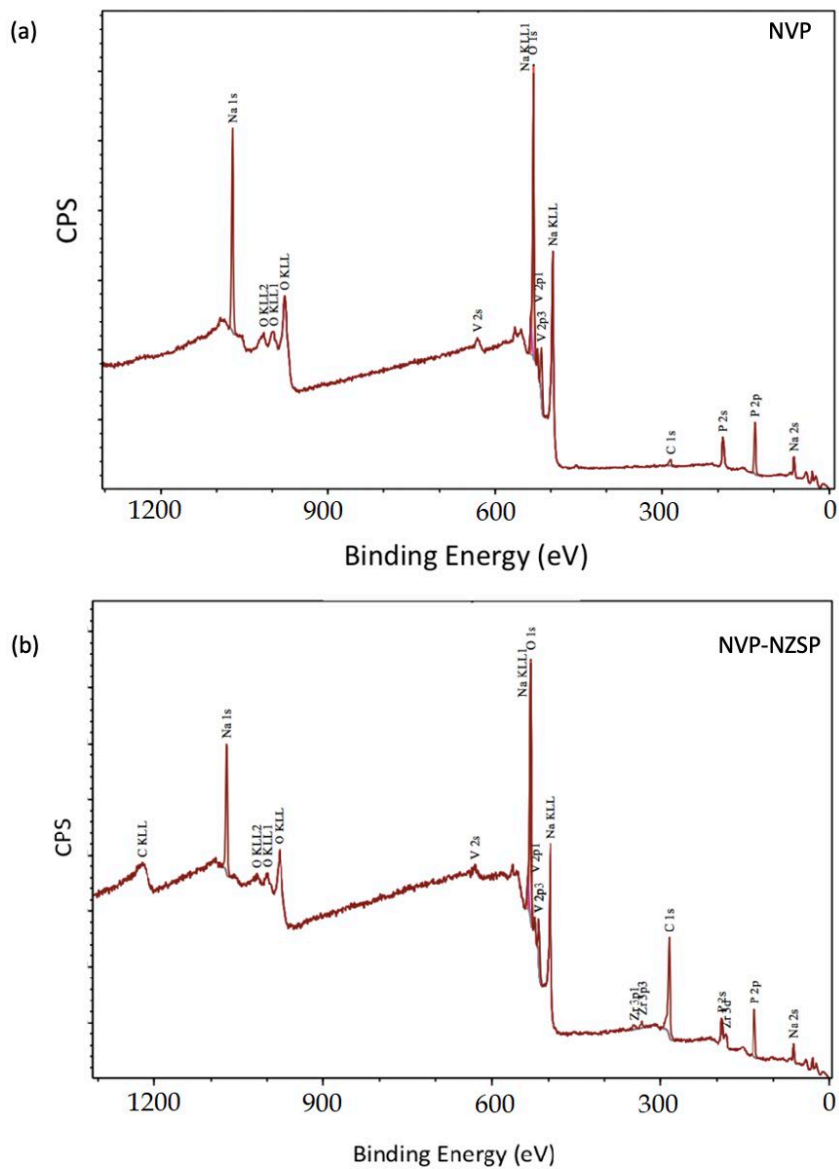


Figure 3.2 Survey spectra of NVP: (a) pure NVP sample; (b) NVP-NZSP mixture

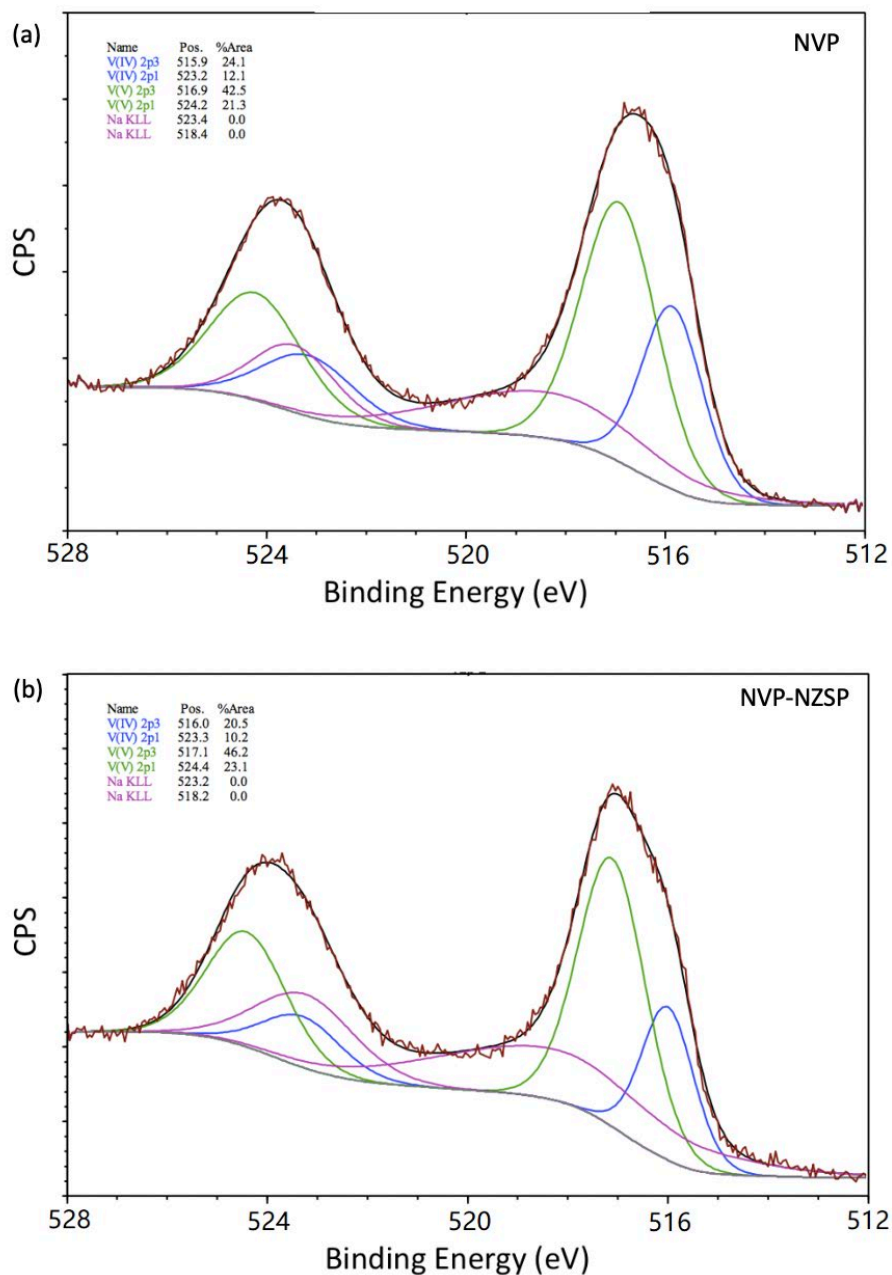


Figure 3.3 High-resolution spectra of NVP: a. pure NVP sample; b. NVP-NZSP mixture

Further analysis was made by TG/DTA, which also gave an indication on how to remove carbon. As shown in **Figure 3.4**, TG/DTA measurement was made in air on

NVP sample prepared by solid-state reaction. Although, no carbonate or organic starting materials were used, mass loss could be observed from the starting of heating up to about 470 °C. This drop was possibly the release of H₂O and the oxidation of carbon in the sample and was proven by mass-spectroscopy later. Further, a raise in mass occurred from 470 °C to about 570 °C, possibly caused by the oxidation of NVP. Mass spectroscopy measurement was made combined with DTA/TG, and the results are also shown below in **Figure 3.4**. All the possible gases released from the sample were detected, and signals of other molecular weight were negligible compared to those of M=18, M=44 and M=12, which were supposed to be H₂O, CO₂ and C. Combined with the DTA results above, conclusion could be drawn that carbon exists in the sample, and the oxidation of carbon (3 wt. %) caused the mass loss. Also, there is a sharp peak at about 540 °C, combined with a release of C and CO₂. However, in order to avoid any reaction between air and NVP, it is not possible to calcine samples to 540 °C during heat-treatments.

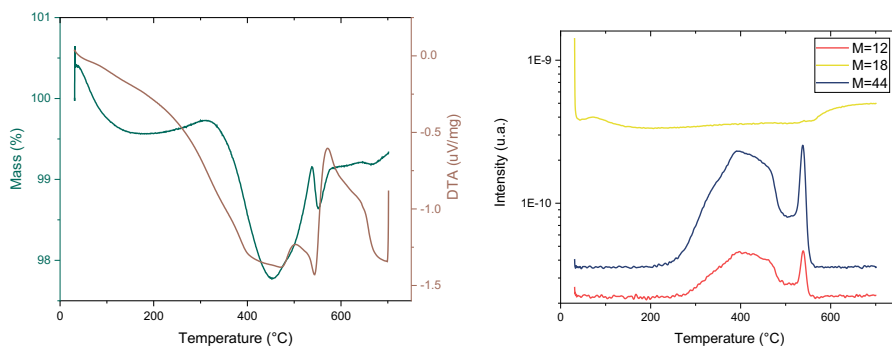


Figure 3.4 TG/DTA results of NVP sample in air, and the mass spectroscopy during the measurement

According to the results, carbon existed in NVP samples made via solid-state reaction. Heat treatments to remove carbon can be made at 400 °C to 450 °C. The temperature is enough for the removal of carbon, since the release of CO₂ during

DTA measurement reached its peak at 400 °C. The amount of carbon remained in the sample above 470 °C should be further evaluated.

Origin and removal of carbon in NVP

Though carbon was detected in black-coloured NVP samples, the origin of carbon is still unclear, since samples prepared without carbonate as starting material and synthesized by solid-state reaction (without organic gel formation) still contained significant amount of, well-distributed carbon. Thus, other possible source of carbon should be examined carefully, especially ethanol, which is used during ball milling.

An experiment was designed to verify the influence of ethanol, and the possibility to prepare carbon-free samples. Starting materials were ball milled in ethanol for 72 h, and then dried in an explosion-protected oven for 12 h. Afterwards, some powder was oxidized at 400°C in air as pellets (named as "Sample O"), then reduced at 780°C in Ar/H₂. Sample that was reduced directly after the oxidation is named "Sample OR". Another sample that was firstly hand milled and then pressed again before reduction is named as "Sample OhR", and a third sample was ball milled (in ethanol) as "Sample ObR". Some powder was reduced in Ar/H₂ as pellets (Sample R), and then oxidized (Sample RO). Every pellet was kept in a vacuum oven for at least 18 h before further processes. A brief sketch for the design of the experiment and resulting samples is shown in **Figure 3.5**.

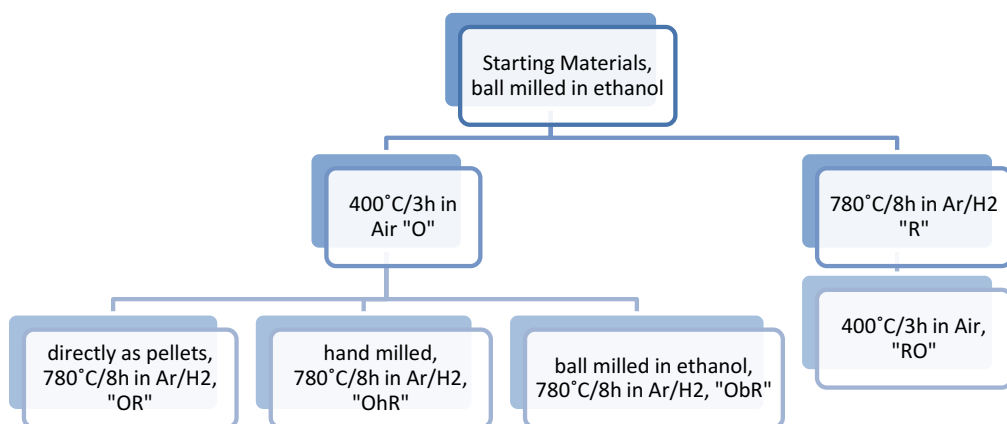


Figure 3.5 The experimental design of samples

Each sample was checked with XRD on the phase purity and with Raman on carbon existence. The XRD patterns are shown in **Figure 3.6**.

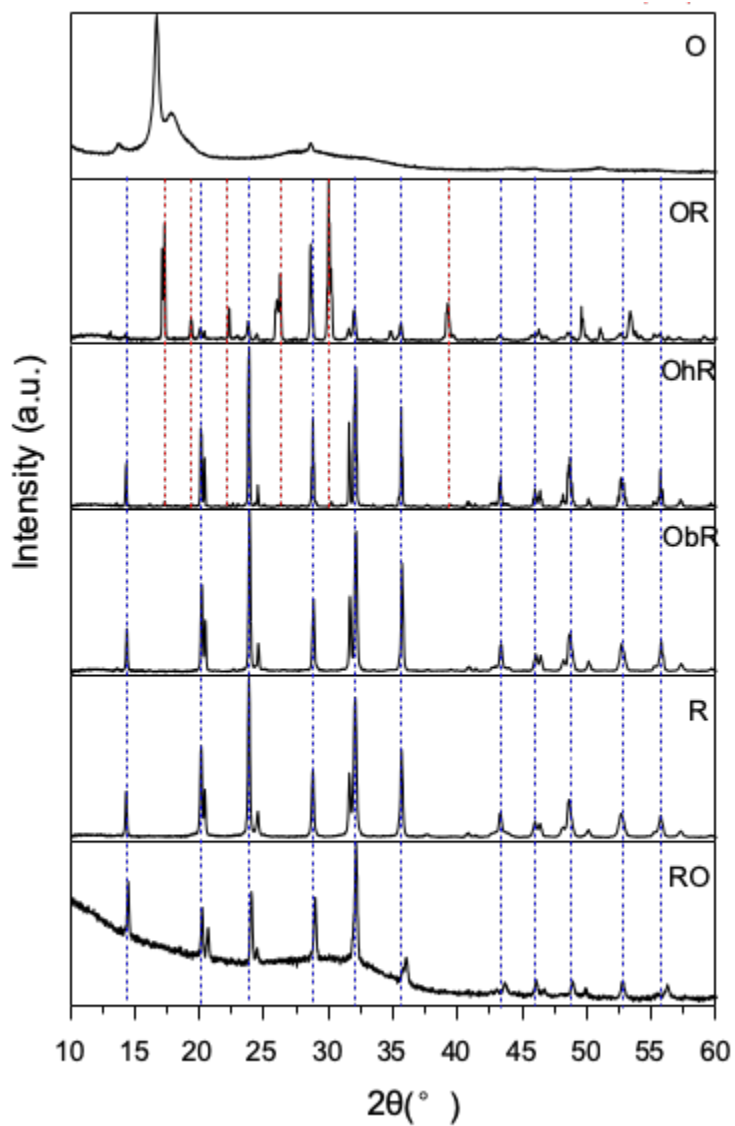


Figure 3.6 XRD patterns of samples mentioned in **Figure 3.5**. Blue lines are reflections of NVP, and red lines are those of NaVP₂O₇

In **Figure 3.6**, Sample R is the normally synthesized NVP sample as a reference, showing high phase purity. After oxidation, Sample O became amorphous, and the only peaks cognizable are of P_2O_5 . In the samples that were oxidized in the first step (Samples OR, ObR, and OhR), only the ball-milled one (ObR) showed good phase purity after further reduction. A possible reason is that during the oxidation the homogeneity is destroyed and some of the intermediates cannot react to NVP later in Ar/ H_2 , but to some other phases (e.g. $NaVP_2O_7$ shown in the patterns). The only difference is the ratio of starting materials [149]. Sample OR was mainly $NaVP_2O_7$, showing only minor amounts of NVP. In Sample OhR, the content of $NaVP_2O_7$ was still high. $NaVP_2O_7$ is also a polyanion material and has a similar process of synthesis as $Na_3V_2(PO_4)_3$. For Sample RO, the oxidation destabilized the sample, which became predominantly amorphous, though peaks of NVP could still be found. The sample was very fragile after the process.

The Raman results are shown in **Figure 3.7**, with the optical microscopic images of the areas measured. In Samples OR and OhR, the peaks of carbon were not detected, and the patterns were similar to references [77,85] (**Figure 1.11**), and the peaks probably belonged to NVP. There were two areas in Sample OR, and the outer part is darker in colour than the inner part. Their Raman spectra, however, had only slight differences. Thus the colour did not come from carbon. The carbon peaks in Samples ObR and R were strong. In the spectrum of Sample R, the signals of NVP could still be observed. In Sample RO, no carbon was observed, and the pattern was different from the first three ones, indicating a different composition. The existence of carbon in the samples is summarized below with XRD results.

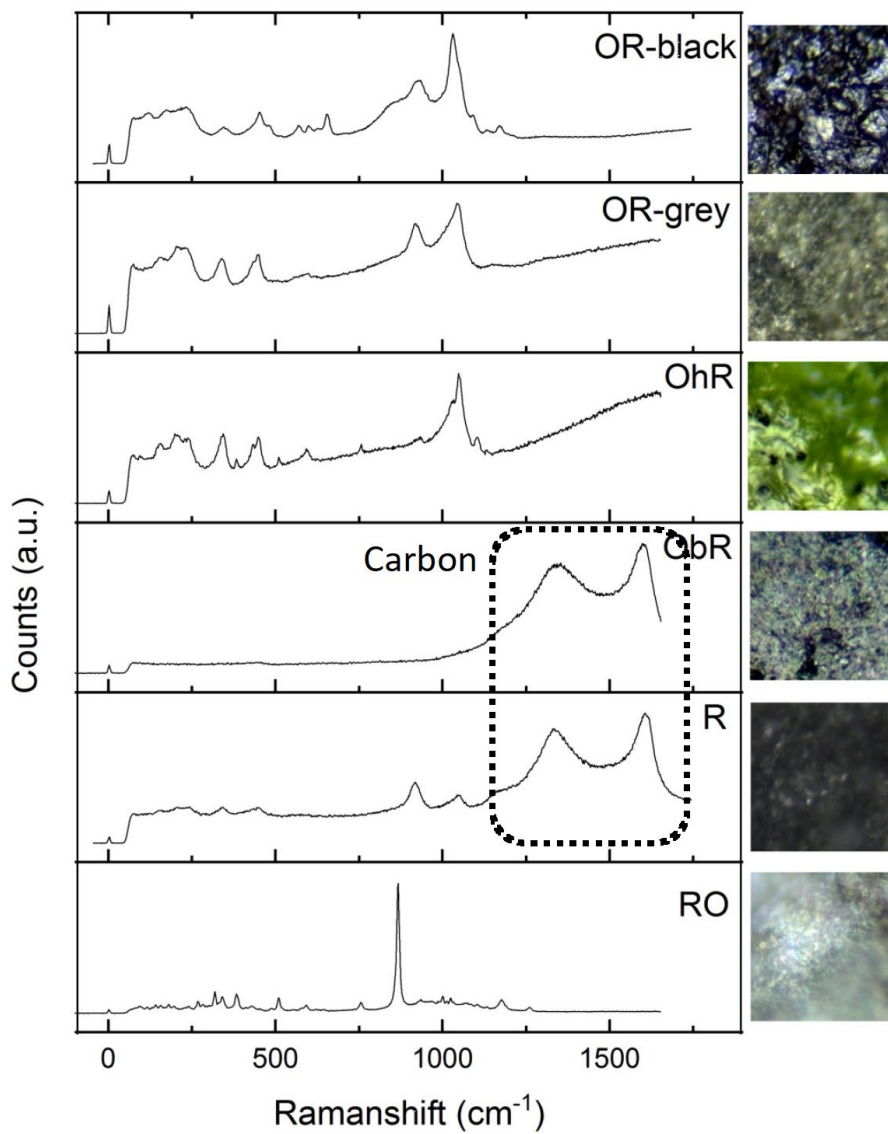


Figure 3.7 Raman spectra of sample mentioned in **Figure 3.5**, with optical microscopic images

Table 3.1 Raman and XRD results of NVP samples

Sample	Carbon Existence	Phase Purity	Comments
OR	no	mainly other phases	partially melted
OhR	no	with impurity peaks of NaVP ₂ O ₇	partially melted
ObR	yes	pure phase	
R	yes	pure phase	
RO	no	partly NVP and partly amorphous	very fragile

From the results, we can see that the heat treatment of 400 °C in air for 3 hours is enough to remove carbon in NVP samples. The oxidation was effective either before or after reduction. It is especially worth noticing that the Sample OhR and Sample ObR experienced similar process of preparation, the only difference being the contact of ethanol. The existence of carbon which should have been oxidized in previous process was obviously a result of the ethanol used in ball milling. This also proved that by keeping the pressed pellets in a vacuum oven, ethanol could not be completely removed.

Moreover, a lot of phenomena in the experiments above indicated that ethanol did not simply adhere on NVP particles, but actually reduced the vanadium during a mechanochemical synthesis, in which raw materials (NaH₂PO₄, V₂O₅) were mixed by ball milling in ethanol. The first phenomenon observed was that ethanol was not removed by keeping the sample in a vacuum furnace. Second, a colour change from yellow to green was observed as shown in **Figure 3.8 (a)**, which indicated the reduction of vanadium. Third, after the ball milling, the smell of the liquid was obviously different from that of ethanol. And last, the size of NVP particles was abnormally small for products from ball milling, as shown in **Figure 3.8 (b)**.

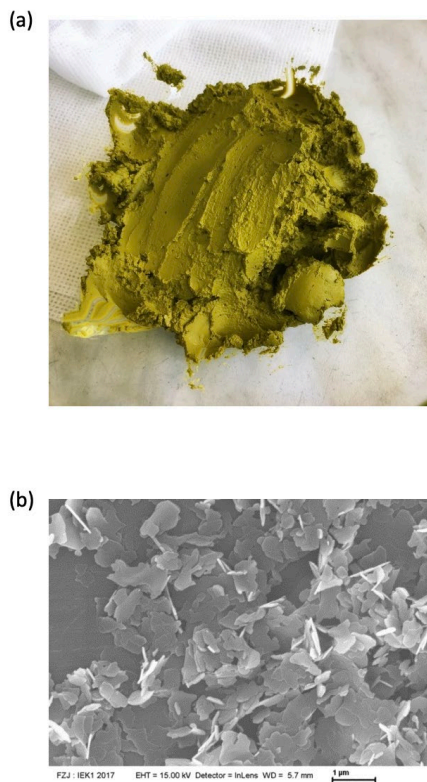


Figure 3.8 (a) Photo of $\text{NaH}_2\text{PO}_4 - \text{V}_2\text{O}_5$ mixture after ball-milling in ethanol; (b) SEM image of NVP precursor after ball-milling

^{13}C nuclear magnetic resonance spectroscopy (NMR) and coupled gas chromatography with mass spectrometry (GC-MS) were used to determine organic chemicals before and after the ball-milling. The measurements were carried out at ZEA-3 by Dr. Willbold. Samples for these investigations were prepared as before with a mixture of NaH_2PO_4 and V_2O_5 ball-milled in ethanol for 24 hours. The pristine ethanol used was taken as a comparison. In this report, ^{13}C -NMR spectra were measured on samples before and after ball-milling, and the results are shown in **Figure 3.9**. In the spectrum of ethanol before ball milling, there are only three peaks. Changes appeared after ball milling, indicating the change of organic chemicals, especially more resonance peaks in the area right of 50 ppm, which corresponds to C in C-O, C=C and C=O structures. However, these signals come

from different organic chemicals with relatively low concentrations. It is worth noting that both methods above require samples in a liquid phase, and the sample was the liquid part from the milling bottle after 2 hours of settling of the solid. So it is possible that some of the organics could not be detected in the measurements. In addition, a direct interpretation of chemicals was impossible from these spectra. In the liquid part of the sample after sedimentation, ethanol was still the dominate phase, but more organic chemicals with $c=c$ and $c=o$ bonds appeared after the ball milling.

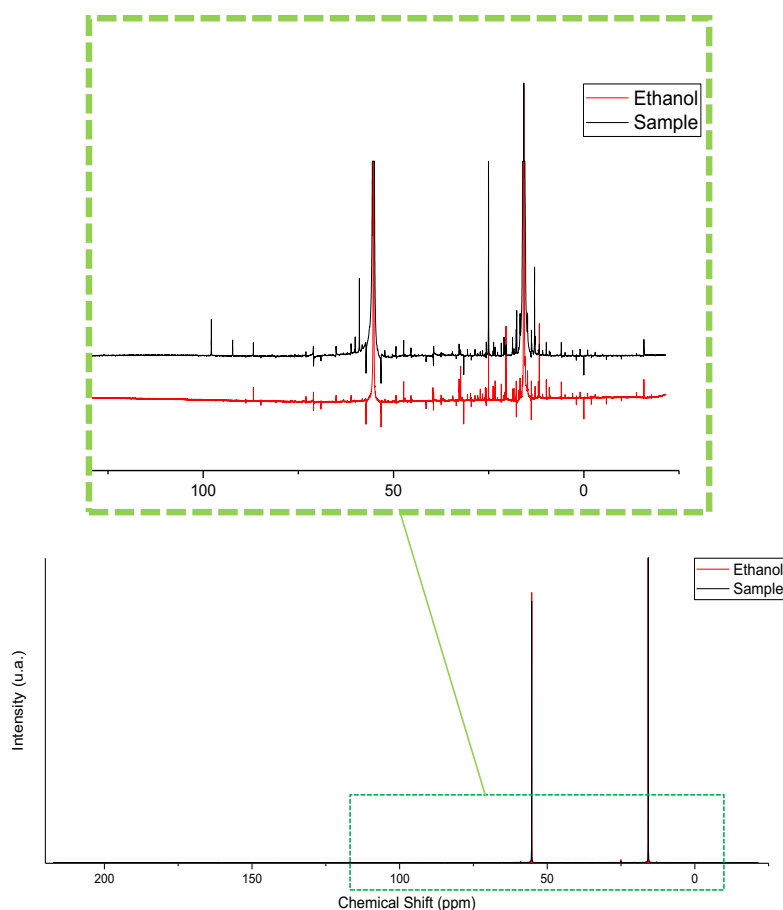


Figure 3.9 NMR spectra of sample after ball-milling and the ethanol used

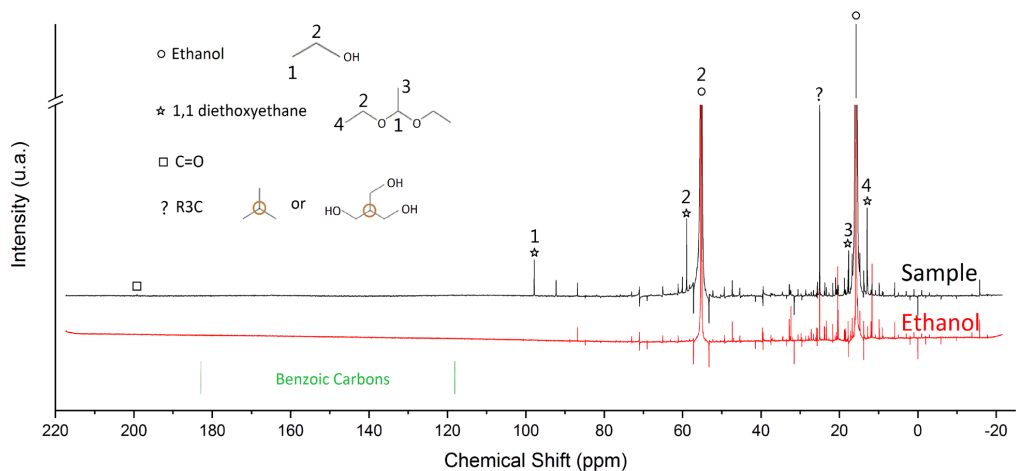
GC-MS was carried out on the liquid after ball-milling, and the result is summarized in **Table 3.2**. A series of compounds were detected in the sample, which did not exist in the ethanol used for ball milling. Though GC-MS cannot give fully quantified information about the composition, it provided a clue for further interpretation of the NMR spectra.

Combined with GC-MS results, a further interpretation of the NMR spectra can be made, as shown in **Figure 3.10**. Carbons in 1,1 diethoxyethane can be clearly identified in the spectrum of the sample, as relatively stronger peaks. Another strong peak that exists only in the sample belongs to carbon connected to 3 other carbons, which, however, cannot be assigned to any compounds detected in GC-MS.

The existence of 1,1 diethoxyethane meets well with the NMR results, and is a strong evidence of the oxidation of ethanol by the V(V) in the raw material. The reaction is a possible reason of the difficulties in removing carbon from NVP sample made by solid-state reaction.

Table 3.2 GC-MS results of ethanol before and after ball milling

Retention time (min)	Ethanol	Sample after ball-milling
1.52	not found	1,1 diethoxyethane
2.20	polyethyleneglycole	not found
10.30	not found	benzoic acid
10.92	not found	ethyl benzoate
12.69	not found	unable to determine
13.33	not found	phosphate compound
14.39	not found	unable to determine
14.92	not found	unable to determine
16.71	not found	unable to determine
17.98	ethyl benzene	not found
20.68	1nitro, 2,4 dimethylbenzene	1nitro, 2,4 dimethylbenzene

**Figure 3.10** Assignment of NMR peaks based on GC-MS results

3.2 Conductivity of NVP measured on Na-ASSBs with thin layer NVP

Special Na-ASSB cells were prepared to measure the conductivity of NVP, since it has been proved rather difficult to prepare a bulk NVP sample with high purity and density in **Section 3.1**. By forming a thin layer of NVP on the surface of a sintered NZSP pellet, it is guaranteed that NVP, with known and quantifiable geometric factors, is detected during an impedance measurement.[150]²

Figure 3.11 shows the typical cross-section of the NVP layer on NZSP. NVP formed a discontinuous layer with similar thickness. The average thickness was 1.7 μm , as calculated from 10 different SEM images. The weight of NVP in this sample was 233.72 μg , measured by chemical analysis afterwards. Thus, the area of the NVP layer was 0.42 cm^2 , or 54% of the whole pellet. Metallic Na was attached to the other side of the NZSP pellet, and the PEISes of the cell were measured at various voltages at RT. This cell structure is very similar to NZSP or Na|NZSP|Na cells reported previously [46], which helps to impetrate the PEIS results.

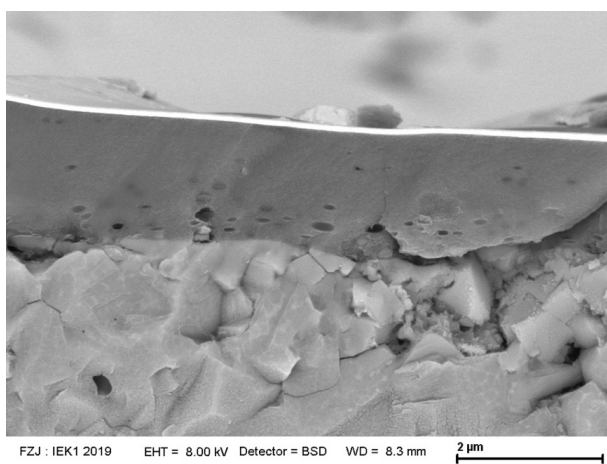


Figure 3.11 SEM image of a typical cross-section of NVP layer (darker contrast) on a NZSP pellet (lighter contrast particles with edges).

² Data of this section was published [150] after the defence of this thesis, together with further analysis on the distributions of relaxation times (DRT) of the PEIS results.

Since the Na negative electrode kept unchanged during the measurement, the voltage of the cell equalled the potential of NVP (vs. Na^+/Na). PEIS was measured at voltages with smaller steps around 3.4 V, when the electrode reaction $\text{Na}_3\text{V}_2\text{P}_3\text{O}_{12} - \text{NaV}_2\text{P}_3\text{O}_{12}$ happens.

The PEIS of the NVP|NZSP|Na cell has two semi-circles visible in each Nyquist plot, as shown in **Figure 3.12**. The first and smaller one has exactly the same frequencies and comparable diameters with that of NZSP grain boundary reported previously [46]. This semicircle kept unchanged with changing voltage of the cell. Some other cell components are expected to be invisible in this experimental setting: NZSP bulk responses to higher frequency and usually invisible on the left of the NZSP grain boundary semicircle [94]; Na has very small impedance, whose semicircle is hid under second large one. Thus, the second semi-circle, changing with cell voltages, represents the reaction of NVP, which depends on the different potentials of the material.

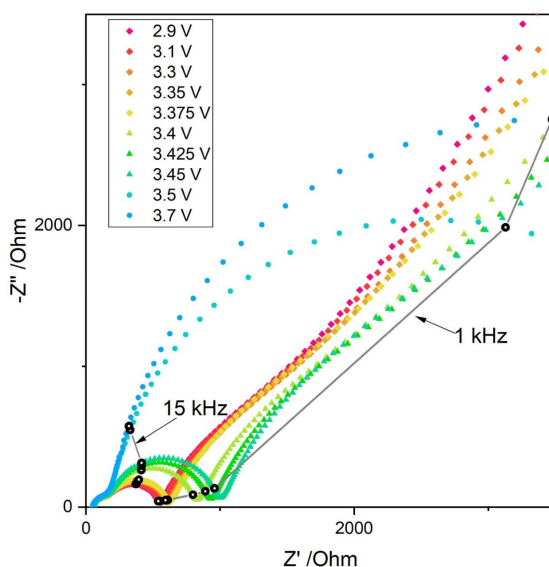


Figure 3.12 Nyquist plots of the PEIS results measured on a NVP|NZSP|Na cell at various voltages (connected circles showing results obtained at 15 kHz and 1 kHz current frequency)

Conductivities of NVP at various potentials were calculated by the geometric factors shown before, as summarized in **Figure 3.13**. From 2.9 V to 3.375V, the conductivity decreased slightly around $1 \times 10^{-6} \text{ S cm}^{-1}$, probably due to the extraction of Na^+ . During the $\text{Na}_3\text{V}_2\text{P}_3\text{O}_{12} - \text{NaV}_2\text{P}_3\text{O}_{12}$ reaction, the conductivity of the material decreased a lot to $8 \times 10^{-8} \text{ S cm}^{-1}$ with increasing potential, as a result of the lattice shrinkage. Ionic conductivity contributed most to the total conductivity, since the electronic conductivity from similar materials was reported to be around $2 \times 10^{-9} \text{ S cm}^{-1}$ [151]. After the reaction, $\text{NaV}_2\text{P}_3\text{O}_{12}$ phase shown a much lower conductivity than that of $\text{Na}_3\text{V}_2\text{P}_3\text{O}_{12}$. This change meets well with the correlation between crystal structures and conductivities reported in other NaSICON materials [152]. At various potentials, the conductivities of NVP are much lower than that of NZSP, typically $1 - 5 \times 10^{-3} \text{ S cm}^{-1}$.

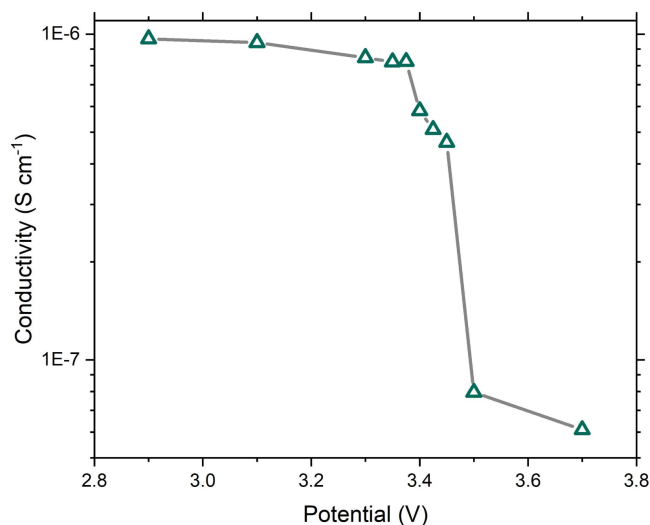


Figure 3.13 Potential dependency of conductivities of NVP

In summary, normal method consisting of powder synthesis and sintering failed to produce pure and dense bulk-type NVP sample. This is mainly due to the reaction between vanadium and organic additives during the synthesis, producing flake-

shaped particles that are difficult to compact during the sintering. Also, the co-existing of V(III) and P(V) in NVP limits the suitable temperature during sintering. By using a solution assisted method, a dense layer of NVP was deposited on the surface of NZSP and the conductivity of NVP was measured for the first time in this thesis, with controlled geometric factors in a ASSB cell. At 25°C, NVP showed a conductivity of $1 \times 10^{-6} \text{ S cm}^{-1}$ at 2.9 V, and the conductivity decreased with a higher potential of NVP, to $8 \times 10^{-8} \text{ S cm}^{-1}$ at 3.5 V. This low conductivity, especially at higher voltages, requires small particle sizes for NVP in electrode composites, in order to reduce the ohmic polarization and concentration polarization.

IV Na-ASSBs Prepared by Chemical Infiltration

As discussed in **Chapter I**, ceramic-based ASSBs suffer from severe contact problems in the positive electrodes and unsatisfactory cell performance, although ceramic ion conductors are promising electrolyte materials for ASSBs, due to their high conductivity, as well as good mechanical, chemical, and thermodynamic stability. Here, a solution to the inter-ceramic contact problems is provided, combining the *in situ* synthesis of electrode active material and infiltration of a porous electrolyte scaffold by precursor solution (named as chemical infiltration).

This chapter gives a detailed introduction to chemical infiltration, including the design, the process of the method, and the fabricated model cells using NVP, NZSP, and Na as the positive electrode, electrolyte and negative electrode materials, respectively. In the end of the chapter, an outlook of the work, as well as more possibilities about this method, are given. Design, data, and analysis of this section was published [36,150,153].

4.1 Design

Design of electrode structure

The positive electrode of ceramic-based ASSBs is usually prepared by powder mixing of electrode and electrolyte materials followed by a co-sintering step [34,41,49,76,140]. Electrodes prepared by this method often have a random, dense microstructure with grain and interfaces originating from the high temperature thermal treatment (as shown schematically in **Figure 4.1a**). This microstructure leads to non-optimized Na-ion transfer and contact damage caused by volume changes of the electrode material during charging and discharging. In addition, the co-sintering process frequently leads to incompatible sintering conditions: either the contacts are poorly formed at low temperatures or there are chemical reactions of the two materials at elevated temperatures, leading to the formation of new, undesired phases.

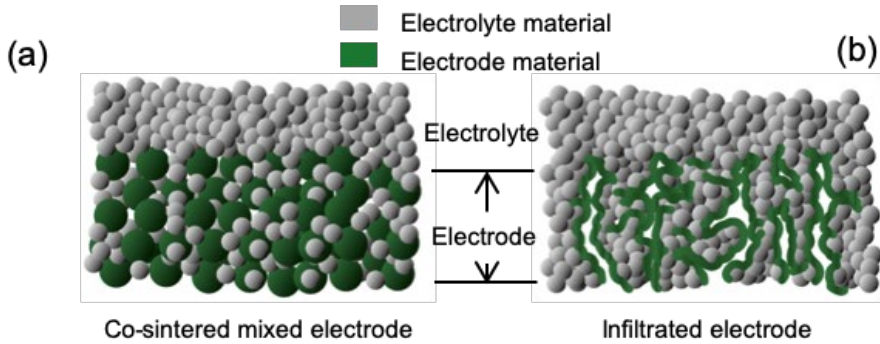


Figure 4.1 Schematics of typical electrode microstructure by different processing routes.

A new electrode design (**Figure 4.1b**) can be achieved by adopting chemical infiltration. Chemical infiltration is a combination of infiltration and *in situ* synthesis of the electrode material. The method is inspired by the manufacture of solid oxide cells (SOCs), whose electrochemical performance also depends strongly on the contact between two ceramic materials [55-57,154]. In the new electrode design, a skeleton of the electrolyte material with open porosity is first sintered as a backbone; afterwards, the precursor solution of the electrode material is infiltrated and the targeted phase is formed by *in situ* synthesis on the accessed pore walls. The use of a sintered backbone of electrolyte material ensures effective ion transport. Meanwhile, the remaining porosity after infiltration can accommodate the strain induced by volume change of the electrode material. In terms of contact between materials, the obtained structure combines the benefits of thin-film electrodes and bulk electrodes, by enabling a high effectiveness of the electrochemical reaction and reducing the influence of volume change during operation, while maintaining scalability.

Material Selection

In this thesis, the NVP | NZSP | Na system chosen also brings benefits due to the similar crystal structure NVP and NZSP share [85,155]. **Figure 4.2** presents the crystal structure of morphotropic NZSP and NVP.

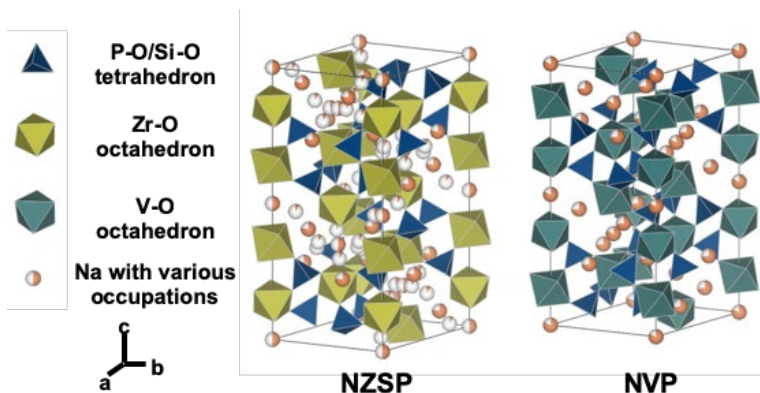


Figure 4.2 Schematic crystal structure of NVP and NZSP

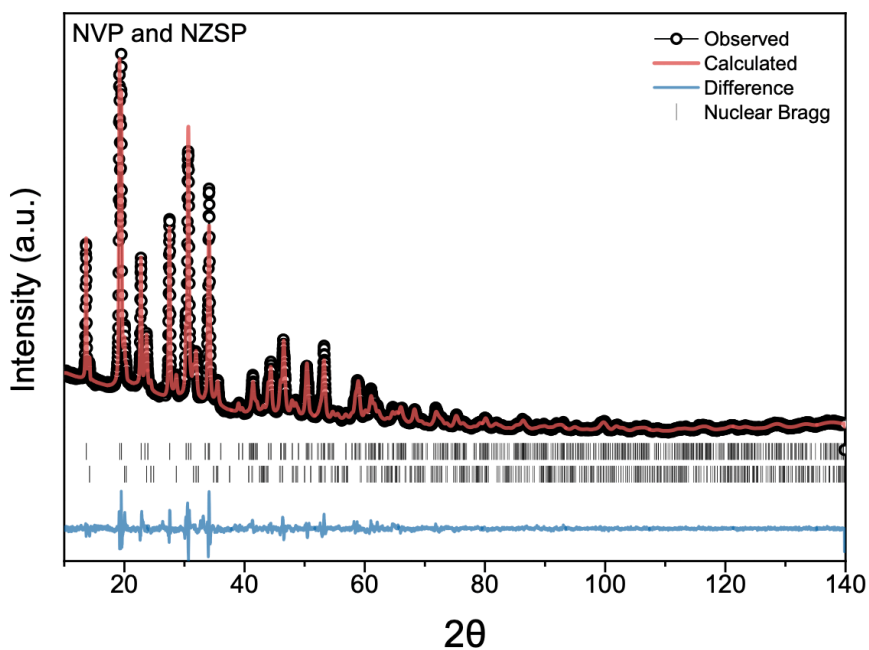


Figure 4.3 Refined X-ray diffraction (XRD) pattern of NVP-NZSP co-sintered powder.

In order to check the compatibility of the two materials, NZSP powder and NVP precursor solution was mixed. After a heat treatment of 6 h at 740 °C in Ar-H₂, no

additional phases could be detected by XRD, as shown in **Figure 4.3**. The lattice parameters of NVP ($a = 8.7321(5) \text{ \AA}$, $c = 21.844(2) \text{ \AA}$) and NZSP ($a = 9.0981(5) \text{ \AA}$, $c = 22.786(2) \text{ \AA}$) are obtained from the refinement of the X-ray diffractograms, and the atomic site occupation is shown in **Table 4.1**. For both lattice parameters, the difference between NVP and NZSP is only 4%. The refinement was performed by colleagues at the School of Advanced Materials, Peking University Shenzhen Graduate School.

Table 4.1. Crystallographic data of NVP and NZSP after infiltration and heat treatment.

(a) NZSP

Atom	Wyckoff site	x/a	y/b	z/c	Occupancy
Na1	6b	0	0	0	0.720
Na2	18e	0.63387	0	0.25	0.696
V	12c	0	0	0.14813	1
P	18e	0.29089	0	0.25	1
O1	6f	0.17803	0.03473	0.19291	1
O2	6f	0.19425	0.16862	0.08910	1

(b) NVP

Atom	Wyckoff site	x/a	y/b	z/c	Occupancy
Na1	6b	0	0	0	0.411
Na2	18e	0.63725	0	0.25	0.761
Na3	36f	1.01390	0.85387	1.01356	0.0926
Zr	12c	0	0	0.14804	1
Si	18e	0.29088	0	0.25	0.91
P	18e	0.29088	0	0.25	0.09
O1	36f	0.17754	0.03625	0.19217	1
O2	36f	0.19521	0.16728	0.08957	1

4.2 Fabrication

A detailed introduction to the fabrication steps of Na-ASSBs by chemical infiltration can be found in **Section 2.2.2**. This part will discuss several steps in the process with details.

4.2.1 Fabrication of multi-layered NZSP pellets

The porous NZSP layer was made by mixing rice starch (RS) (10 wt. %) into NZSP precursor, which burnt during the sintering in air and left behind well distributed pores. The following figures (**Figure 4.5**) are laser optical microscopy images of the surface and the cross-sections. On the surface, the lower regions (green to blue colour) indicates the open pores. On the cross-section, the difference in porosity is obvious between different layers, and the majority of the pores have a diameter below 5 μm .

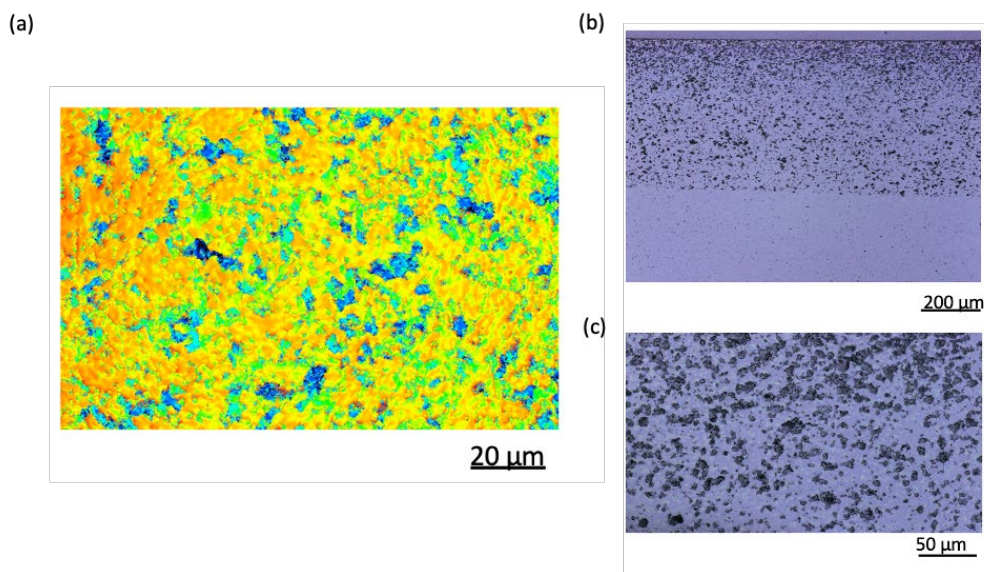


Figure 4.5 Optical microscopy images of multi-layered NZSP samples: (a) image taken on the porous surface, with colours indicating the relative heights of the surface (red: highest to blue: lowest) (b-c) images with different magnification taken on cross-sections

With higher concentrations of starch, however, pellets become unstable, with macroscopic defects in the porous layers. Also, the cross-section images (**Figure 4.6**) shows that the layer with 20 wt.% of RS were completely damaged during sintering and only a few large pores left; the 30% layer almost disappeared, leaving only a few small pores in the bordering region with the dense part.

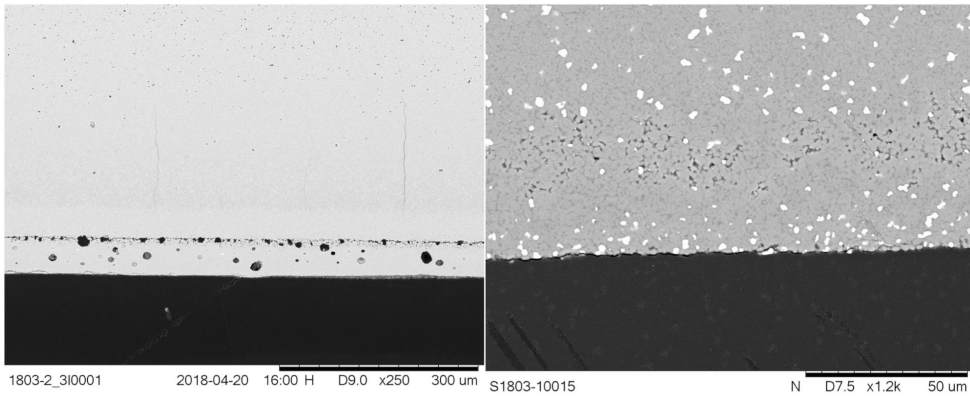


Figure 4.6 SEM images of multi-layered NZSP pellets: left, 20 wt. % of rice starch in porous layer; right, 30 wt. % (particles with high contrast are ZrO₂)

In order to further investigate the mechanism of the abnormal densification, an optical inspection system “TOMMIplus” was used to record the morphological changes during sintering of the porous layer. Three pellets were prepared from different kinds of powder: pure NZSP, NZSP with 10 wt.% RS, and NZSP with 20 wt.% RS. Due to the photo resolution of the camera, only single-layered samples were prepared to make the differences more obvious and visible. In order to avoid contamination of the system, the pellets were firstly heated to 500°C with a rate of 6 K/min, and transferred into “TOMMIplus” after cooling down. Then the samples were sintered to 1280°C with a rate of 6 K/min, and the key photos in the record are summarized in **Figure 4.7**.

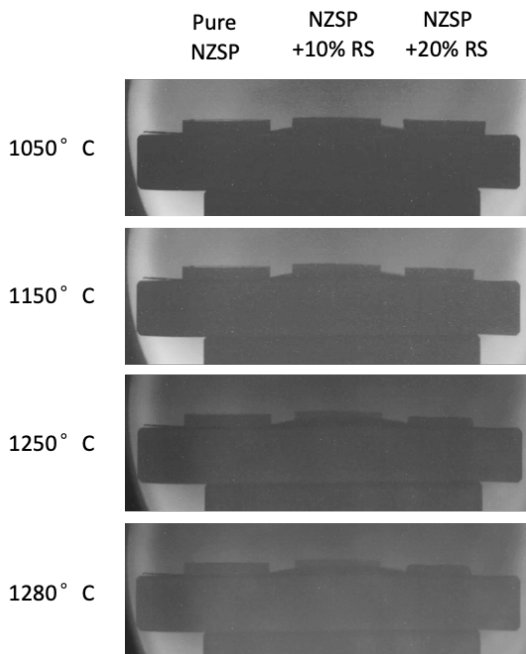


Figure 4.7 Photos of pellets with different amount of starch during sintering

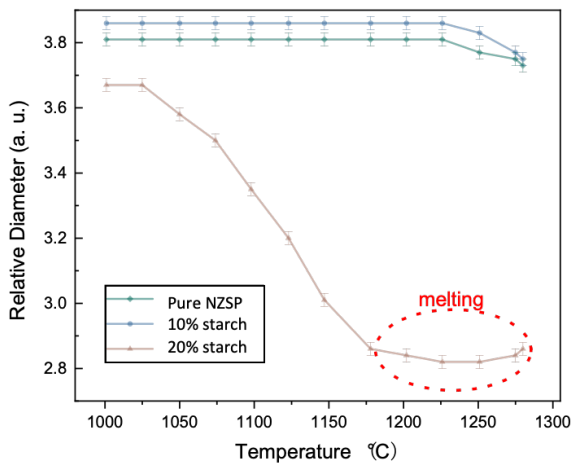


Figure 4.8 Relative diameter change of pellets with different amount of starch during sintering

As shown in **Figure 4.7**, the sintering behaviours of pure NZSP and NZSP - 10% RS are similar, while the NZSP - 20% RS shrank much more starting from 1150°C, and finally melted at 1280°C. The results indicated that the melting point of NZSP was reduced with higher amounts of starch. This phenomena is not common in previous reports on using RS as a pore former [156], thus further study is needed to determine the mechanism. To sinter the multi-layered sample with 20% RS, 1150°C is not enough to fully densify the electrolyte, but the difference of shrinkage between layers is already massive to destabilize the pellet, as shown in **Figure 4.8**. Further research should be done to optimize the sintering process of the multi-layered NZSP to balance the stability of porous layer and density of the dense layer. Possible solutions include change of the pore former or pre-sintering of NZSP in the mixture. For the first cells, the pellets with 10 wt. % starch will be used.

4.2.2 Preparation of NVP precursor solution

The first recipe of precursor solution was based NaH_2PO_4 and NH_4VO_3 in nitric acid. The concentration of active materials in the solution was limited by the solubility of NH_4VO_3 in aqueous solution. The highest solubility was achieved by solving NH_4VO_3 in 25% nitric acid, which was only about 0.3 mol/L. Such solution is also not stable with vanadium and phosphorus precipitating in the form of VOPO_4 . This will lead to a higher relative concentration of sodium in the solution. Visible precipitation appeared after several hours of standing, while the ratio of different elements could still change in a micro-pore even in a very short time. To solve the problems above, a new method of solution preparation was necessary.

V_2O_5 has never been reported to be soluble in any solutions, but can react with NaOH solution with high concentration, producing soluble VO_4^- ions. NH_4VO_3 is soluble in both di-ethanolamine and ethanolamine (EA), which are miscible with water. A series of experiments were carried out on the ratio of solute and solvent. To the maximum, 1.5g NH_4VO_3 was soluble in 10g of solution, which was about 1.3 mol/L and much higher than that without EA. The solution was also proved to be long-time stable. It is worth noting that a large amount of heat was released during

the mixing, raising the temperature of the solution from room temperature to about 60°C.

The use of EA significantly increased the miscibility of NH_4VO_3 and H_2O molecules, increased the solubility of NH_4VO_3 in aqueous solution, and prevented the precipitation of vanadium-phosphorus compounds. Also, ethanolamine was reduced to elemental carbon in Ar/H_2 during the heat-treatment to form NVP, which can act as current collector in the electrode. Citric acid can be added into the solution, to increase the amount of carbon after heat-treatment. A higher amount of carbon is necessary for batteries with higher loading, and will be discussed in details later.

4.2.3 Infiltration of NVP precursor solution

Infiltration was made by dropping the precursor solution on the surface of porous NZSP. For infiltration, wettability is an important property of the liquid used and will strongly influences the amount of liquid in the pores and thus the effectiveness of infiltration. In this thesis, the wettability of the solution and NZSP was studied by measuring the contact angles of the solution on NZSP pellets. The solution was dropped on both polished and unpolished surfaces of sintered NZSP pellets.

Photos taken are shown in **Figure 4.9**. Since the solution had a very low viscosity, the shape of the drops changed slowly during the test. After 5 minutes, the contact angle with unpolished surface changed from 36° to 28° and that with polished surface from 13° to 8°. The results for polished surface were not very accurate since the surface became curved during manual polishing, and the real wetting angle should be even smaller.

The solution was proven to have a very high wettability on NZSP, which will help the solution to infiltrate NZSP pores via capillary forces. The infiltration happens automatically after the contact of solution with the porous layer.

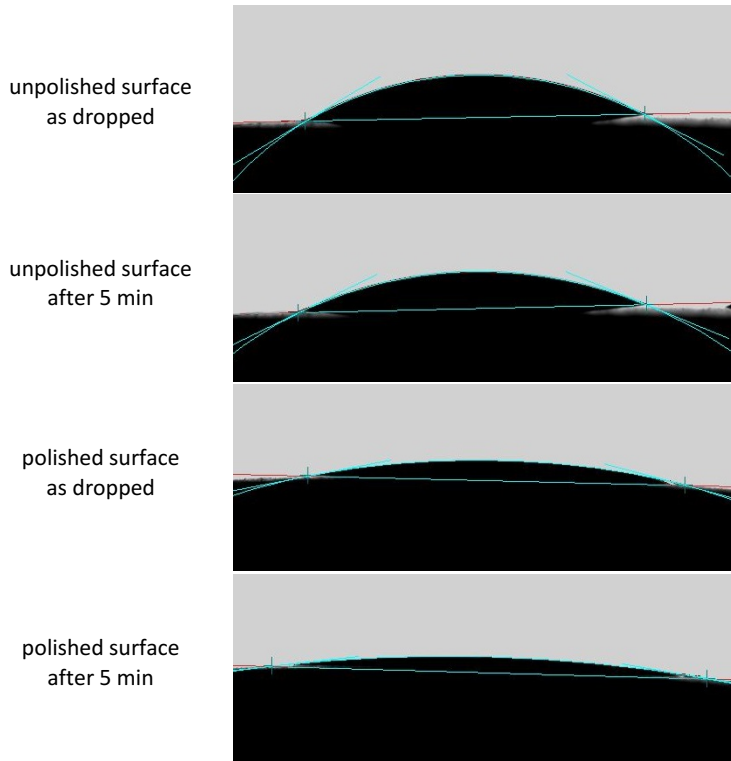


Figure 4.9 Photos of the solution dropped on different NZSP surfaces

4.3 Performance

4.3.1 Long-term cycling performance

Charge/discharge cycling of the NVP|NZSP|Na batteries with infiltrated positive electrode was performed with various current densities at 25 °C.

Figure 4.10a shows the charge/discharge behaviour during a 100-cycle test, illustrating the voltage as a function of the charged/discharged capacity of the battery. Starting from the 3rd cycle, the battery was operated between 2.8 V and 3.8 V with a C-rate of 0.1 (current density of 35.2 $\mu\text{A cm}^{-2}$). Each plot exhibits a flat plateau at approximately 3.4 V, the typical potential of the V(III) \leftrightarrow V(IV) redox reaction [157], representing a stable electrode reaction in the infiltrated positive electrode. Each plot exhibits a flat plateau at approximately 3.4 V, the typical potential of the V(III) \leftrightarrow V(IV) redox reaction [157], representing a stable electrode reaction in the infiltrated positive electrode. Charge and discharge plateaus of the same cycle are very similar, determining the small internal resistance of the battery. Most importantly, the capacity fades gradually and very slowly, demonstrating the stability and the superior cycle ability of the battery.

Figure 4.10b shows that the battery has specific discharge capacities (i.e., capacity divided by the weight of the active electrode material) between 97.4 for the 3rd cycle and 88.5 mAh g⁻¹ for the 100th cycle (the theoretical capacity being approximately 118 mAh g⁻¹) [85]. The Coulombic efficiency is 98.3 % for the 3rd cycle, while for cycles 5-14 it is above than 99 %, and for cycles 15-100 it is higher than 99.5 %. The overall capacity degradation, calculated from the third cycle, was only 9.1 % after 100 cycles.

Results obtained from a battery operating with a higher C-rate (0.6 C, 127.7 $\mu\text{A cm}^{-2}$) are shown in **Figure 4.10c** and **4.10d**. Starting from the first stable cycle (3rd), the capacity faded from 106.0 to 96.5 mAh g⁻¹ (100th cycle), that gives a capacity retention of 90.57 %. The Coulombic efficiency was 98.9 % for the 3rd cycle, while for cycles 4-26 it was above 99 %, and for cycles 27-100 it was above 99.9 %. The specific capacity of this battery was slightly higher than the one tested with 0.1 C (**Figure**

4.10a and 4.10b) because of the periods at constant voltage when the battery was still charged/discharged.

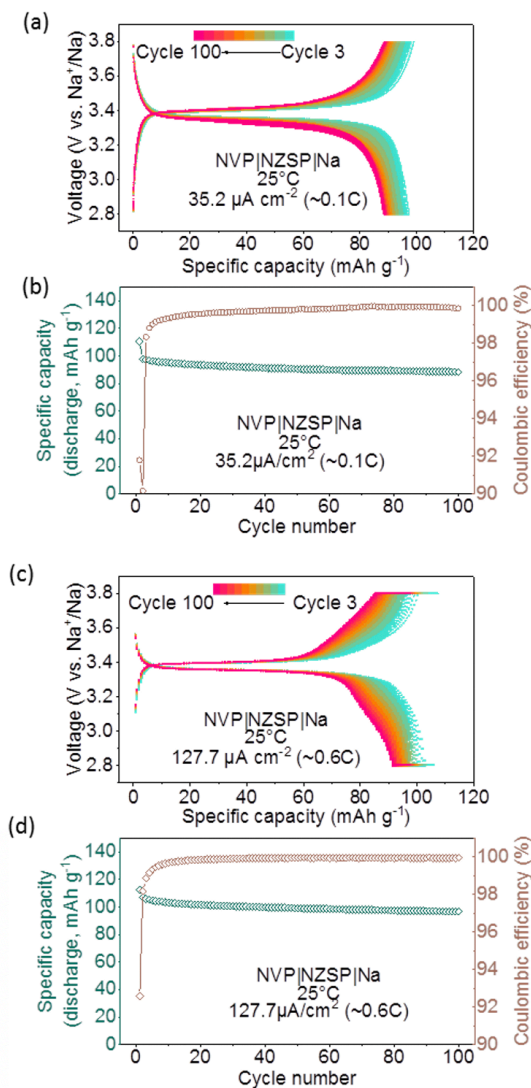


Figure 4.10 Cycling performances of NVP-NZSP-Na cells

(a-b) a cell operating with a current density of $35.2 \mu\text{A cm}^{-2}$: (a) charge and discharge curves for stable cycles; (b) discharge capacities and Coulombic efficiencies
 (c-d) a cell operating with a current density of $127.7 \mu\text{A cm}^{-2}$: (c) charge and discharge curves for stable cycles; (d) discharge capacities and Coulombic efficiencies

The first two cycles of each test had initial capacity losses due to presently non-identified side reactions, and were used to adjust the testing parameters (details given in **Figure 4.11a**).

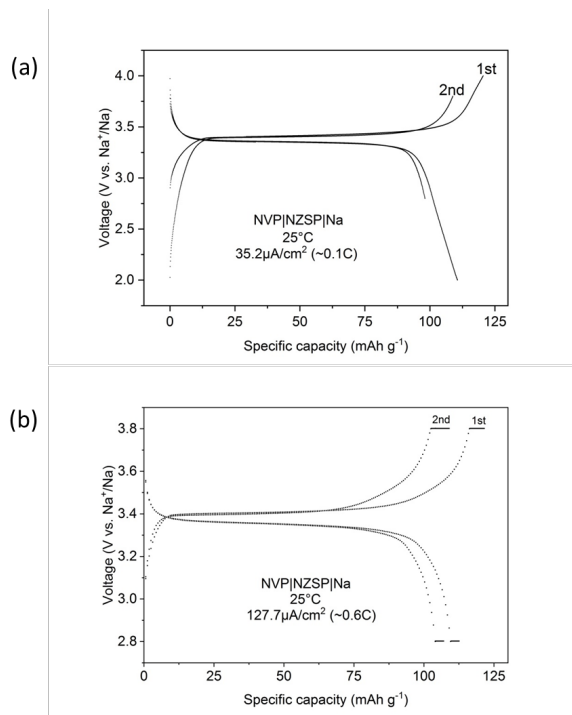


Figure 4.11 Charge-discharge curves of the 1st and 2nd cycle of the batteries: (a) Battery shown in **Figure 4.9 (a-b)**; (b) Battery shown in **Figure 4.9 (c-d)**

4.3.2 C-rate tests

Charging and discharging behaviour was also tested with different current densities (C-rates) on a third battery.

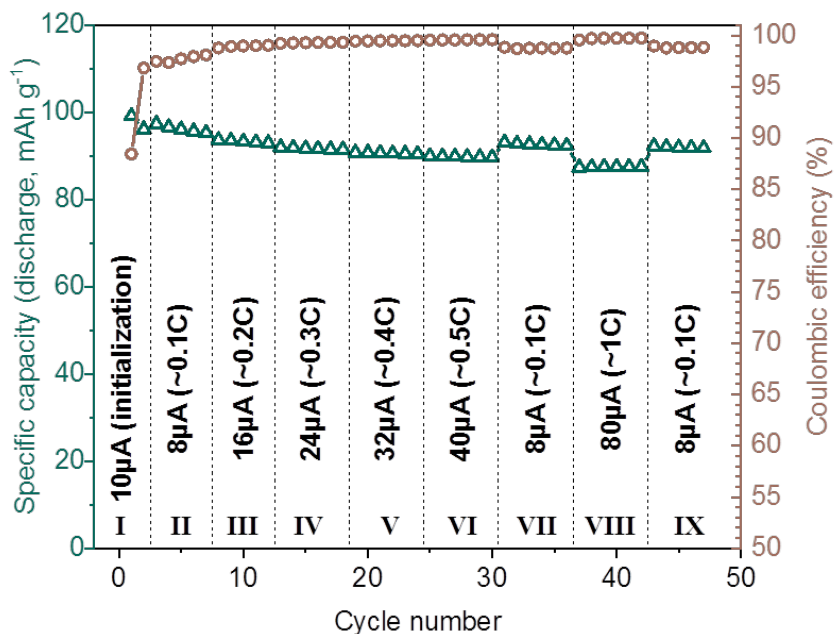


Figure 4.12 Performance of a cell operating with different current densities: corresponding discharge capacity and Coulombic efficiency for each cycle.

Figure 4.12 summarizes the discharge capacities and Coulombic efficiencies for each cycle. With higher current density, the capacity became smaller due to the ohmic polarization caused by internal resistance of the battery. Cycles with a fixed C-rate showed very small degradation, similar to the performance shown in **Figure 4.10b** and **d**. After cycles performed with high current densities (in stage **VI** and **VIII** in **Figure 4.11**), the capacity in stage **VII** and **IX** restored to a level similar to that in stage **II**. The capacity of the final cycle in stage **IX** corresponds to 94.3 % of that of the first cycle in stage **II**. The decrease in capacity with increasing current densities resulted from larger polarization rather than the deterioration of the battery.

The relationship between current and polarization was investigated for this battery, and gives a better indication of the internal resistance than the impedance, because of the complex structure of the electrode. The polarization of each cycle was measured by calculating the potential difference between the charge and discharge

plateaus at a fixed capacity of 30 μAh , which was a shared value within the plateau range with various C-rates. The potential differences of cycles in stage II were about 22 mV, and comparable to sodium batteries using NVP and liquid electrolytes[77]. Further calculation is made on the relation between potential difference and current density, as shown in **Figure 4.13**.

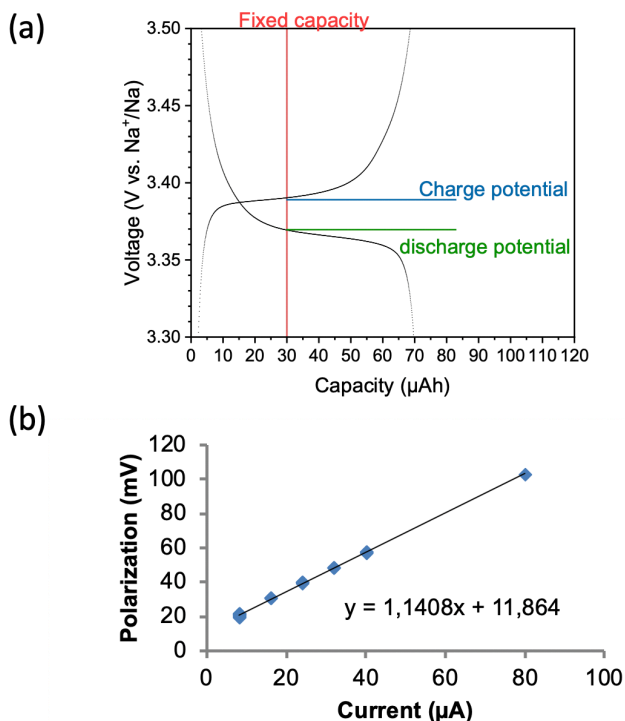


Figure 4.13 Calculation of internal resistance of the battery in **Figure 4.11**: (a) an example (Cycle 3) of how to determine the potential difference; (b) relation of voltage differences ($\Delta V = V_{charge} - V_{discharge}$) and current used, with the linear regression of the data.

In **Figure 4.13**, the relation between current and polarization of this battery is shown. Cycle 3 (with current of 8 μA) is shown as an example in **Figure 4.13a**. The dependence of polarization (mV) on current (μA) showed good linear relation with a slope of 1.1408, indicating that the internal resistance of the battery was about 570 Ω

($396 \Omega \text{ cm}^2$). Hence, the internal resistance was much smaller than typical ASSBs [34], and can be even smaller if a thinner electrolyte separator is applied.

For cycles with $80 \mu\text{A}$ current, only Cycle 38 was included in **Figure 4.13b**. Cycles 39–43 (2nd–6th cycle with $80 \mu\text{A}$) showed slightly larger polarization and is not included. The abnormal polarization probably resulted from a limited electronic conductivity, since the capacities were not influenced and the cell returned to normal cycling behaviour after applying again lower current densities.

4.3.3 Batteries with higher loading

Na-ASSB cells with higher loading of NVP were also fabricated, by making thicker porous NZSP layer ($\sim 0.5 \text{ mm}$) and infiltrating NVP for more times (up to 6). Data in this section was published [36] in *Journal of Power Sources*.

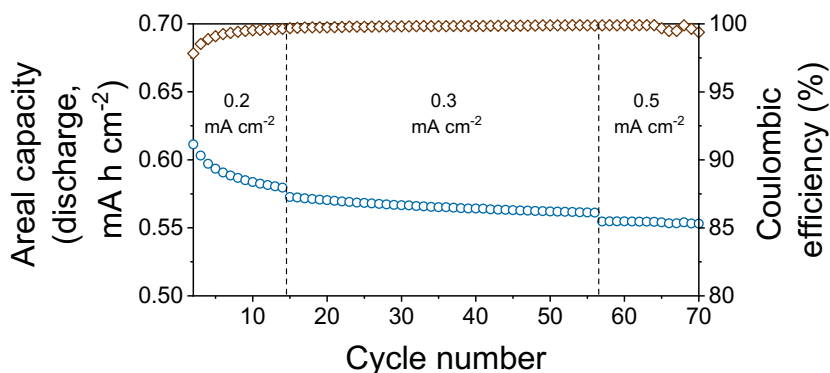


Figure 4.14 Discharge capacity and Coulombic efficiency at different current density of a typical high-loading Na-ASSB cell in dependence of the cycle numbers

A typical cycling performance of the high-loading cells is shown in **Figure 4.14**, with a mass loading of active cathode materials (NVP) as 6.2 mg cm^{-2} . After 3 cycles of stabilization, the cell has a discharge areal capacity of $0.60 \text{ mA h cm}^{-2}$ with Coulombic efficiency of 98.5% (which gradually increases to 99.5% at the 10th cycle). After operating at current densities of 0.2, 0.3 and 0.5 mA cm^{-2} for totally 70 cycles at $25 \text{ }^\circ\text{C}$, the areal capacity still remains $0.55 \text{ mA h cm}^{-2}$ with Coulombic efficiency of

99.5%, indicating the stability of the cell. This is already among the ASSB cells with highest loading in both Li and Na systems.

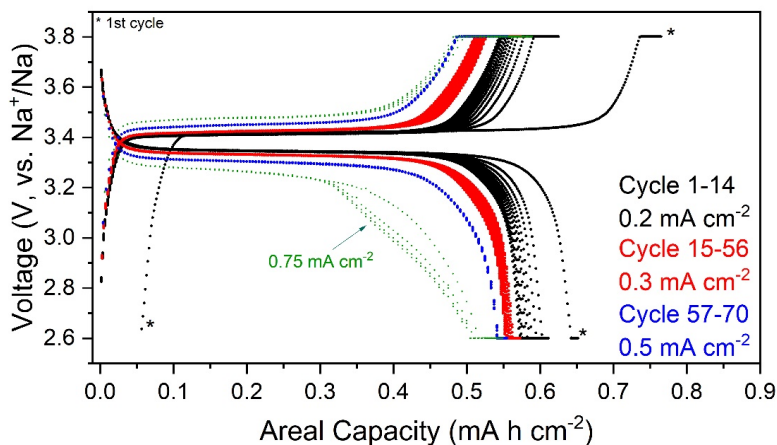


Figure 4.15 The charge-discharge curves of cell described in **Figure 4.14**

The results of charge/discharge cycling of the cell presented in **Figure 4.14** is shown in **Figure 4.15**. The cell was cycled with various current densities at 25 °C. The first two cycles had initial capacity losses due to presently non-identified side reactions, and were used to adjust the testing parameters. Starting from the 3rd cycle, the battery was operated between 2.6 V and 3.8 V with current density ranging from 0.2 mA cm⁻² to 0.75 mA cm⁻², and the cell was held at constant voltages for 30 minutes after each charge/discharge step. In general, the capacity fades gradually and very slowly, demonstrating the stability and the superior cycle ability of the battery. Especially at 0.5 mA cm⁻², the cell is still stable. However, with higher current density (0.75 mA cm⁻²), the polarization of the cell can be clearly seen in the discharge processes, indicating that the electrode reaction in the positive electrode

does not permit higher current densities. Further improvements of the positive electrode part of the cells are necessary, as discussed in **Section 4.6**.

4.4 Characterization

4.4.1 Microscopic methods

The microstructure of a typical NVP-NZSP electrode given by SEM in **Figure 4.16** and **Figure 4.17**. The porosity of the electrolyte scaffold is found to vary between 20 % and 25 %. The vanadium distribution, measured by EDS, was used to probe the NVP distribution, as shown in **Figure 4.16b**. The continuity of the NZSP is clearly visible in **Figure 4.16a**. The continuity and openness of most of the pores are demonstrated by the fact that the liquid precursors can only enter open pores, but vanadium is present in all parts of the porous layer. As shown with higher magnifications in **Figure 4.17**, The NVP particles (dark contrast) are homogeneously distributed on the pore walls of the NZSP (bright contrast), forming thin and continuous layers (approximately 50-200 nm thick) on the electrolyte support.

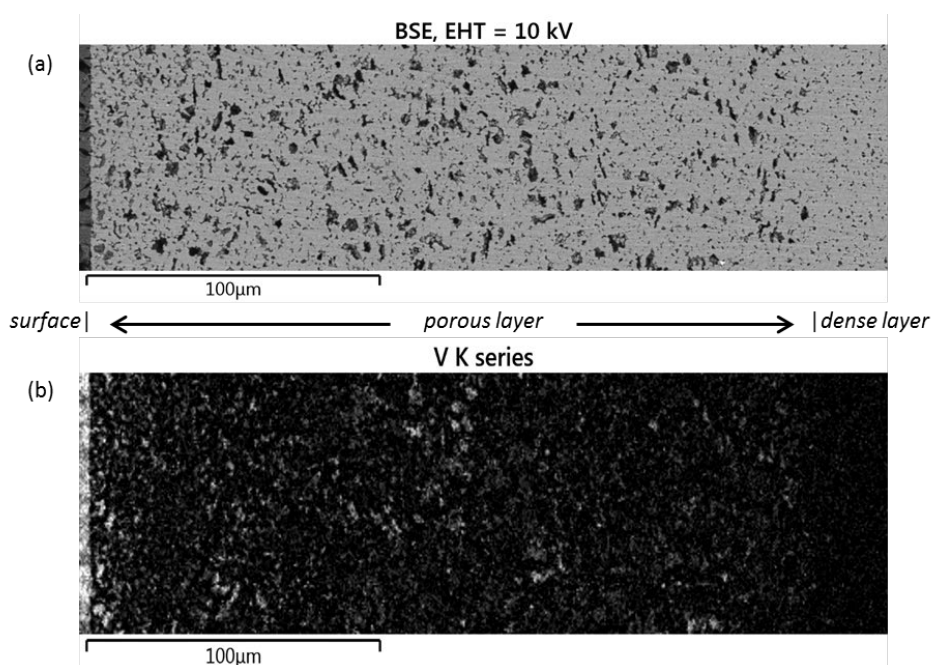


Figure 4.16 SEM images of an infiltrated NVP-NZSP pellet with elemental mapping by EDS: (a) Backscattered electrons image of the porous part with the surface on the left side (b) EDS mapping of vanadium in the same area as (a).

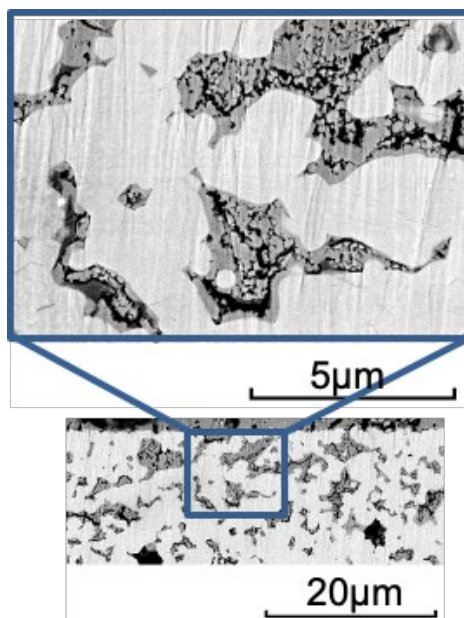


Figure 4.17 SEM images with higher magnification of a cross-sectional NVP (dark contrast)-infiltrated NZSP (bright contrast) pellet.

In order to elucidate the NVP-NZSP interface, which is essential to the performance of ASSBs, HAADF-STEM was used to investigate the positive electrode before and after cycling. **Figure 4.18a** shows the morphology of the as-prepared electrolyte-electrode composite structure, where the image contrast clearly identifies the NZSP (bright contrast) and the NVP (dark contrast) phase in terms of the Z-contrast imaging principle of HAADF-STEM[158]. After infiltration and heat treatment, a NVP layer forms and is well attached to pore walls of the NZSP framework. The interface providing substantial stability enhancement is confirmed by examination of the interface after the 100-cycle electrochemical tests at 0.6 C (**Figure 4.18b**), as described in **Section 4.3**. After the cycling of the battery, the contact between the NZSP framework and NVP layer is maintained, without any interfacial cracks or cleavage of the phases observed.

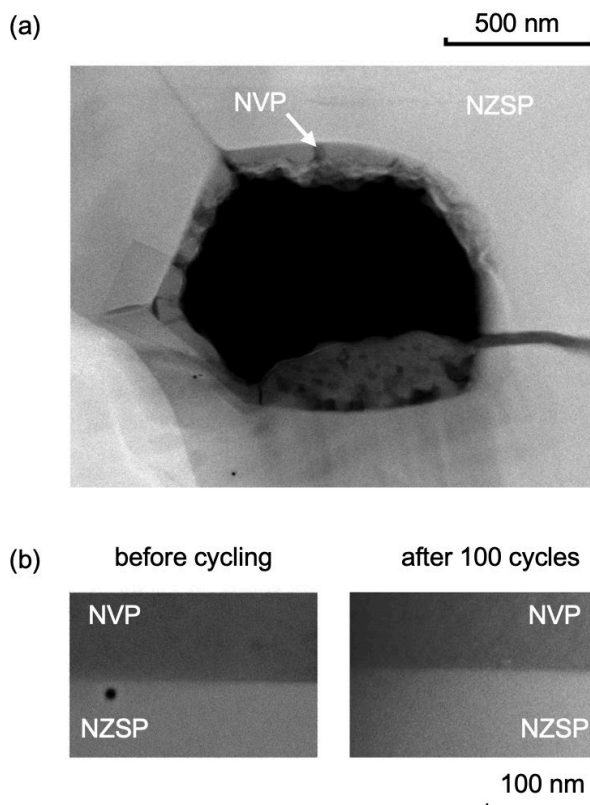


Figure 4.18 Microscopic morphology and compositional characterization near the NVP-NZSP interface:

- (a) HAADF-STEM image of as-prepared NVP-NZSP composite collected from a typical micrometer-scale pore.
- (b) Mesoscale comparison of the interface structure before (left) and after 100 cycles of charging and discharging (right) test at a current of 0.6 C. A black spot in the image was caused by electron-beam irradiation.

An elemental mapping analysis by EDS reveals the distribution of ‘fingerprinting’ V, Si, and Zr at a NVP/NZSP interface, as shown in **Figure 4.19a**. V clearly diffuses from NVP into NZSP, whereas Si and Zr are better retained on the NZSP side. Since the NVP and NZSP phases have the same crystal structure and similar lattice parameters, the substitution of atoms from one phase to another is unlikely to modify the structure of the other phase [159]. In addition, the diffusion is likely to

further minimize lattice parameter mismatch and facilitate a good mechanical contact between these two phases.

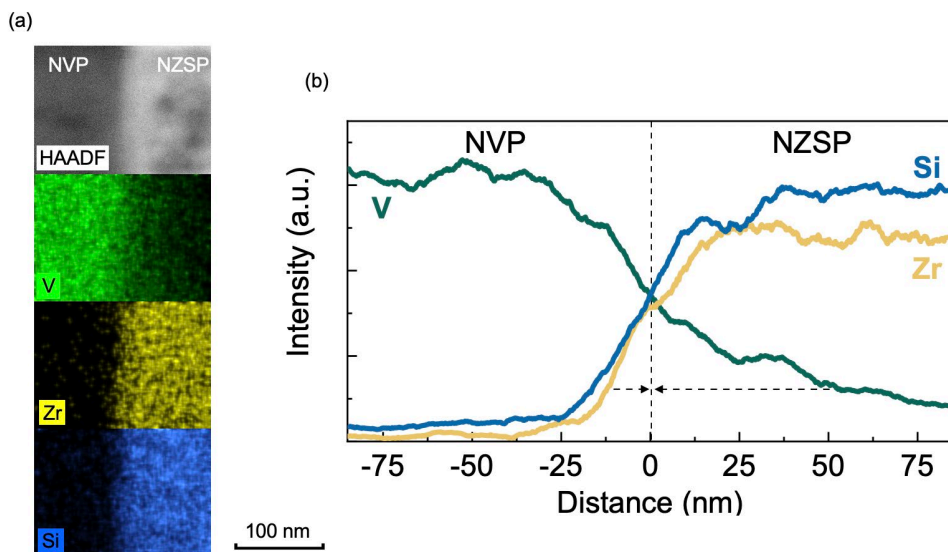


Figure 4.19 Compositional characterization near the NVP-NZSP interface:

- (a) HAADF-STEM image of the interface structure, along with 'fingerprinting' elemental maps of V for NVP and Zr, Si for NZSP.
 (b) Line profiles of elemental distribution for V, Zr and Si corresponding to the entire region shown in (a). Arrows indicate the deeper penetration length of V into NZSP, compared with those of Zr and Si into NVP.

The elemental interdiffusion behaviour near the interface is further illustrated by line profiles of the three elements (**Figure 4.19b**). The penetration length of V into the NZSP, compared with those of Si and Zr into NVP, clearly evidences the cation diffusion at the interface, which is attributed to the *in situ* synthesis of NVP on the NZSP. Clearly, the chemical infiltration method provides a promising strategy to guarantee intimate contacts in positive electrodes. The EDS mapping shows a carbon enrichment at the surface of the NVP phase (**Figure 4.20**), resulting from the carbonization of ethanolamine. Carbon is favourable for providing electronic conduction pathways, and is commonly added to NVP electrodes in previous

reports [41,76-78,85,140]. Averaging the analytical EDS results from different regions resulted in an atomic ratio V:C \approx 8:1.

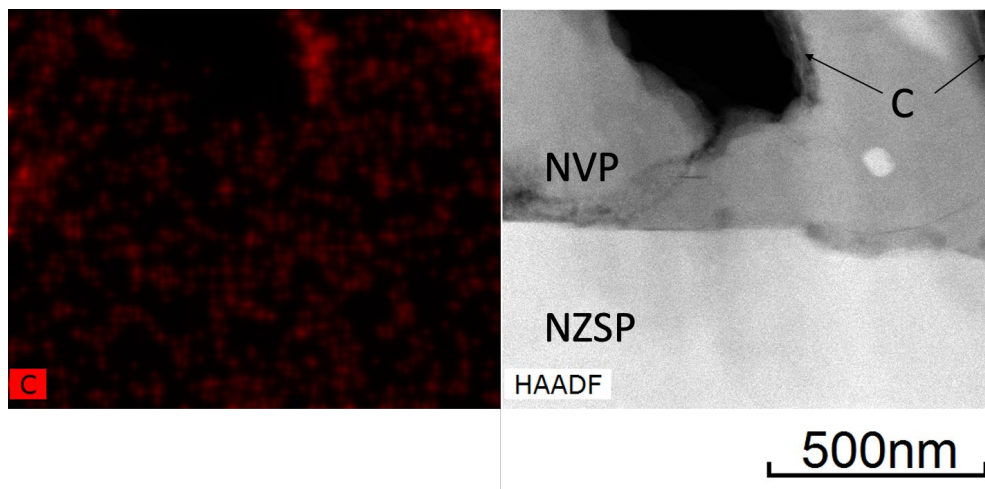
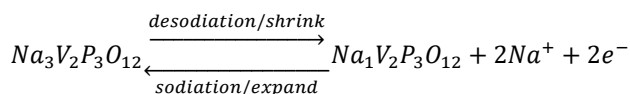


Figure 4.20 EDS mapping of carbon with the HAADF image of the same area

4.4.2 *in situ* XRD

During the discharge and charge processes of batteries, the sodiation and desodiation of NVP occurs with the following phase transformation:



In order to have a better understanding on the transformation in Na-ASSBs and its influence on the volume change of NVP, *in situ* XRD patterns were obtained from the positive electrode surface during the cycling of a battery, when it was charged/discharged between 2.8 V and 3.8 V. As shown in **Figure 4.21**, the diffraction angle from $2\theta = 31^\circ$ to 33.5° was chosen to record one of the strongest reflections of NVP. Before cycling, NVP in $R\bar{3}c$ symmetry is detected. During cycling, the phase transition of NVP (eq. 1) is observed. This transformation is completed, as indicated by the shift of the (116) diffraction peak, and is similar to the behaviour measured on batteries containing liquid electrolyte by Jian et al. [77]. Since the signal

was recorded from the surface of the electrode, which is the furthest section away from the electrolyte separator, the results suggest that all of the NVP inside the electrode participated in the sodiation and desodiation (within the detection limitation of XRD).

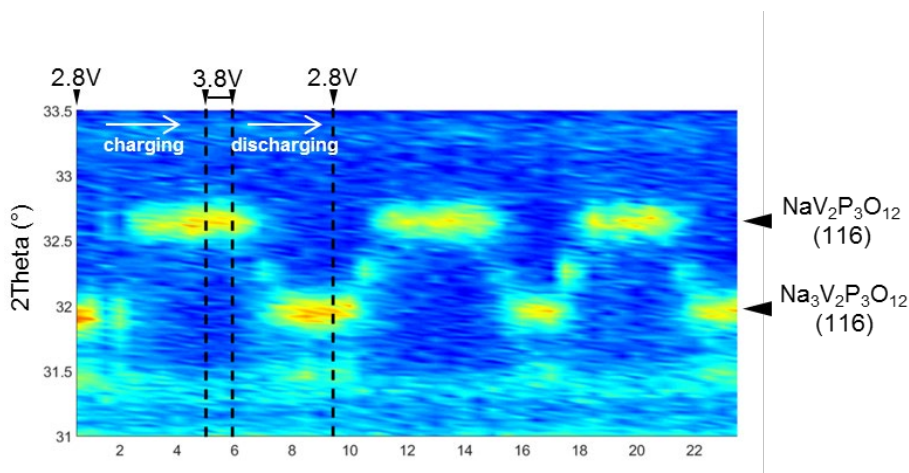


Figure 4.21 Structural change of NVP during cycling of the cell. In situ XRD patterns (2θ from 31 to 33.5°) of a cycled NVP-NZSP-Na battery, measured on the outer surface of the positive electrode.

The lattice parameters of $\text{NaV}_2\text{P}_3\text{O}_{12}$ after charging are $a = 8.409(1) \text{ \AA}$ and $c = 21.655(3) \text{ \AA}$ (Section 4.1), indicating that the volume change accompanying the phase transformation is about 8 % as a result of the extraction/insertion of Na ions, in agreement with results from liquid-based batteries [77]. In the case of co-sintered mixed electrodes, such a volume change is geometrically constrained and introduces internal stress in the electrode microstructure. High levels of mechanical stress can damage the interface between electrode and electrolyte particles, or even trigger crack growth within the particles [34]. For the ASSBs produced by chemical infiltration, most NVP particles are not closely packed, with only one plane shared with NZSP as the interface, as shown by electron microscopy in Figure 4.18. The

dimensional changes of NVP can therefore be accommodated without creating a significant internal stress. Residual free volume in the infiltrated electrode is occupied during discharging or created during charging in operation of the batteries.

4.5 Discussion: Infiltrated Na-ASSBs compared with other ASSBs

As summarized in **Table 1.1**, before the present work, the only reported ceramic based Na-ASSBs [51,52] that operated stably at RT (~25% capacity fading after 100 cycles) had been prepared by pulsed laser deposition, an advanced thin film method limited in scalability in the foreseeable future. Batteries prepared and characterized in the present work showed overall degradations of below 10 % after 100 cycles at 25 °C. Previous bulk type Na-ASSBs using similar materials [41,76,140] showed more pronounced fading (15-35 %) during less than 40 cycles, and systematically benefited from higher operating temperatures (80 °C or even 200 °C).

The degradation level observed here is similar to those of batteries fabricated using soft solid electrolyte materials, such as complex Na-*closo*-borates[24], sulphides[22] and polymer[44]. These soft materials typically offer, due to their deformability, better contacts with the electrode materials and better tolerance to volume changes than oxides or phosphates, but lack mechanical, chemical, thermal and electrochemical stability[1]. In contrast, the achievements presented here largely benefit from the microstructure design, bringing together two stiff ceramic phases.

The loading of active positive electrode material (1.7 mg cm⁻² and 3 mg cm⁻²) is only below that of the previously reported ASSB operated at 200 °C, prepared by co-sintering in a pressure-assisted spark plasma sintering device [140]. In every aspect, Na-ASSBs in the present work have comparable properties to the best Li-ASSBs of the same type[49]. The degradation in discharge capacity of one ASSB (**Figure 4.10c**) is compiled in **Figure 4.22**, and compared with other ASSBs manufactured with similar materials[41], as well as with a Na-ion battery containing a liquid electrolyte[77] and a Li-ASSB[49]. The performance loss of the present battery with an infiltrated positive electrode is much better than that of previous Na-ASSBs, and similar to that of batteries with a liquid electrolyte. Compared to bulk-type Li-ASSBs, batteries in this work have similar degradation but more stable performance with less capacity fluctuating.

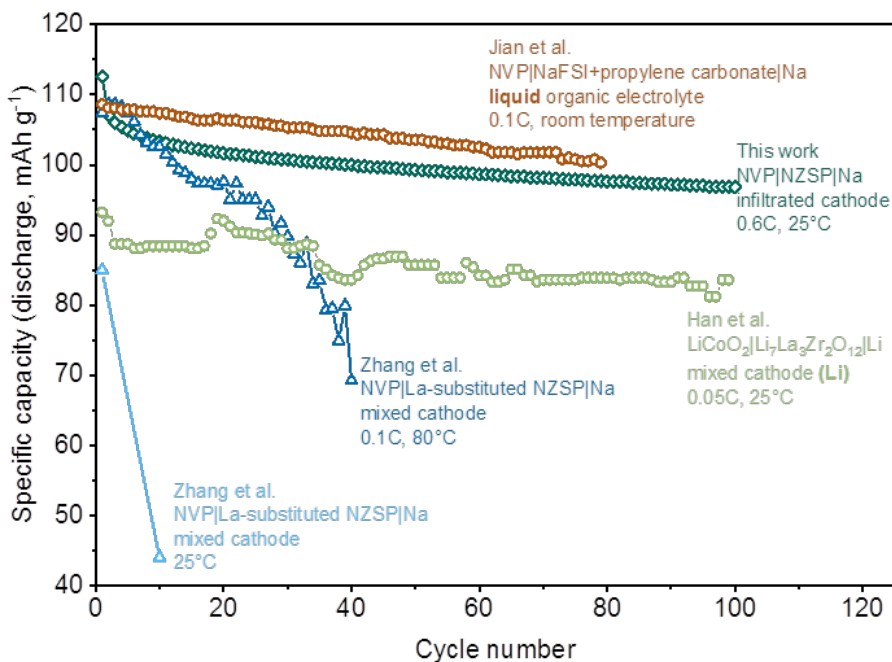


Figure 4.22 Discharge capacity degradation of different ASSBs and a sodium-ion battery with liquid electrolyte. Data from this work are compared with those taken from figures in previous publications (Zhang et al. [41], Jian et al. [77], and Han et al. [49])

Compared with similar concepts of infiltration reported previously [43,58,59,65], the chemical infiltration in the present thesis provides an optimized interface between the electrolyte and electrode materials, which is a critical factor to a stable battery performance. The interface formed during the *in situ* synthesis, well-connected and highly tolerant to the volume change of the electrode material, provides better stability than direct transferring of electrode materials into porosity by suspension [43]. It is also worth noting that the *in situ* synthesis of electrode material is not only about infiltrating precursor solution, but requires the compatibility of the electrode and electrolyte materials, due to the possible elemental inter-diffusion. In the present report, two NASICON phases are used, which proved to tolerate to the inter-diffusion. Incompatible materials, such as LiCoO_2 and

$\text{Li}_{6.75}\text{La}_3\text{Zr}_{1.75}\text{Ta}_{0.25}\text{O}_{12}$ reported previously [65], cannot benefit from a desired interface. The battery performance can be even worse than batteries with mixed and co-sintered electrodes, due to the reaction between materials during heat-treatment. By considering these key factors, we have found the proper process to apply chemical infiltration on the fabrication of ASSBs for the first time and solve the contact and strain problems.

4.6 Outlook

Application of chemical infiltration on other systems

In this thesis, chemical infiltration significantly contributes to the progress towards practical application of Na-ASSBs. In addition, most ASSBs need a permanent mechanical pressure during operation, whereas the infiltrated Na-ASSBs do not require any external load [21]. This might be an important asset on the system level. The present approach is also flexible and can be applied to various scaffolds and infiltrated material combinations.

Chemical infiltration requires lower temperatures for the combination of electrolyte and electrode materials than traditional co-sintering, and enables more choices of materials to be incorporated into ASSBs. The proven tolerance of the prepared electrode, with a volume change of 8% of the active materials in this work, offers the opportunity to use other electrode materials with similar or smaller volume change, e. g. LiFePO_4 (c.a. 5 %), with the possibility of an even better performance.[160]

Optimization towards higher operating C-rates

Cells in this thesis were able to operate at 0.5 C and those with small loadings at 1C. These high C-rate is a breakthrough for ASSBs, achieved by low internal resistance of the cells. However, 1C is still not enough for practical application, let alone large cells showed a fluctuating performance at such a rate (**Figure 4.14**). In contrast, NVP in batteries with liquid batteries were reported able to operate at much higher C-rates (up to 10C) [115].

As discussed in **Section 4.3.2**, Na-ASSB cells prepared by chemical infiltration have similar internal resistance as cells with liquid electrolyte. Thus, there must exist some other factors that prevent the ASSB cell from fast charging/discharging. **Figure 4.23** is a typical charge/discharge curve of NVP|NZSP|Na cells, with the discharge curve flipped along the x-axis. After the flipping, the x-axis can be represented by the Na^+ amount in NVP. It is clear that the deviation of the discharge curve cannot be explained by ohmic polarization, since internal resistance should increase with

less Na^+ in NVP, while in the discharge curve it slopes in the other direction. The deviation of potential, then, can only be explained by the concentration polarization inside the less conductive NVP phase.

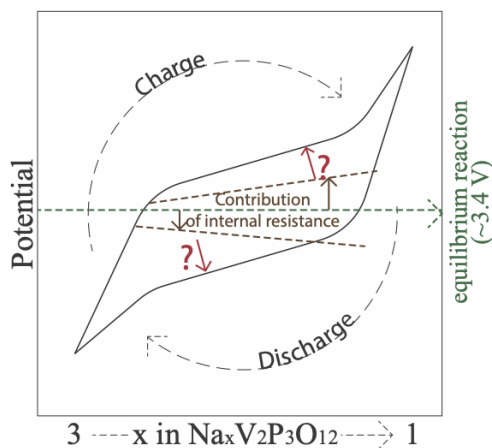


Figure 4.23 A typical shape of charge/discharge curve of a NVP-NZSP-Na ASSB cell, with Na concentration as the x-axis. The discharge curve is flipped horizontally from that plotted against capacity.

This assumption can be further confirmed by the current dependency of the curves, as shown in **Figure 4.24**. The deviation of the discharge curve from the equilibrium state, though has an opposite direction from the current, increases in value with a higher current. Concentration polarization, as the C-rate limiting factor, can also explain the difference between an ASSB cell and a liquid cell. In a cell with liquid electrolyte, the electrode particle is surrounded by liquid electrolyte; while in a ASSB prepared by chemical infiltration, only electrode material contact the solid electrolyte on one side of the particle/film.

In order to enable ASSB cells with higher operating C-rate, it is necessary to further reduce the particle size of active electrode material. Thus, the pathway of ion

transport in the less conductive electrode material is shorter, and the concentration polarization can be reduced.

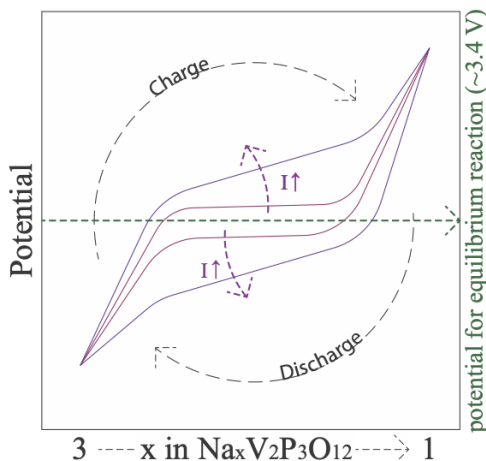


Figure 4.24 The current dependency of charge/discharge curve of a typical NVP-NZSP-Na ASSB cell

Optimization towards higher energy density

In principle, the present electrode has comparable energy density to co-sintered mixed electrodes and is compatible with commercially available batteries after optimization of all components.

As shown in **Figure 4.25**, the theoretical energy densities of model batteries prepared by infiltration method were estimated. The materials used for calculation are: NVP (density approximately 3.1 g cm^{-3}) as positive electrode material, NZSP (3.2 g cm^{-3}) as electrolyte, and metallic Na (1.0 g cm^{-3}) as negative electrode material. Here we assume that the electrolyte has a thickness of $20 \text{ }\mu\text{m}$ and the anode $10 \text{ }\mu\text{m}$. The positive electrode material is assumed to fill 90 % of porosity in the infiltrated cathode, and gives a reversible specific capacity of 95 mAh g^{-1} at the potential of 3.4 V .

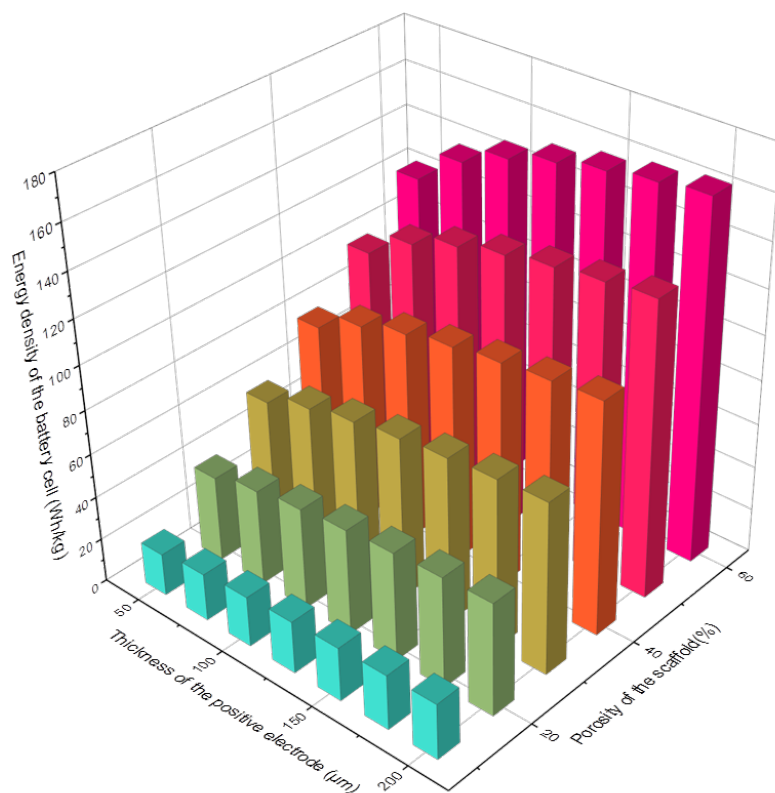


Figure 4.25 Calculated energy densities of battery cells with infiltrated positive electrodes, depending on their thickness and porosity.

Although the cells in this thesis showed excellent performance with a robust material contact, they can be further optimized by tailoring the amount and morphology of the porosity. An optimum between porosity necessary for infiltration and ionic conduction and maximum energy density (related to the amount of active electrode material formed) is yet to be found. The chemical infiltration method has the potential to be scaled up to larger areas to achieve a faster throughput and can be further improved by designing the microstructure of the scaffold, as well as reducing the thickness of the electrolyte layer, using previously developed techniques [59-61].

However, there are some limitations that are difficult to overcome even with fully optimized processes. The most important limitation is the ratio of electrolyte material in the electrode composite, which provides necessary conductivity but reduces the energy density as “dead” mass. As simulated in a Li-S ASSB system [53], the minimum ratio of electrolyte depends on the relative particle size of electrolyte material to that of the active electrode material, and increases with larger electrolyte particles. With active electrode material and electrolyte of the same particle size, weight ratio of active electrode material in the composite can hardly be higher than 50%, while in liquid cells it is normally 90%. As discussed in previous part, small particle size of electrode material is necessary for fast charge/discharge of the ASSBs. In NVP|NZSP|Na cells, NVP should have a much smaller size than that in cells reported in this thesis, i.e. smaller than 1 μm . For solid electrolyte material, it is rather difficult to reduce the particle size to below 1 μm . Thus, the porosity estimation of 60 vol.% is probably the upper limit in the NVP|NZSP|Na system, indicating that the energy density can never be higher than 160 Wh kg^{-1} , the typical density of state-of-the-art liquid batteries. The energy density should be similar with systems using positive electrode materials with similar specific capacities (LiCoO₂, LiFePO₄ etc.) Even for material with ultra-high specific capacities, e.g. LiNi_{0.33}Mn_{0.33}Co_{0.33}O₂ (NMC), the energy density can hardly reach 300 Wh kg^{-1} , the expectation density for next-generation batteries [161].

In a word, though ASSBs have the advantage of using metal negative electrode with high energy density, the limitations in the positive electrode make it difficult to meet the requirement of future commercial applications for mobile devices. Optimizations should be made, not only on developing electrode materials with high specific capacity, but also on developing highly conductive electrode materials. Also, more studies should be made specifically on ASSBs for stationary applications, which is less sensitive to weight, but cost and scalability. From this aspect, Na-ASSBs might be more suitable than Li-ASSBs.

V Summary

In this doctoral thesis, research work mainly focused on two topics: basic properties of NVP, as well as design, preparation, and testing of positive electrodes for Na-ASSBs.

For the investigation of basic properties of the electrode material NVP different raw materials for material synthesis were compared, and the use of NaH_2PO_4 resulted in the highest purity of the produced powder. Systematic experiments were carried out to reveal the source of carbon in NVP samples, and provided a process to remove most of the carbon. Following characterization confirmed the reaction between ethanol and vanadium compounds as the source of carbon and explained the reason why carbon is difficult to remove.

However, densification of NVP samples was difficult via normal sintering methods or crystal growing methods. Thus, special electrochemical cells were designed and prepared, with a thin layer of NVP on top of NZSP, and were used to measure the conductivity of NVP. At 25°C , NVP showed a total conductivity of $1 \times 10^{-6} \text{ S cm}^{-1}$ at 2.9 V, and the conductivity decreased with a higher potential of NVP, to $8 \times 10^{-8} \text{ S cm}^{-1}$ at 3.5 V. This low conductivity, especially at higher voltages, requires a small particle sizes of NVP in electrode composites, in order to reduce the ohmic polarization and concentration polarization.

For Na-ASSBs, a new design was developed for the positive electrode by employing an infiltration method using porous electrolyte scaffolds and a precursor solution. The whole preparation processes were studied to achieve this design, including the preparation of dense-porous double-layered NZSP pellets, the preparation of precursor solution with high vanadium concentration and good wettability on NZSP, the infiltration of the solution into the porous NZSP layer, and the heat-treatment to obtain NVP phase after infiltration.

The bulk-type NVP-NZSP-Na cells showed, for the first time, excellent cycling performance at room temperature. The resulting Na-ASSBs have good specific

capacity of the active positive electrode material ($>95 \text{ mAh g}^{-1}$) and high Coulombic efficiency ($>99 \%$). Various characterization methods revealed that the design and fabrication of positive electrodes optimize the NZSP-NVP interface structures, providing effective ion exchange and minimizing the stress caused by volume change of electrode active materials. As a result of the ideal interface structures, the batteries have low internal resistance and possess stable performance with slow capacity fading ($<10 \%$ after 100 cycles). In addition, the design can be scaled up, with a capacity of 0.60 mAh cm^{-2} at high rate of 0.5 mA cm^{-2} achieved.

The achieved results are an important step towards the practical application of Na-ASSBs, demonstrating an excellent strategy for designing ideal solid-solid interfaces and providing a breakthrough for the fabrication of ceramic-based ASSBs. Based on this cell structure, an outlook was made on the future of ASSBs, showing that ASSBs has the possibilities to reach the energy densities of state-of-the-art batteries with liquid electrolyte. The power density will be a main problem in the developing of ASSBs and requires further optimization on the positive electrode structure. It is also difficult to achieve the overall surpassing of ASSBs to batteries with liquid electrolyte, unlike the expectation of many researchers in the community. ASSBs may have a limited application in specific areas in the future. However, ASSBs, especially Na-ASSBs will be promising candidate for stationary applications with all the advantages regarding to safety and temperature suitability.

References

1. Manthiram, A., X. Yu, and S. Wang, *Nat. Rev. Mater.* 2017, 2, p. 1.
2. *Linden's Handbook of Batteries*. Fourth Edition ed. 2011, New York: McGraw-hill.
3. Tarascon, J.-M. and M. Armand, *Issues and challenges facing rechargeable lithium batteries*, in *Materials For Sustainable Energy: A Collection of Peer-Reviewed Research and Review Articles from Nature Publishing Group*. 2011, World Scientific. p. 171.
4. Bard, A.J., L.R. Faulkner, J. Leddy, and C.G. Zoski, *Electrochemical methods: fundamentals and applications*. Vol. 2. 1980: Wiley New York.
5. Younesi, R., G.M. Veith, P. Johansson, K. Edström, and T. Vegge, *Energy & Environmental Science* 2015, 8, p. 1905.
6. Faraday, M., *Philosophical Transactions of the Royal Society of London* 1833, p. 23.
7. Yao, Y.-F.Y. and J. Kummer, *J. Inorg. Nucl. Chem.* 1967, 29, p. 2453.
8. Goodenough, J.B., H.-P. Hong, and J. Kafalas, *Mater. Res. Bull.* 1976, 11, p. 203.
9. Chandra, S., H. Lal, and K. Shahi, *J. Phys. D Appl. Phys.* 1974, 7, p. 194.
10. Reuter, B. and K. Hardel, *Angew. Chem.* 1960, 72, p. 138.
11. Fenton, D., *Polymer* 1973, 14, p. 589.
12. Knödler, R., *J. Appl. Electrochem.* 1984, 14, p. 39.
13. Oshima, T., M. Kajita, and A. Okuno, *International J. Applied Ceramic Technology* 2004, 1, p. 269.
14. Bones, R., J. Coetzer, R. Galloway, and D. Teagle, *J. Electrochem. Soc.* 1987, 134, p. 2379.
15. Coetzer, J., *J. Power sources* 1986, 18, p. 377.
16. Capasso, C. and O. Veneri, *Energy Procedia* 2014, 61, p. 1138.
17. Robinson, A.L. and J. Janek, *MRS Bull.* 2014, 39, p. 1046.
18. Hanyu, Y. and I. Honma, *Scientific reports* 2012, 2, p. 453.
19. Aono, H., E. Sugimoto, Y. Sadaoka, N. Imanaka, and G.-y. Adachi, *Solid State Ion.* 1990, 40, p. 38.
20. Thangadurai, V., H. Kaack, and W.J. Weppner, *J. Am. Ceram. Soc.* 2003, 86, p. 437.
21. Janek, J. and W.G. Zeier, *Nat. Energy* 2016, 500, p. 300.
22. Wan, H., J.P. Mwizerwa, X. Qi, X. Xu, H. Li, Q. Zhang, L. Cai, Y.S. Hu, and X. Yao, *ACS Appl. Mater. Interfaces* 2018, 10, p. 12300.
23. Kato, T., S. Iwasaki, Y. Ishii, M. Motoyama, W.C. West, Y. Yamamoto, and Y. Iriyama, *J. Power Sources* 2016, 303, p. 65.
24. Duchêne, L., R.S. Kühnel, E. Stimp, E. Cuervo Reyes, A. Remhof, H. Hagemann, and C. Battaglia, *Energy Environ. Sci.* 2017, 10, p. 2609.
25. Chen-Yang, Y., H. Chen, F. Lin, and C. Chen, *Solid State Ion.* 2002, 150, p. 327.
26. Choi, S.W., S.M. Jo, W.S. Lee, and Y.R. Kim, *Adv. Mater.* 2003, 15, p. 2027.
27. Borghini, M.C., M. Mastragostino, S. Passerini, and B. Scrosati, *J. Electrochem. Soc.* 1995, 142, p. 2118.
28. Liu, Y., J. Lee, and L. Hong, *J. Power Sources* 2004, 129, p. 303.
29. Song, J., Y. Wang, and C.C. Wan, *J. Power Sources* 1999, 77, p. 183.
30. Zhao, C., L. Liu, X. Qi, Y. Lu, F. Wu, J. Zhao, Y. Yu, Y.S. Hu, and L. Chen, *Adv. Energy Mater.* 2018, p. 1703012.
31. Albertus, P., S. Babinec, S. Litzelman, and A. Newman, *Nature Energy* 2018, 3, p. 16.
32. Zhao, Y., K.R. Adair, and X. Sun, *Energy & Environmental Science* 2018, 11, p. 2673.
33. Krauskopf, T., H. Hartmann, W.G. Zeier, and J.r. Janek, *ACS Appl. Mater. Interfaces* 2019, 11, p. 14463.
34. Tsai, C.-L., Q. Ma, C. Dellen, S. Lobe, F. Vondahlen, A. Windmüller, D. Grüner, H. Zheng, S. Uhlenbruck, and M. Finsterbusch, *Sustainable Energy & Fuels* 2019.

35. Krauskopf, T., B. Mogwitz, C. Rosenbach, W.G. Zeier, and J. Janek, *Advanced Energy Materials* 2019, 9, p. 1902568.
36. Tsai, C.-L., T. Lan, C. Dellen, Y. Ling, Q. Ma, D. Fattakhova-Rohlfing, O. Guillon, and F. Tietz, *J. Power Sources* 2020, 476, p. 228666.
37. Liu, L., X. Qi, Q. Ma, X. Rong, Y.-S. Hu, Z. Zhou, H. Li, X. Huang, and L. Chen, *ACS Appl. Mater. Interfaces* 2016, 8, p. 32631.
38. Lu, Y., J.A. Alonso, Q. Yi, L. Lu, Z.L. Wang, and C. Sun, *Adv. Energy Mater.* 2019, p. 1901205.
39. Wu, T., Z. Wen, C. Sun, X. Wu, S. Zhang, and J. Yang, *J. Mater. Chem. A* 2018, 6, p. 12623.
40. Yang, J., H.-L. Wan, Z.-H. Zhang, G.-Z. Liu, X.-X. Xu, Y.-S. Hu, and X.-Y. Yao, *Rare Metals* 2018, 37, p. 480.
41. Zhang, Z., Q. Zhang, J. Shi, Y.S. Chu, X. Yu, K. Xu, M. Ge, H. Yan, W. Li, L. Gu, Y.-S. Hu, H. Li, X.-Q. Yang, L. Chen, and X. Huang, *Adv. Energy Mater.* 2017, 7, p. 1601196.
42. Zhao, K., Y. Liu, S. Zhang, S. He, N. Zhang, J. Yang, and Z. Zhan, *Electrochem. Commun.* 2016, 69, p. 59.
43. Hitz, G.T., D.W. McOwen, L. Zhang, Z. Ma, Z. Fu, Y. Wen, Y. Gong, J. Dai, T.R. Hamann, L. Hu, and E.D. Wachsman, *Mater. Today* 2019, 22, p. 50.
44. Gao, H., S. Xin, L. Xue, and J.B. Goodenough, *Chem* 2018, 4, p. 833.
45. Zhou, W., Y. Li, S. Xin, and J.B. Goodenough, *ACS Cent. Sci.* 2017, 3, p. 52.
46. Ma, Q., C. Tsai, X.K. Wei, M. Heggen, F. Tietz, and J.T.S. Irvine, *J. Mater. Chem. A* 2019, 7, p. 7766.
47. Ren, Y., T. Liu, Y. Shen, Y. Lin, and C.-W. Nan, *Journal of Materiomics* 2016, 2, p. 256.
48. Lalère, F., J.B. Leriche, M. Courty, S. Boulineau, V. Viallet, C. Masquelier, and V. Seznec, *J. Power Sources* 2014, 247, p. 975.
49. Han, F., J. Yue, C. Chen, N. Zhao, X. Fan, Z. Ma, T. Gao, F. Wang, X. Guo, and C. Wang, *Joule* 2018, 2, p. 497.
50. Yamauchi, H., J. Ikejiri, F. Sato, H. Oshita, T. Honma, and T. Komatsu, *Journal of the American Ceramic Society* 2020.
51. Kehne, P., C. Guhl, Q. Ma, F. Tietz, L. Alff, R. Hausbrand, and P. Komissinskiy, *J. Power Sources* 2019, 409, p. 86.
52. Kehne, P., C. Guhl, Q. Ma, F. Tietz, L. Alff, R. Hausbrand, and P. Komissinskiy, *J. Electrochem. Soc.* 2019, 166, p. A5328.
53. Shi, T., Q. Tu, Y. Tian, Y. Xiao, L.J. Miara, O. Kononova, and G. Ceder, *Advanced Energy Materials* 2019.
54. Li, J., C. Ma, M. Chi, C. Liang, and N.J. Dudney, *Adv. Energy Mater.* 2015, 5, p. 1401408.
55. Ma, Q., B. Iwanschitz, E. Dashjav, S. Baumann, D. Sebold, I.A. Raj, A. Mai, and F. Tietz, *J. Power Sources* 2015, 279, p. 678.
56. Ma, Q., F. Tietz, A. Leonide, and E. Ivers-Tiffée, *Electrochem. Commun.* 2010, 12, p. 1326.
57. Vohs, J.M. and R.J. Gorte, *Adv. Mater.* 2009, 21, p. 943.
58. Kotobuki, M., H. Munakata, and K. Kanamura, *J. Power Sources* 2011, 196, p. 6947.
59. Kotobuki, M., Y. Suzuki, K. Kanamura, Y. Sato, K. Yamamoto, and T. Yoshida, *J. Power Sources* 2011, 196, p. 9815.
60. Fu, K.K., Y. Gong, G.T. Hitz, D.W. McOwen, Y. Li, S. Xu, Y. Wen, L. Zhang, C. Wang, and G. Pastel, *Energy Environ. Sci.* 2017, 10, p. 1568.
61. Gong, Y., K. Fu, S. Xu, J. Dai, T.R. Hamann, L. Zhang, G.T. Hitz, Z. Fu, Z. Ma, D.W. McOwen, X. Han, L. Hu, and E.D. Wachsman, *Mater. Today* 2018, 21, p. 594.
62. Hamann, T.R., L. Zhang, Y. Gong, G.L. Godbey, J.E. Gritton, Z. Ma, D.W. McOwen, G.T. Hitz, L. Hu, and E.D. Wachsman, *Microscopy and Microanalysis* 2018, 24, p. 814.
63. Ren, Y., T. Liu, Y. Shen, Y. Lin, and C.-W. Nan, *Ionics* 2017, 23, p. 2521.
64. McOwen, D.W., S. Xu, Y. Gong, Y. Wen, G.L. Godbey, J.E. Gritton, T.R. Hamann, J. Dai, G.T. Hitz, L. Hu, and E.D. Wachsman, *Adv. Mater.* 2018, 30, p. e1707132.
65. Ren, Y., T. Liu, Y. Shen, Y. Lin, and C.-W. Nan, *Ion.* 2017, 23, p. 2521.
66. Dunn, B., H. Kamath, and J.-M. Tarascon, *Science* 2011, 334, p. 928.

67. Yang, Z., J. Zhang, M.C. Kintner-Meyer, X. Lu, D. Choi, J.P. Lemmon, and J. Liu, *Chem. Rev.* 2011, 111, p. 3577.
68. Larcher, D. and J.-M. Tarascon, *Nat. Chem.* 2015, 7, p. 19.
69. Wadia, C., P. Albertus, and V. Srinivasan, *Journal of Power Sources* 2011, 196, p. 1593.
70. Pan, H., Y.-S. Hu, and L. Chen, *Energy Environ. Sci.* 2013, 6, p. 2338.
71. Yabuuchi, N., K. Kubota, M. Dahbi, and S. Komaba, *Chem. Rev.* 2014, 114, p. 11636.
72. Slater, M.D., D. Kim, E. Lee, and C.S. Johnson, *Adv. Funct. Mater.* 2013, 23, p. 947.
73. Kasperkiewicz, J., J. Kovacich, and D. Lichtman, *J. Electron Spectrosc. Relat. Phenom.* 1983, 32, p. 123.
74. Dean, J.A., *Lange's handbook of chemistry*. 1999: New York; London: McGraw-Hill, Inc.
75. Samsonov, G., *Mechanical properties of the elements*, in *Handbook of the Physicochemical Properties of the Elements*. 1968, Springer. p. 387.
76. Noguchi, Y., E. Kobayashi, L.S. Plashnitsa, S. Okada, and J.-i. Yamaki, *Electrochim. Acta* 2013, 101, p. 59.
77. Jian, Z.L., W.Z. Han, X. Lu, H.X. Yang, Y.S. Hu, J. Zhou, Z.B. Zhou, J.Q. Li, W. Chen, D.F. Chen, and L.Q. Chen, *Adv. Energy Mater.* 2013, 3, p. 156.
78. Zhu, C., P. Kopold, P.A. van Aken, J. Maier, and Y. Yu, *Adv. Mater.* 2016, 28, p. 2409.
79. Delmas, C., R. Olazcuaga, F. Cherkaoui, R. Brochu, and G. Le Flem, *Comptes rendus hebdomadaires des séances de l'Académie des sciences. Série C, Sciences chimiques* 1978, 287, p. 169.
80. Goodenough, J.B., H.Y.P. Hong, and J.A. Kafalas, *Mater. Res. Bull.* 1976, 11, p. 203.
81. Gopalakrishnan, J. and K.K. Rangan, *Chem. Mater.* 1992, 4, p. 745.
82. Korhuis, V., R. Hoffmann, J. Huang, and A. Sleight, *Chem. Mater.* 1993, 5, p. 206.
83. Zatovsky, I.V., *Acta Crystallogr. E* 2010, 66, p. i12.
84. Cushing, B.L. and J.B. Goodenough, *J. Solid State Chem.* 2001, 162, p. 176.
85. Jian, Z., L. Zhao, H. Pan, Y.-S. Hu, H. Li, W. Chen, and L. Chen, *Electrochem. Commun.* 2012, 14, p. 86.
86. Kang, J., S. Baek, V. Mathew, J. Gim, J. Song, H. Park, E. Chae, A.K. Rai, and J. Kim, *J. Mater. Chem.* 2012, 22, p. 20857.
87. Guillon, O., C. Lenser, D. Udomsilp, N. Menzler, P. Holtappels, T. Fujisaki, L. Kwati, H. Matsumoto, A. Sabato, and F. Smeacetto, *Advanced Ceramics for Energy Conversion and Storage*. 2020: Elsevier.
88. Lim, S.Y., H. Kim, R. Shakoer, Y. Jung, and J.W. Choi, *J. Electrochem. Soc.* 2012, 159, p. A1393.
89. Jian, Z., C. Yuan, W. Han, X. Lu, L. Gu, X. Xi, Y.-S. Hu, H. Li, W. Chen, D. Chen, Y. Ikuhara, and L. Chen, *Adv. Funct. Mater.* 2014, 24, p. 4265.
90. Chotard, J.-N., G. Rousse, R. David, O. Mentre, M. Courty, and C. Masquelier, *Chem. Mater.* 2015, 27, p. 5982.
91. Jung, Y.H., C.H. Lim, and D.K. Kim, *J. Mater. Chem. A* 2013, 1, p. 11350.
92. Schwartz, M.E. and J.D. Switalski, *The Journal of Chemical Physics* 1972, 57, p. 4132.
93. Lim, S.-J., D.-W. Han, D.-H. Nam, K.-S. Hong, J.-Y. Eom, W.-H. Ryu, and H.-S. Kwon, *J. Mater. Chem. A* 2014, 2, p. 19623.
94. Aragon, M.J., P. Lavela, R. Alcantara, and J.L. Tirado, *Electrochim. Acta* 2015, 180, p. 824.
95. Aragon, M.J., P. Lavela, G.F. Ortiz, and J.L. Tirado, *ChemElectroChem* 2015, 2, p. 995.
96. Lalère, F., V. Seznec, M. Courty, R. David, J.N. Chotard, and C. Masquelier, *J. Mater. Chem. A* 2015, 3, p. 16198.
97. Li, H., X. Yu, Y. Bai, F. Wu, C. Wu, L.-Y. Liu, and X.-Q. Yang, *J. Mater. Chem. A* 2015, 3, p. 9578.
98. Zhang, H., I. Hasa, B. Qin, T. Diemant, D. Buchholz, R.J. Behm, and S. Passerini, *ChemElectroChem* 2017, 4, p. 1256.
99. Klee, R., M. Wiatrowski, M.J. Aragon, P. Lavela, G.F. Ortiz, R. Alcantara, and J.L. Tirado, *ACS Appl. Mater. Interfaces* 2017, 9, p. 1471.
100. Chekannikov, A., R. Kapaev, S. Novikova, N. Tabachkova, T. Kulova, A. Skundin, and A. Yaroslavtsev, *J. Solid State Electrochem.* 2017, 21, p. 1.

101. Zhang, J., Y. Fang, L. Xiao, J. Qian, Y. Cao, X. Ai, and H. Yang, *ACS Appl. Mater. Interfaces* 2017, 9, p. 7177.
102. Song, W., X. Ji, C. Pan, Y. Zhu, Q. Chen, and C.E. Banks, *Phys Chem Chem Phys* 2013, 15, p. 14357.
103. Nefedov, V., D. Gati, B. Dzhurinskii, N. Sergushin, and Y.V. Salyn, *Zhurnal Neorganicheskoi Khimii* 1975, 20, p. 2307.
104. Horvath, B., J. Strutz, J. Geyer - Lippmann, and E. Horvath, *Zeitschrift für anorganische und allgemeine Chemie* 1981, 483, p. 205.
105. Slink, W.E. and P.B. DeGroot, *J. Catalysis* 1981, 68, p. 423.
106. Werfel, F. and O. Brümmer, *Phys. Scr.* 1983, 28, p. 92.
107. Nag, N. and F. Massoth, *J. Catalysis* 1990, 124, p. 127.
108. Gopalakrishnan, R., B. Chowdari, and K. Tan, *Solid State Ion.* 1992, 53, p. 1168.
109. Cornaglia, L. and E. Lombardo, *J. Phys. Condens. Matter* 1993, 5, p. A225.
110. Silversmit, G., D. Depla, H. Poelman, G.B. Marin, and R. De Gryse, *J. Electron Spectrosc. Relat. Phenom.* 2004, 135, p. 167.
111. Saravanan, K., C.W. Mason, A. Rudola, K.H. Wong, and P. Balaya, *Adv. Energy Mater.* 2013, 3, p. 444.
112. Pivko, M., I. Arcon, M. Bele, R. Dominko, and M. Gaberscek, *J. Power Sources* 2012, 216, p. 145.
113. Tao, S., X. Wang, P. Cui, Y. Wang, Y.A. Haleem, S. Wei, W. Huang, L. Song, and W. Chu, *RSC Adv.* 2016, 6, p. 43591.
114. Song, W., X. Ji, Y. Yao, H. Zhu, Q. Chen, Q. Sun, and C.E. Banks, *Phys. Chem. Chem. Phys.* 2014, 16, p. 3055.
115. Zhu, C., K. Song, P.A. van Aken, J. Maier, and Y. Yu, *Nano Lett.* 2014, 14, p. 2175.
116. Li, S., Y. Dong, L. Xu, X. Xu, L. He, and L. Mai, *Adv. Mater.* 2014, 26, p. 3545.
117. Wang, W.-J., H.-B. Zhao, A.-B. Yuan, J.-H. Fang, and J.-Q. Xu, *Acta Physico-Chimica Sinica* 2014, 30, p. 1113.
118. Yan, J., X. Liu, and B. Li, *Electrochem. Commun.* 2015, 56, p. 46.
119. Fang, Y., L. Xiao, X. Ai, Y. Cao, and H. Yang, *Adv. Mater.* 2015, 27, p. 5895.
120. Liu, J., K. Tang, K. Song, P.A. van Aken, Y. Yu, and J. Maier, *Nanoscale* 2014, 6, p. 5081.
121. Rui, X., W. Sun, C. Wu, Y. Yu, and Q. Yan, *Adv. Mater.* 2015, 27, p. 6670.
122. Zhang, W., Y. Liu, C. Chen, Z. Li, Y. Huang, and X. Hu, *Small* 2015, 11, p. 3822.
123. Padhi, A.K., K. Nanjundaswamy, and J.B. Goodenough, *J. Electrochem. Soc.* 1997, 144, p. 1188.
124. Plashnitsa, L.S., E. Kobayashi, Y. Noguchi, S. Okada, and J.-i. Yamaki, *J. Electrochem. Soc.* 2010, 157, p. A536.
125. Shen, W., C. Wang, H. Liu, and W. Yang, *Chem.: Eur. J* 2013, 19, p. 14712.
126. Chu, Z. and C. Yue, *Solid State Ion.* 2016, 287, p. 36.
127. Chu, Z. and C. Yue, *Ceram. Int.* 2016, 42, p. 820.
128. Fang, J., S. Wang, Z. Li, H. Chen, L. Xia, L. Ding, and H. Wang, *J. Mater. Chem. A* 2016, 4, p. 1180.
129. Hu, Q., J.-Y. Liao, B.-K. Zou, H.-Y. Wang, and C.-H. Chen, *J. Mater. Chem. A* 2016, 4, p. 16801.
130. Klee, R., P. Lavela, M.J. Aragon, R. Alcantara, and J.L. Tirado, *J. Power Sources* 2016, 313, p. 73.
131. Rajagopalan, R., L. Zhang, S.X. Dou, and H.K. Liu, *Adv. Mater. Interfaces* 2016, 3.
132. Shen, W., H. Li, Z. Guo, C. Wang, Z. Li, Q. Xu, H. Liu, Y. Wang, and Y. Xia, *ACS Appl. Mater. Interfaces* 2016, 8, p. 15341.
133. Song, J., S. Park, V. Mathew, J. Gim, S. Kim, J. Jo, S. Kim, M.H. Alfaruqi, J.P. Baboo, I.H. Kim, S.J. Song, and J. Kim, *ACS Appl. Mater. Interfaces* 2016, 8, p. 35235.
134. Tao, S., P. Cui, W. Huang, Z. Yu, X. Wang, S. Wei, D. Liu, L. Song, and W. Chu, *Carbon* 2016, 96, p. 1028.
135. Xu, Y., Q. Wei, C. Xu, Q. Li, Q. An, P. Zhang, J. Sheng, L. Zhou, and L. Mai, *Adv. Energy Mater.* 2016, 6.
136. Zhong, X., Z. Yang, Y. Jiang, W. Li, L. Gu, and Y. Yu, *ACS Appl. Mater. Interfaces* 2016, 8, p. 32360.
137. Delmas, C., A. Nadiri, and J.L. Soubeyroux, *Solid State Ion.* 1988, 28, p. 419.

138. Kajiyama, S., J. Kikkawa, J. Hoshino, M. Okubo, and E. Hosono, *Chem.: Eur. J* 2014, 20, p. 12636.
139. Huang, H., S.C. Yin, T. Kerr, N. Taylor, and L.F. Nazar, *Adv. Mater.* 2002, 14, p. 1525.
140. Lalere, F., J.B. Leriche, M. Courty, S. Boulineau, V. Viallet, C. Masquelier, and V. Seznec, *J. Power Sources* 2014, 247, p. 975.
141. Pechini, M.P., 1967, US Patent 3,330,697
142. Naqash, S., Q. Ma, F. Tietz, and O. Guillon, *Solid State Ion.* 2017, 302, p. 83.
143. Bragg, W.H. and W.L. Bragg, *Proceedings of the Royal Society of London. Series A, Containing Papers of a Mathematical and Physical Character* 1913, 88, p. 428.
144. Ewald, P.P., *Annalen der Physik* 1921, 369, p. 253.
145. Rodríguez-Carvajal, J., *Physica B* 1993, 192, p. 55.
146. Momma, K. and F. Izumi, *J. Appl. Crystallogr.* 2011, 44, p. 1272.
147. Gopalakrishnan, R., B. Chowdari, and K. Tan, *Solid State Ionics* 1992, 53, p. 1168.
148. Jesson, D. and S.J. Pennycook, *Proceedings of the Royal Society of London. Series A: Mathematical and Physical Sciences* 1995, 449, p. 273.
149. Kee, Y., N. Dimov, A. Staikov, P. Barpanda, Y.-C. Lu, K. Minami, and S. Okada, *RSC Adv.* 2015, 5, p. 64991.
150. Lan, T., Q. Ma, C.-L. Tsai, F. Tietz, and O. Guillon, *Batteries & Supercaps* 2020, 3, p. 1.
151. Wang, H., G. Hasegawa, Y. Akiyama, T. Yamamoto, A. Inoishi, H. Akamatsu, M. Inada, T. Ishihara, and K. Hayashi, *Electrochimica Acta* 2019, 305, p. 197.
152. Guin, M., F. Tietz, and O. Guillon, *Solid State Ionics* 2016, 293, p. 18.
153. Lan, T., C.-L. Tsai, F. Tietz, X.-K. Wei, M. Heggen, R.E. Dunin-Borkowski, R. Wang, Y. Xiao, Q. Ma, and O. Guillon, *Nano Energy* 2019, 65, p. 104040.
154. Ma, Q., M. Balaguer, D. Pérez-Coll, L.G. de Haart, J.M. Serra, G.C. Mather, F. Tietz, N. Menzler, and O. Guillon, *ACS Appl. Energy Mater.* 2018, 1, p. 2784.
155. Chen, S., C. Wu, L. Shen, C. Zhu, Y. Huang, K. Xi, J. Maier, and Y. Yu, *Adv. Mater.* 2017.
156. Schafbauer, W., F. Schulze-Küppers, S. Baumann, W.A. Meulenber, N.H. Menzler, H.P. Buchkremer, and D. Stöver. *Tape casting as a multi purpose shaping technology for different applications in energy issues.* in *Materials Science Forum*. 2012. Trans Tech Publ.
157. Plashnitsa, L.S., E. Kobayashi, Y. Noguchi, S. Okada, and J.-i. Yamaki, *J. Electrochem. Soc.* 2010, 157, p. A536.
158. Nellist, P. and S. Pennycook, *The principles and interpretation of annular dark-field Z-contrast imaging*, in *Adv. Imag. Elect. Phys.* 2000, Elsevier. p. 147.
159. Inoishi, A., T. Omuta, E. Kobayashi, A. Kitajou, and S. Okada, *Adv. Mater. Interfaces* 2017, 4.
160. Malik, R., A. Abdellahi, and G. Ceder, *J. Electrochem. Soc.* 2013, 160, p. A3179.
161. Niu, C., H. Lee, S. Chen, Q. Li, J. Du, W. Xu, J.-G. Zhang, M.S. Whittingham, J. Xiao, and J. Liu, *Nature Energy* 2019, p. 1.

Acknowledgements

This work became possible with the help of many people, and I would like to express my gratitude to all of them here in this part.

First of all, I would like to thank Dr. Qianli Ma, who gave me direct guidance about my experimental and theoretical work. In the last three years, almost every day, I worked together with him, learnt from him, and was inspired by his enthusiasm for research. Also, I want to thank him for his caring about my personal life here, starting from my arrival at Düren Bahnhof (and failure to catch the Rurtalbahn train due to the daily delay of the Deutsche Bahn).

Also, I would like to thank Dr. Frank Tietz, the leader of our team. I feel very lucky to finish (not jet when writing) my doctoral thesis in his team, with his wide knowledge about material science, his deep understanding to the research field, his openness to all my naïve ideas, as well as his patience during all the discussions and when correcting my flawed manuscripts (including this one). Besides, I am grateful for his kind, helpful, and solid support for my work.

Another very important person to this work is my supervisor, Prof. Dr. Olivier Guillon. I want to thank him for his strategic guidance on my working, which outlined my direction in all my miscellaneous works around this topic. Also, I learnt a lot from his solid instructions on material development, benefit a lot from his guidance on many aspects from designing experiments to writing paperwork, and get inspired a lot from his scientific attitude.

This thesis also contains precious contributions from Dr. Chih-Long Tsai, who helped design many of the experiments and guided me on idea development, on experimental techniques, on paperwork, as well as on dealing with “reviewer 3”. Important contributions of this thesis also come from Dr. Xian-Kui Wei, Dr. Marc Heggen, and Prof. Dr. Rafal E. Dunin-Borkowski from ERC, as well as Rui Wang and Prof. Dr. Yinguo Xiao from Peking University Shenzhen Graduate School. Financial support from China Scholarship Council (CSC) (file no. 201606210131) is gratefully acknowledged.

I am also very grateful to Dr. Sandra Lobe and Dr. Christian Dellen for both many scientific discussions and the maintenance of some key instruments. Colleagues from my group, Dr. Monika Bhardwaj, Dr. Enkhtsetseg Dashjav, and Dr. Sahir Naqash, also inspired me many times during my work on the thesis. Experimental supports to the thesis also come

from: Volker Bader (heat-treatments), Marie-Theres Gerhards and Sylke Pristat (thermogravimetric measurements), Dr. Yoo-Jung Sohn (XRD), Dr. Daniel Grüner and Dr. Doris Sebold (SEM), Dr. Robert Mücke (simulation), Dr. Falk Schulze-Küppers (instructions on porosity making and of course the coffee machine), Dr. Volker Nischwitz (ICP-OES), Dr. Sabine Willbold (NMR), Florian Thaler (contact angle measurements), Frank Vondahlen (instrument maintenance), Erhan Sucuoglu and Tobias Offermanns (machining of samples). Also a lot of other colleagues help me with this work, of whom I cannot list everyone with details. Many thanks to all of you. During the last three years, I benefited a lot from working together with colleagues from the battery department: Prof. Dr. Dina Fattakhova, Dr. Sven Uhlenbruck, Dr. Martin Finsterbusch, Ah-Ram Seok, Dr. Alexandra von der Heiden, Dr. Anna Windmüller, Asmaa Loutati, Dr. Bambar Davaasuren, Gerald Dück, Jochen Rippbahn, Martin Ihrig, Michaela Andreas, Dr. Ranjith Vellacheri, Ruijie Ye, Serkan Sevinc, Prof. Yihan Ling, and Dr. Yulia Arinicheva. I wish I could list more without the suspicion of making up the thesis length.

Although not directly related to this work, many colleagues from IEK-1 filled my last three years at IEK-1 with wise discussions and happy chats. Chen Cao and Jun Zhang will also defend their thesis in the near future, and I hope they can enjoy it, too. Dr. Dapeng Zhou and Dr. Yang Liu have started their academic careers, and I wish them a bright future. I enjoyed sharing offices with Apurv Dash, Moritz Kindelmann, Ralf Steinert, as well as some already mentioned colleagues, and thank them for enduring my preference of darkness. There should be a limitation to listing and I have to stop here.

Special thanks are given to Junyan Song, who is always by my side (chemically). Also, special thanks are given to my parents, Dr. Jingli Lan and Prof. Wenli Pang, for their care and support all the way.

Thanks are given to some dead buddies: Johann S. Bach (I guess I won't listen to his keyboard works for a while after finishing this thesis), Georg F. Händel, Prof. Dimitri D. Shostakovich, Franz P. Schubert, J. Anton Bruckner, Ludwig v. Beethoven, W. Richard Wagner, Gustav Mahler, and Wolfgang Mozart. All of them made my experimental work and especially writing of this thesis much easier. I hope they didn't scare the colleagues who shared a same lab with me. And finally, here is a small piece of music for woodwind quartet, dedicated to the two trees (look like birches) in the north of IEK-1.

93 Prestissimo

Musical score for measures 93-102. The score is in 3/4 time and features a complex texture with multiple voices. Dynamics include *f*, *ff*, *mf*, and *mp*. The tempo is marked **Prestissimo**.

97

Musical score for measures 97-106. The score continues with intricate melodic and harmonic lines. Dynamics include *mp*. The tempo remains **Prestissimo**.

106

Musical score for measures 106-121. The texture remains dense with multiple voices. Dynamics include *f*, *ff*, and *mp*. The tempo remains **Prestissimo**.

122 D) Largo

Musical score for measures 122-131. The tempo changes to **Largo**. The score features a dramatic shift in dynamics, including *f*, *ff*, *p*, and *mp*. The time signature changes to 6/8.

136 E) Presto

Musical score for measures 136-143. The tempo changes to **Presto**. The score features a return to a more active texture with dynamics including *f* and *mp*. The time signature changes to 4/4.

143

Musical score for measures 143-148. The score concludes with a final section featuring dynamics of *mp* and *mf*.

Band / Volume 538

Transparent Passivating Contact for Crystalline Silicon Solar Cells

M. Köhler (2021), 186 pp

ISBN: 978-3-95806-550-5

Band / Volume 539

Distribution of trace gases with adverse effects on fuel cells

D. Klemp, R. Wegener, R. Dubus, L. Karadurmus, N. Kille, Z. Tan (2021),
160 pp

ISBN: 978-3-95806-551-2

Band / Volume 540

Cyclotron Irradiation on Tungsten & Co-relation of Thermo-Mechanical Properties to Displacement and Transmutation Damage

R. Rayaprolu (2021), xiv, 211 pp

ISBN: 978-3-95806-552-9

Band / Volume 541

Smart Energy in Haushalten:

Technologien, Geschäftsmodelle, Akzeptanz und Wirtschaftlichkeit

H. Shamon, T. Rehm, B. Helgeson, F. Große-Kreul, M. Gleue, U. Paukstadt,
G. Aniello, T. Schneiders, C. Frings, A. Reichmann, A. Löschel, T. Gollhardt,
W. Kuckshinrichs, K. Gruber, P. Overath, C. Baedeker, F. Chasin, K. Witte,
J. Becker

(2021), VI, 142 pp

ISBN: 978-3-95806-554-3

Band / Volume 542

Deployment Status of Fuel Cells in Road Transport: 2021 Update

R. C. Samsun, L. Antoni, M. Rex, D. Stolten (2021), 37 pp

ISBN: 978-3-95806-556-7

Band / Volume 543

Processing and creep resistance of short SiC fiber containing Ti_3SiC_2 MAX phase composites

A. Dash (2021), vii, 125 pp

ISBN: 978-3-95806-558-1

Band / Volume 544

Synthese und Charakterisierung von Geopolymeren für die Entsorgung der Spaltprodukte ^{137}Cs und ^{90}Sr

S. K. Weigelt (2021), VI, 186 pp

ISBN: 978-3-95806-559-8

Band / Volume 545

Potential depletion of ozone in the mid-latitude lowermost stratosphere in summer under geoengineering conditions

S. Robrecht (2021), 185 pp

ISBN: 978-3-95806-563-5

Band / Volume 546

Two-phase Flow in Porous Transport Layers of Polymer Electrolyte Membrane Electrolysers

D. Borah (2021), xi, 196 pp

ISBN: 978-3-95806-564-2

Band / Volume 547

Effects of root temperature on food quality of horticultural crops

F. He (2021), V, 143 pp

ISBN: 978-3-95806-565-9

Band / Volume 548

Verhalten und Kontrolle von Schlacken des bioliq®-Vergasers

K. Mielke (2021), 162, XXXV pp

ISBN: 978-3-95806-566-6

Band / Volume 549

Gravity waves resolved in Numerical Weather Prediction products

C. Strube (2021), iii, 139 pp

ISBN: 978-3-95806-567-3

Band / Volume 550

Experimental study of the chemical degradation of biogenic volatile organic compounds by atmospheric OH radicals

M. Rolletter (2021), XIII, 199 pp

ISBN: 978-3-95806-568-0

Band / Volume 551

Infiltrated Positive Electrodes for All-Solid-State Sodium Batteries

T. Lan (2021), vi, 104 pp

ISBN: 978-3-95806-576-5

Weitere **Schriften des Verlags im Forschungszentrum Jülich** unter
<http://www.zb1.fz-juelich.de/verlagextern1/index.asp>

Energie & Umwelt / Energy & Environment
Band / Volume 551
ISBN 978-3-95806-576-5